Supporting Information for the Publication Entitled:

Unprecedented pairs of uranium (IV/V) hydroxido and (IV/V/VI) oxido complexes supported by a seven-coordinate cyclen-anchored tris-aryloxide ligand

Sascha T. Löffler, Julian Hümmer, Andreas Scheurer, Frank W. Heinemann and Karsten Meyer*

Friedrich-Alexander-Universität Erlangen-Nürnberg (FAU), Department of Chemistry and Pharmacy, Inorganic Chemistry, Egerlandstraße 1, 91058 Erlangen, Germany.

Supporting Information Table of Contents

General Considerations

All air- and moisture-sensitive experiments were performed under dry nitrogen atmosphere, using standard Schlenk techniques or an MBraun inert-gas glovebox, containing an atmosphere of purified dinitrogen. The glovebox was equipped with a –35 °C freezer. Solvents were purified using a two-column solid-state purification system (JC Meyer Solvent System, Irvine, CA, www.jcmeyer-solventsystems.com), transferred to the glovebox without exposure to air and moisture, and stored over activated molecular sieves and potassium, where appropriate (*n*-pentane, *n*-hexane, benzene). Commercially available starting materials were purchased from prominent suppliers (Acros Organics, Alfa Aesar, Sigma Aldrich, Merck, TCI, VWR) and were used without further purification. The precursor complex $[U^{III}(N(SiMe_3)_2)_3]$ was prepared as described in literature.[1] The cyclen anchor 1-methyl-1,4,7,10-tetraazacyclododecane of the ligand was synthesized as described in literature.[2]

NMR spectra were recorded on JEOL JNM ECX and ECZS 400 MHz instruments, operating at respective frequencies of 400.18 MHz and 399.79 (^{1}H NMR), and 100.62 and 100.53 MHz (^{13}C NMR), with a probe temperature of 23 °C. Chemical shifts, δ, are reported relative to the ^{1}H resonances of the solvent in ppm.[3] NMR solvents were obtained packaged under argon and stored over activated molecular sieves.

NMR multiplicities are abbreviated as follows: s = singlet, m = multiplet, br = broad signal.

Electronic absorption spectra were recorded from λ = 220 nm to λ = 2300 nm on a Shimadzu double beam UV-3600 UV/Vis/NIR spectrophotometer in given solvents at room temperature. Cuvettes (117.100-QS) from Hellma with 10 mm layer thickness were used.

IR spectra were recorded on a Shimadzu IRAffinity-1 system in KBr pellets or the solvent stated.

Magnetism data of microcrystalline and powdered samples (10.0–25.0 mg), loaded within a polycarbonate gel capsule inside a plastic straw (Figure S1) or loaded and compressed into a quartz glass holder (Figures S2-S3), with or without Eicosane® (icosane $C_{20}H_{42}$), were collected on a Quantum Design MPMS-3 SQUID magnetometer. The DC moment was recorded in the temperature range of 2–300 K with an applied DC field of 1 T, if not stated otherwise. The DC moment was converted into molar magnetic susceptibility (χ_M) using the following formula (with H = magnetic field, n = moles of substance):

$$\chi_M = \frac{DC\ moment}{H \cdot n}$$

Values of the magnetic susceptibility were corrected for core diamagnetism (χ_{dia}) of the sample and Eicosane® (if used), using tabulated Pascal's constants.[4] Effective magnetic moments (μ_{eff}) were calculated using the following formula (with temperature (T)):

$$\mu_{eff} = 2.828 \cdot \sqrt{(\chi_M - \chi_{dia}) \cdot T}$$

For data simulation and analysis, the program "JulX2", written by Dr. Eckhard Bill (MPI CEC, Mülheim/Ruhr) was used.[5]

Figure S1: Representative picture of a sample, loaded within a polycarbonate gel capsule inside a plastic straw.

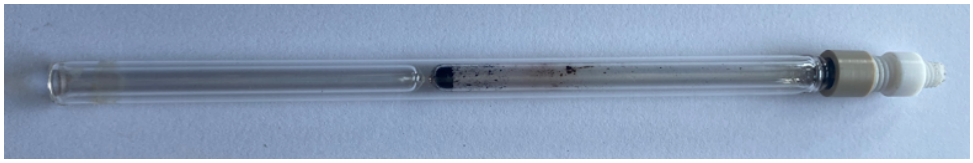

Figure S2: Representative picture of a sample, loaded within an air-tight quartz holder. The sample was compressed with a Teflon™ stick.

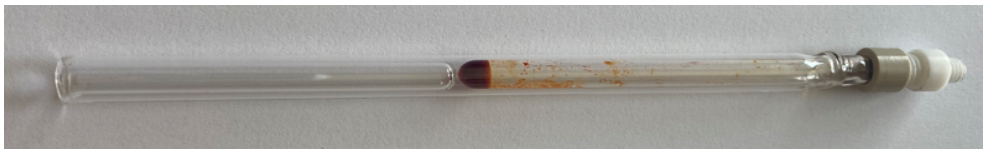

Figure S3: Representative picture of a sample, loaded within an air-tight quartz holder. A defined amount of solid Eicosan® was weighted onto the sample in the holder. The holder was sealed and warmed to 45 °C. The desired "compressed" shape was obtained upon cooling to room temperature.

Elemental analyses were obtained using Euro EA 3000 (Euro Vector) and EA 1108 (Carlo-Erba) elemental analyzers in the Chair of Inorganic and General Chemistry at the Friedrich-Alexander-University Erlangen-Nürnberg (FAU).

Due to the possible formation of (volatile) radioactive uranium fluoride compounds (e.g., UF_6), we are – by regulation and re-strictions – not allowed to conduct elemental analyses on fluoride-containing uranium complexes.

Electrochemical measurements were carried out at room temperature under inert gas atmosphere with an Autolab Type-III potentiostat, recorded in 0.1 M *n*-BuN_4PF_6 ($TBAPF_6$, purchased from Acros and used without further purification) solution in THF, using a glassy carbon working electrode and Pt electrodes as counter and pseudo-reference electrodes. Ferrocene was added as internal standard and all measurements were referenced to E(Fc/Fc+) = 0.41 V *vs.* NHE.

***Caution**: Natural uranium is a radioactive α-emitter; and thus, direct exposure and inhalation must be prevented. Manipulations should be carried out with care in monitored fume hoods or in inert atmosphere gloveboxes in radiation-controlled laboratories equipped with appropriate counting instruments.*

Synthetic and Spectroscopic Details

Synthesis of (1,4,7-tris-(3,5-di-tert-butyl-2-hydroxy-benzyl)-10-methyl-1,4,7,10-tetraaza-cyclododecane), ($^{t\text{-Bu},t\text{-Bu}}$ArOH)$_3$(Me)cyclen

To a room temperature solution of 1-methyl-1,4,7,10-tetraazacyclododecane (0.500 g, 2.68 mmol) and Et_3N (0.890 g, 8.84 mmol) in 100 mL DCM, 1-bromomethyl-3,5-di-*t*-butylphenol (2.25 g, 7.50 mmol) was added dropwise over a period of 30 minutes. After complete addition, the solvent was removed *in vacuo* and the residue was dissolved in Et_2O to yield a colorless solution and a white precipitate that was filtered off. After washing the precipitate with Et_2O, the combined organic phases were evaporated *in vacuo* at 40 °C to obtain the product as white solids. **Yield:** 93% (2.10 g, 2.49 mmol). **^{1}H NMR** (25 °C, 270 MHz, $CDCl_3$): δ = 7.23 – 7.22 (d, $^4J_{HH}$ = 2.7 Hz, 2H, Ar-*H*), 7.16 – 7.15 (d, $^4J_{HH}$ = 2.7 Hz, 1H, Ar-*H*), 6.80 – 6.79 (d, $^4J_{HH}$ = 2.7 Hz, 2H, Ar-*H*), 6.68 – 6.67 (d, $^4J_{HH}$ = 2.7 Hz, 1H, Ar-*H*), 3.62 (s, 4H, CH_2), 3.58 (s, 2H, CH_2), 2.90 (s, 8H, CH_2), 2.65 (t, 4H, CH_2), 2.51 (t, 4H, CH_2), 2.18 (s, 3H, CH_3), 1.44 (s, 18H, *t*-Bu), 1.31 (s, 9H, *t*-Bu), 1.27 (s, 18H, *t*-Bu), 1.25 (s, 9H, *t*-Bu) ppm. **^{13}C NMR:** (25 °C, 67.8 MHz, $CDCl_3$): δ = 154.0 (Ar, 2 C), 153.9 (Ar, 1 C), 140.5 (Ar, 2 C), 140.4 (Ar, 1 C), 135.8 (Ar, 2 C), 135.7 (Ar, 1 C), 123.7 (Ar, 2 C), 123.6 (Ar, 1 C), 122.9 (Ar, 3 C), 121.5 (Ar, 2 C), 121.2 (Ar, 1 C), 60.3 (*C*H_2, 1 C), 60.1 (*C*H_2, 2 C), 52.4 (cyclen, 2 C), 50.8 (cyclen, 4 C), 50.2 (cyclen, 2 C), 42.6 (methyl, 1 C), 34.9 (*t*-Bu, 2 C), 34.8 (*t*-Bu, 1 C), 34.1 (*t*-Bu, 3 C), 31.7 (*t*-Bu, 9 C), 29.7 (*t*-Bu, 6 C), 29.4 (*t*-Bu, 3 C) ppm. **Elemental analysis:** anal. calcd. for $C_{54}H_{88}O_3N_4$: C 77.09%; H 10.54%; N 6.66%. Found: C 75.39%; H 10.28%; N 6.23% (despite multiple attempts, reproducibly low in carbon).

Synthesis of [U^{III}(($OAr^{t\text{-Bu},t\text{-Bu}}$)$_3$(Me)cyclen)] (1)

A precooled solution of [$U^{III}(N(SiMe_3)_2)_3$] (122 mg, 0.170 mmol) in benzene was added dropwise to a precooled solution of ($^{t\text{-Bu},t\text{-Bu}}$ArOH)$_3$(Me)cyclen (143 mg, 0.170 mmol) in benzene and the reaction mixture was immediately evaporated to lyophilize it. After evaporation of the solvent the solid was washed with *n*-pentane until the washing was colorless to obtain the product as purple solids. **Yield:** 65% (120 mg, 0.111 mmol). **^{1}H NMR** (25 °C, 270 MHz, C_6D_6): δ = 15.17, 15.08, 5.17, 5.01, 3.82, 3.64, 0.30, –2.02, –3.18, –4.85, –12.11, –13.29 ppm. **Elemental Analysis:** anal. calcd. for $C_{54}H_{85}O_3N_4U$: C 60.26%; H 7.96%; N 5.21%. Found: C 58.62%; H 7.83%; N 4.69% (despite multiple attempts, reproducibly low in carbon).

Synthesis of [(cyclen(Me)($^{t\text{-Bu},t\text{-Bu}}$ArO)$_3$)U^{IV}(Cl)] (2)

A 20 mL scintillation vial was charged with **1** (60 mg, 0.056 mmol), dissolved in 3 mL THF. A few drops of DCM were added, and the mixture was stirred for three hours. After evaporation of the volatiles, the crude product was washed with *n*-pentane until the washing was colorless to obtain the product as green solids. **Yield:** 76% (47 mg, 0.042 mmol). **^{1}H NMR** (25 °C, 270 MHz, C_6D_6): δ = 44.70, 43.87, 39.48, 35.42, 27.21, 25.92, 14.76, 14.75, 7.31, 4.31, 2.31, 0.12, –0.31, –1.21, –3.70, –4.00, –4.99, –7.23, –7.91, –12.15, –13.85, –13.99, –14.15, –16.27, –16.52, –17.85, –19.03, –50.35, –50.65, –64.65, –67.60, –70.93 ppm. **Elemental Analysis:** anal. calcd. for $C_{54}H_{85}ClO_3N_4U \bullet 0.25\ C_6H_6$: C 58.92%; H 7.71%; N 4.95%. Found: C 58.90%; H 7.66%; N 5.01%.

Synthesis of [(cyclen(Me)($^{t\text{-Bu},t\text{-Bu}}$ArO)$_3$)U^{IV}(F)] (3)

Complex **1** (126 mg, 0.117 mmol) was dissolved in 6 mL THF and AgF (14.8 mg, 0.117) was added. After stirring the mixture for three days the solution was filtered over a Celite® pad and the Celite® was washed with THF until the washing was colorless. The filtrate was evaporated, and the precipitate was dissolved in *n*-pentane. After a few minutes, a green precipitate is formed. The precipitate is filtered off and washed with *n*-pentane two times (1 mL each) to obtain the product as green solids. **Yield:** 36% (46 mg, 0.042 mmol). **^{1}H NMR** (25 °C, 270 MHz, C_4D_8O): δ = 60.78, 57.51, 53.07, 41.53, 33.21, 25.10, 19.06, 18.16, 16.04, 15.92, 14.24, 12.97, 12.68, 12.02, 11.68, 11.23, 4.88, 4.04, 3.83, –1.40, –6.52, –8.46, –9.65, –11.30, –12.07, –12.12, –12.35, –12.86, –14.44, –18.71, –19.72, –52.59, –60.24, –63.35, –65.59 ppm.

Synthesis of [(cyclen(Me)($^{t\text{-Bu},t\text{-Bu}}$ArO)$_3$)U^{IV}(OH)] (4)

A 20 mL scintillation vial was charged with **1** (100 mg, 0.0929 mmol) and dissolved in 10 mL toluene. A solution of H_2O in THF (0.2 M, 0.8 mL) was added and the mixture was stirred overnight. After evaporation of the volatiles the crude product was dissolved in *n*-pentane. After a few minutes, a green precipitate is formed, the precipitate is filtered off and washed with *n*-pentane two times (1 mL each) to obtain the product as green solids. **Yield:** 23% (23 mg, 0.021 mmol). **^{1}H NMR** (25 °C, 270 MHz, C_6D_6): δ = 64.76, 52.95, 48.51, 38.77, 26.31, 20.14, 19.04, 18.67, 18.27, 16.43, 16.27, 15.00, 14.71, 14.26, 13.28, 9.99, 5.16, 5.00, 4.19, 4.03, 3.82, –3.16, –4.33, –7.85, –9.52, –10.34, –12.26, –13.35, –22.07, –24.34, –26.40, –45.31, –51.11, –66.57, –67.77 ppm. **IR (KBr pellet):** $\tilde{\nu}$ (cm^{-1}) = 3675 (m), 2955 (vs), 2900 (vs), 2860 (vs), 1603 (m), 1473 (m), 1444 (m), 1413 (m), 1380 (m), 1359 (m), 1308 (s), 1270

(s), 1203 (m), 1166 (m), 1133 (m), 1081 (m), 1019 (m), 999 (m), 974 (w), 947 (w), 920 (w), 895 (m), 873 (m), 835 (s), 807 (m), 743 (s), 678 (m), 643 (w), 612 (m), 583 (w), 527 (m), 466 (w), 441 (w), 421 (m). **Elemental Analysis**: anal. calcd. for $C_{54}H_{86}O_4N_4U$: C 59.32%; H 7.93%; N 5.12%. Found: C 59.56%; H 7.83%; N 4.82%.

Synthesis of [(cyclen(Me)($^{t\text{-Bu},t\text{-Bu}}$ArO)$_3$)U^{V}(F$_2$)] (5)

Complex **3** (26 mg, 0.024 mmol) was dissolved in 5 mL THF, AgF (6.0 mg, 0.048) was added and the mixture was stirred overnight. The solution was filtered over a Celite® pad and the Celite® was washed with THF until the washing was colorless. The filtrate was evaporated, and the precipitate was dissolved in Et_2O. Storage at –25 °C resulted in a black precipitate that is filtered off to obtain **5** as black solids. **Yield:** 23% (6.0 mg, 0.042 mmol). **^{1}H NMR** (25 °C, 270 MHz, C_6D_6): δ = 17.08, 16.85, 12.88, 12.71, 10.51, 9.85, 9.83, 9.26, 8.87, 8.04, 4.49, 4.31, 3.57, 2.04, 1.87, 1.79, 1.70, 1.64, 1.42, 1.38, 0.30, –0.39, –1.15, –3.29, –4.32, –5.94 ppm.

Synthesis of [(cyclen(Me)($^{t\text{-Bu},t\text{-Bu}}$ArO)$_3$)U^{V}(O)] (6)

A solution of **1** (130 mg, 0.121 mmol) in 8 ml toluene was treated with 1 atm. of N_2O overnight. After evaporation of the volatiles, the crude product was washed with *n*-pentane two times (2 mL each) to obtain the product as orange solids. **Yield:** 61% (80.0 mg, 0.0732 mmol). **^{1}H NMR** (25 °C, 270 MHz, C_6D_6): δ = 15.43, 15.23, 15.04, 13.28, 12.09, 11.65, 5.17, 4.61, 4.53, 3.85, 2.44, 1.66, 0.29, –4.00, –4.84, –10.01, –10.73, –11.09, –12.82, –14.32, –17.71 ppm. **IR** (KBr pellet): $\tilde{\nu}$ (cm^{-1}) = 2958 (vs), 2900 (s), 2861 (s), 1473 (vs), 1441 (vs), 1412 (m), 1380 (m), 1359 (m), 1308 (s), 1269 (vs), 1242 (vs), 1203 (m), 1166 (m), 1135 (m), 1082 (m), 1022 (w), 996 (w), 973 (w), 949 (w), 897 (m), 874 (m), 837 (s), 807 (m), 764 (m), 743 (s), 680 (w), 644 (w), 614 (w), 584 (w), 529 (m), 466 (w), 443 (w), 421 (w). **Elemental Analysis:** anal. calcd. for $C_{54}H_{85}O_4N_4U$: C 59.38%; H 7.84%; N 5.13%. Found: C 59.48%; H 8.06%; N 4.86%.

Synthesis of [(cyclen(Me)($^{t\text{-Bu},t\text{-Bu}}$ArO)$_3$)U^{V}(OH)][SbF$_6$] (7)

A 20 mL scintillation vial was charged with [(($^{t\text{-Bu},t\text{-Bu}}$ArOH)$_3$(Me)cyclen)U^{IV}(OH)] (65 mg, 0.059 mmol) dissolved in 4 mL THF. $AgSbF_6$ (20 mg, 0.059 mmol) was added and the mixture stirred for one hour. The solution was filtered over a Celite® pad and the Celite® was washed with THF until the washing was colorless. After evaporation of the volatiles, the crude product was dissolved in Et_2O and stored at –25 °C until a black precipitate is formed. Filtration of the

solvent yields the product as black solids**. Yield:** 80% (62 mg, 0.047 mmol). **^{1}H NMR** (25 °C, 270 MHz, C_6D_6): δ = 36.04, 33.84, 26.09, 25.93, 23.85, 23.60, 19.93, 18.51, 18.40, 13.75, 12.89, 10.07, 7.87, 7.68, 7.09, 4.48, 4.42, 3.58, 2.60, 1.67, 1.40, 1.04, 0.64, 0.30, –2.39, –3.20, –4.75, –4.85, –6.02, –6.75, –6.91, –8.32, –13.58, –21.07, –22.10, –23.37, –25.41 ppm. **IR** (KBr pellet): $\tilde{\nu}$ (cm^{-1}) = 2957 (s), 2902 (w), 2868 (m), 1601 (m), 1478 (m), 1458 (m), 1444 (m), 1410 (w), 1393 (w), 1361 (m), 1310 (m), 1267 (m), 1230 (s), 1204 (m), 1167 (m), 1130 (m), 1076 (m), 999 (w), 970 (w), 948 (w), 902 (m), 879 (m), 836 (s), 808 (m), 776 (w), 748 (m), 659 (vs), 619 (w), 602 (w), 585 (w), 565 (w), 537 (m), 477 (m), 445 (m), 428 (m).

Synthesis of [(cyclen(Me)($^{t\text{-Bu},t\text{-Bu}}$ArO)$_3$)U^{VI}(O)][$SbF_6$] (8)

A 20 mL scintillation vial was charged with 6 (50 mg, 0.046 mmol) dissolved in 4 mL THF. $AgSbF_6$ (16 mg, 0.046 mmol) was added and the mixture stirred for one hour. The solution was filtered over a Celite® pad and the Celite® was washed with THF until the washing was colorless. After evaporation of the volatiles the crude product was dissolved in Et_2O and stored at –25 °C until a black precipitate is formed. Filtration of the solvent yields the product as black solids. Yield: 39% (41 mg, 0.018 mmol). **^{1}H NMR** (25 °C, 400 MHz, tetrahydrofuran-d8) δ 8.60 (d, $|^2J|$ = 15.0 Hz, 1 H, CH_2-Ar), 7.94 (d, ^4J = 2.4 Hz, 1 H, Ar-H), 7.80 (d, ^4J = 2.4 Hz, 1 H, Ar-H), 7.69 (d, ^4J = 2.3 Hz, 1 H, Ar-H), 7.64 (d, ^4J = 2.3 Hz, 1 H, Ar-H), 7.36 (d, ^4J = 2.3 Hz, 1 H, Ar-H), 7.14 (d, ^4J = 2.3 Hz, 1 H, Ar-H), 7.11 (d, $|^2J|$ = 14.9 Hz, 1 H, CH_2-Ar), 6.65 (d, $|^2J|$ = 14.9 Hz, 1 H, CH_2-Ar), 6.18 (d,$|^2J|$ = 15.0 Hz, 1 H, CH_2-Ar), 5.72 (d, $|^2J|$ = 14.9 Hz, 1 H, CH_2-Ar), 5.46 (d, $|^2J|$ = 14.5 Hz, 1 H, CH_2-Ar), 4.37–3.21 (m, 16 H, CH_2-N), 3.56 (s, 3 H, CH_3-N), 1.72 (s, 9 H, $C(CH_3)_3$), 1.38 (s, 9 H, $C(CH_3)_3$), 1.37 (s, 9 H, $C(CH_3)_3$), 1.30 (s, 9 H, $C(CH_3)_3$), 1.25 (s, 9 H, $C(CH_3)_3$), 1.15 (s, 9 H, $C(CH_3)_3$) ppm. **^{13}C NMR** (25 °C, 101 MHz, tetrahydrofuran-d8) δ 170.23, 167.44, 162.36, 153.54, 150.60, 149.59, 139.41, 138.14, 137.08, 136.10, 135.97, and 135.08 (12 C, Ar-C), 123.34, 122.57, 122.43, 120.44. 120.19, and 117.60 (6 C, Ar-CH), 66.18, 64.89, and 63.24 (3 C, CH_2-Ar), 56.53, 54.66, 54.44, 54.39, 54.30, 53.12, 52.92, and 52.81 (8 C, CH_2-N), 51.64 (1 C, CH_3-N), 35.15 and 34.93 (2 C, $C(CH_3)_3$), 34.56 and 33.94 (6 C, $C(CH_3)_3$), 33.91, 33.75, and 33.32 (3 C, $C(CH_3)_3$), 33.25, 33.10, and 32.91 (9 C, $C(CH_3)_3$), 32.57 (1 C, $C(CH_3)_3$), 32.21 (3 C, $C(CH_3)_3$) ppm. **^{1}H NMR** (25 °C, 270 MHz, C_6D_6): δ = 8.11, 8.07, 8.05, 7.97, 7.76, 7.60, 7.19 7.03, 6.99, 6.67, 6.36, 6.30, 6.05, 6.00, 5.98, 5.56, 5.45, 5.36, 4.78, 4.72, 4.68, 4.57, 4.51, 4.46, 4.04, 3.96, 3.87 3.77, 3.58, 3.50, 3.42, 3.33, 3.28, 3.20, 3.10, 2.87, 2.72 1.80, 1.48, 1.43, 1.32, 1.16, 1.12 ppm.

IR (KBr pellet): $\tilde{\nu}$ (cm^{-1}) = 2960 (s), 2905 (w), 2866 (m), 1598 (m), 1476 (m), 1456 (m), 1444 (m), 1413 (w), 1395 (w), 1361 (m), 1307 (m), 1267 (m), 1230 (s), 1204 (m), 1167 (m), 1130 (m), 1079 (m), 999 (w), 970 (w), 948 (w), 899 (m), 879 (m), 836 (s), 811 (m), 773 (w), 748 (m), 659 (vs), 619 (w), 600 (w), 588 (w), 565 (w), 537 (m), 471 (m), 448 (m), 428 (m).

Synthesis of [K][(cyclen(Me)(*t*-Bu,*t*-BuArO)$_3$)U(O)] (9)

To a solution of **6** (120 mg, 0.915 mmol) in 5 mL benzene, KC_8 (12.0 mg, 0.0915 mmol) was added and the mixture was stirred overnight. The mixture was filtered over a Celite® pad and the Celite® was washed with benzene until the washing was colorless. After evaporation of the volatiles the product was obtained as green solids. **Yield:** 97% (99.0 mg, 0.0445 mmol). **^{1}H NMR** (25 °C, 270 MHz, C_6D_6): δ = 91.50, 61.62, 49.26, 46.22, 40.62, 37.22, 32.66, 31.95, 28.18, 21.91, 19.97, 14.88, 12.93, 11.93, 10.75, 9.69, 7.37, 3.88, 3.78, 3.66, 3.15, 2.10, 1.34, 1.14, 0.95, 0.38, 0.15, –0.25, –0.49, –2.06, –2.38, –3.02, –4.33, –4.67, –4.92, –5.20, – 5.44, –5.29, –8.15, –9.16, –10.93, –12.82, –15.08, –16.14, –17.30, –17.66, –20.24, –21.59, –23.17, –33.69, –36.19, –43.09, –47.81, –57.23, –58.69, –66.48, –72.47 ppm. **Elemental Analysis:** anal. calcd. for $C_{54}H_{85}O_4N_4UK$: C 57.33%; H 7.57%; N 4.95%. Found: C 57.78%; H 7.63%; N 4.63%.

NMR spectroscopy

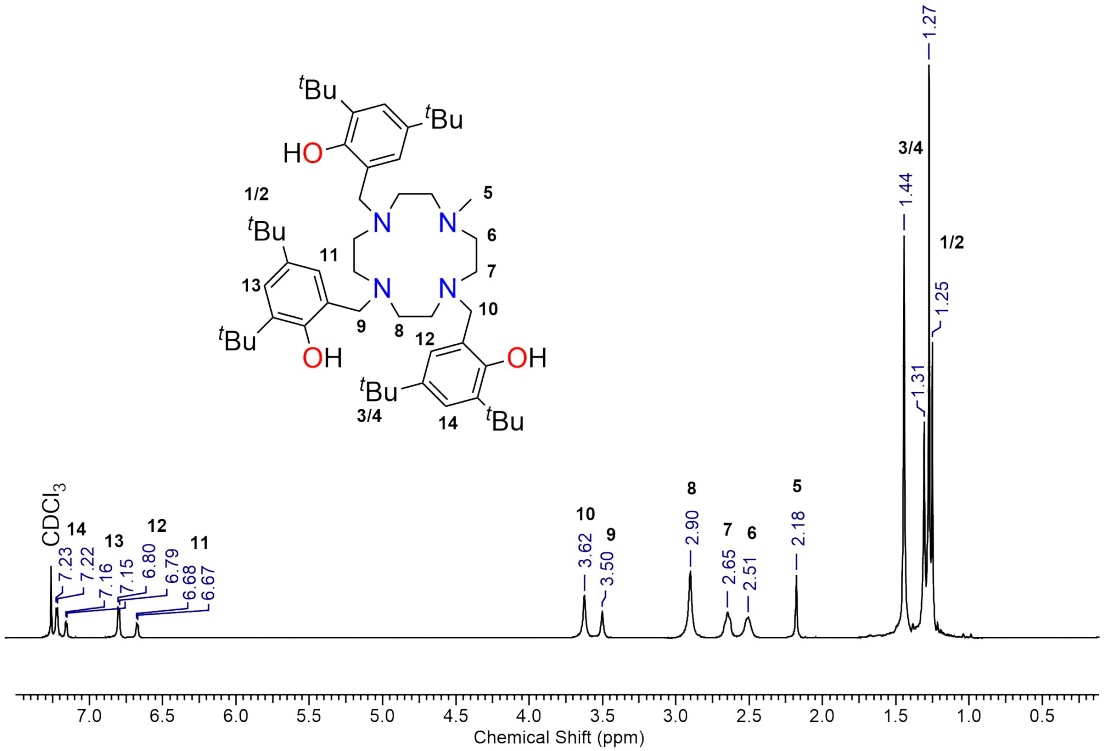

Figure S4: ^{1}H NMR spectrum of (^{t}-Bu,^{t}-BuArOH)$_3$(Me)cyclen, recorded at 270 MHz at room temperature in $CDCl_3$.

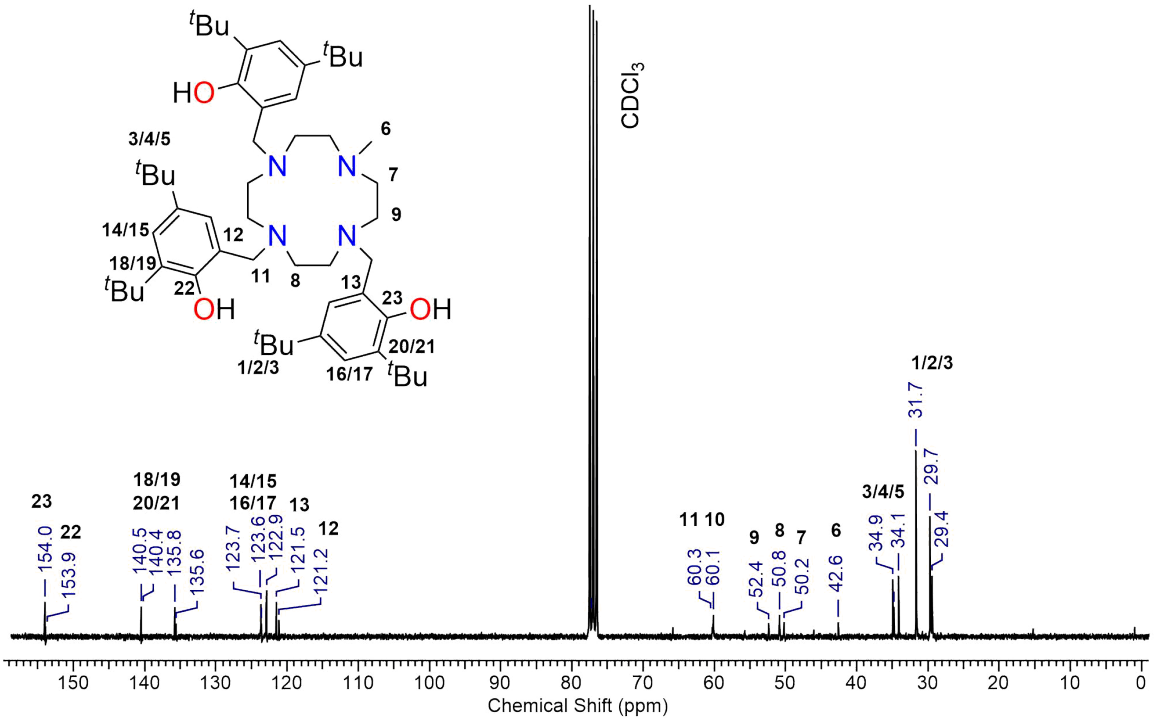

Figure S5: ^{13}C NMR spectrum of (^{t}-Bu,^{t}-BuArOH)$_3$(Me)cyclen, recorded at 68 MHz at room temperature in $CDCl_3$.

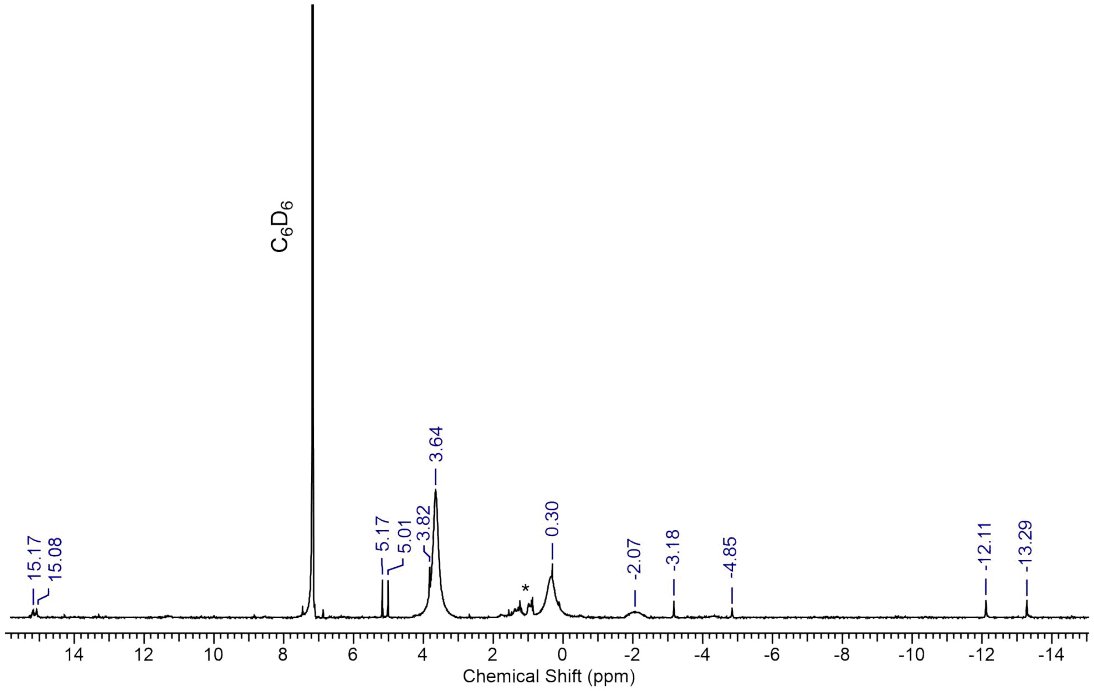

Figure S6: ^{1}H NMR spectrum of the U(III) precursor complex **1**, recorded at 270 MHz at room temperature in benzene-d_6.

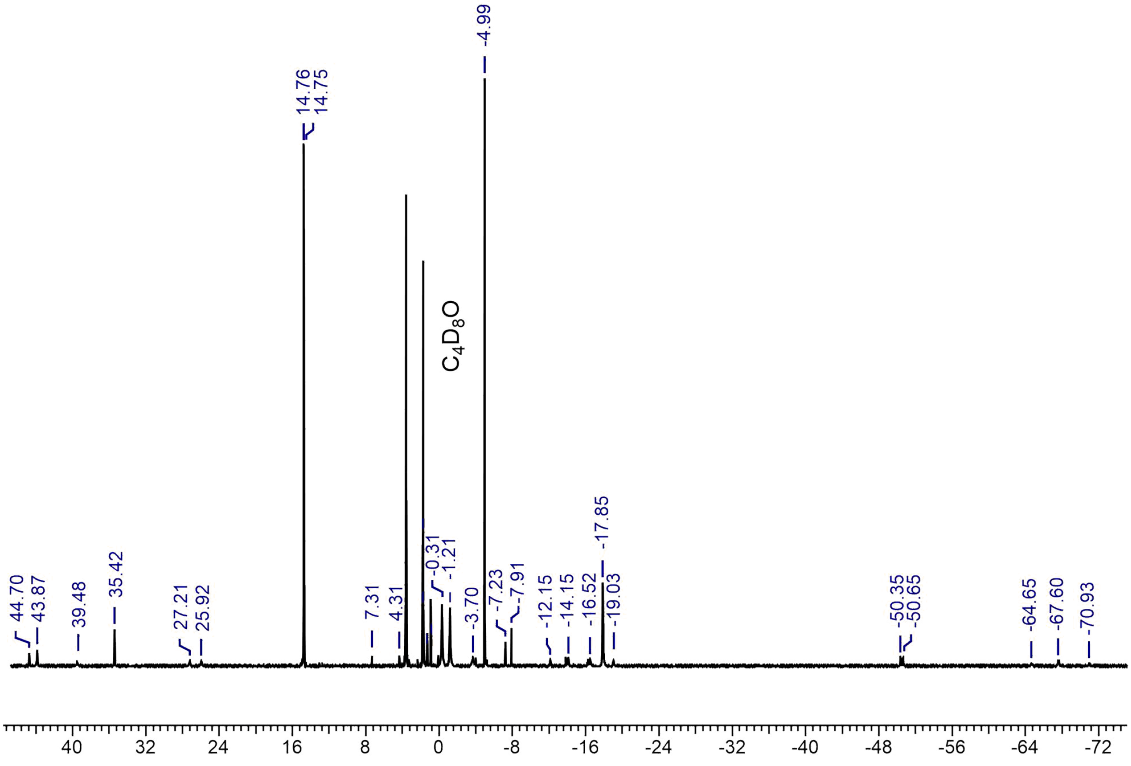

Figure S7: ^{1}H NMR spectrum of the U(IV) chlorido complex **2**, recorded at 270 MHz at room temperature in THF-d_8.

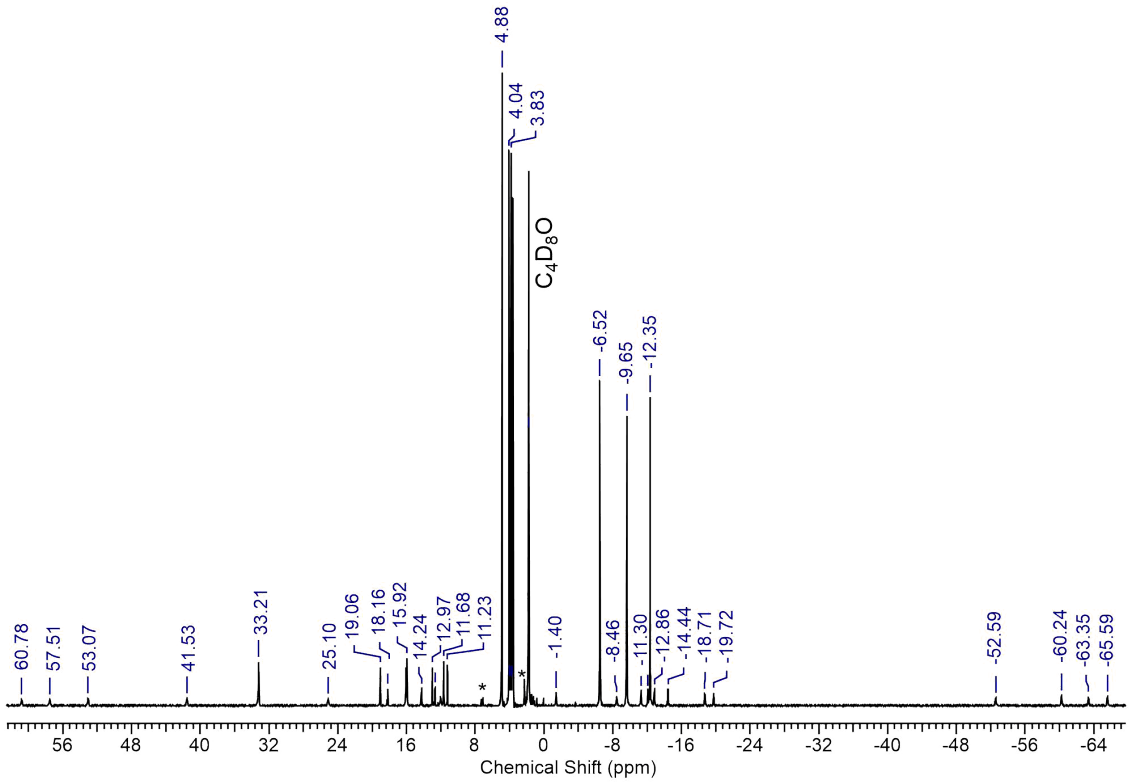

Figure S8: ^{1}H NMR spectrum of the U(IV) fluorido complex **3**, recorded at 270 MHz at room temperature in THF-d_8. Toluene impurities are marked with *.

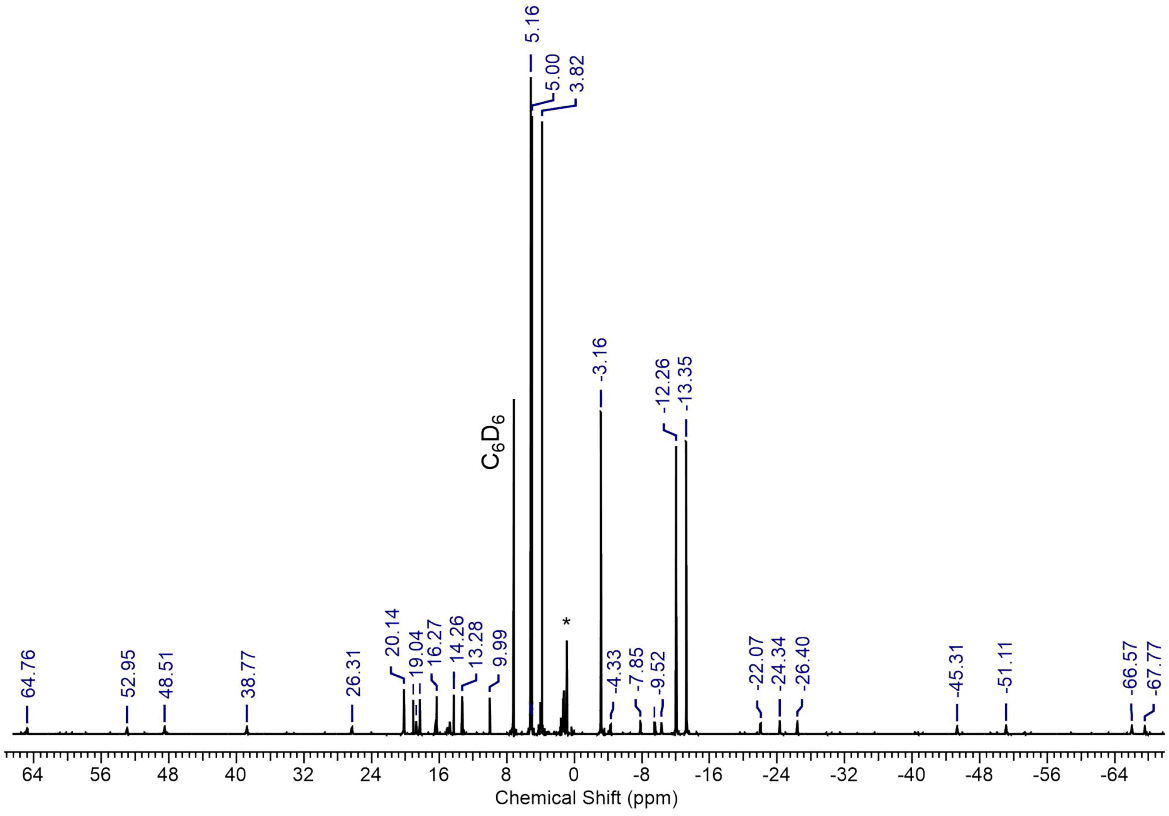

Figure S9: ^{1}H NMR spectrum of the U(IV) hydroxido complex **4**, recorded at 270 MHz at room temperature in benzene-d_6. *n*-Pentane impurities are marked with *.

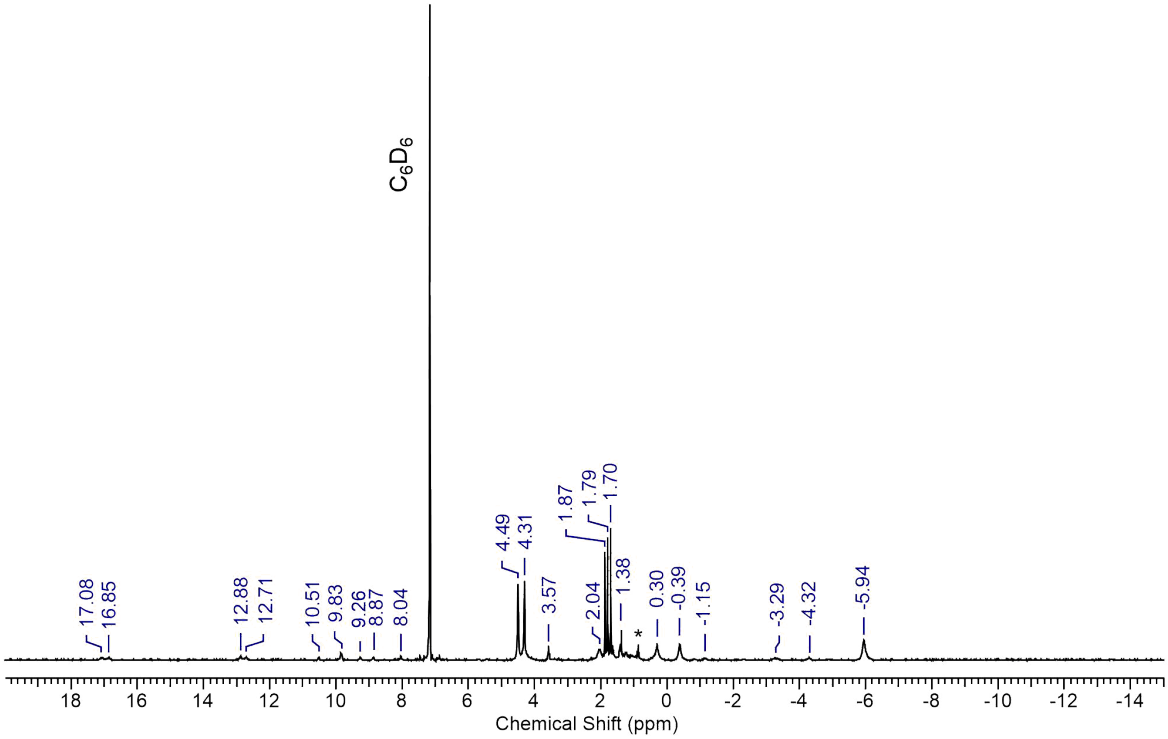

Figure S10: ^{1}H NMR spectrum of the U(V) difluorido complex **5**, recorded at 270 MHz at room temperature in benzene-d_6. *n*-Pentane impurities are marked with *.

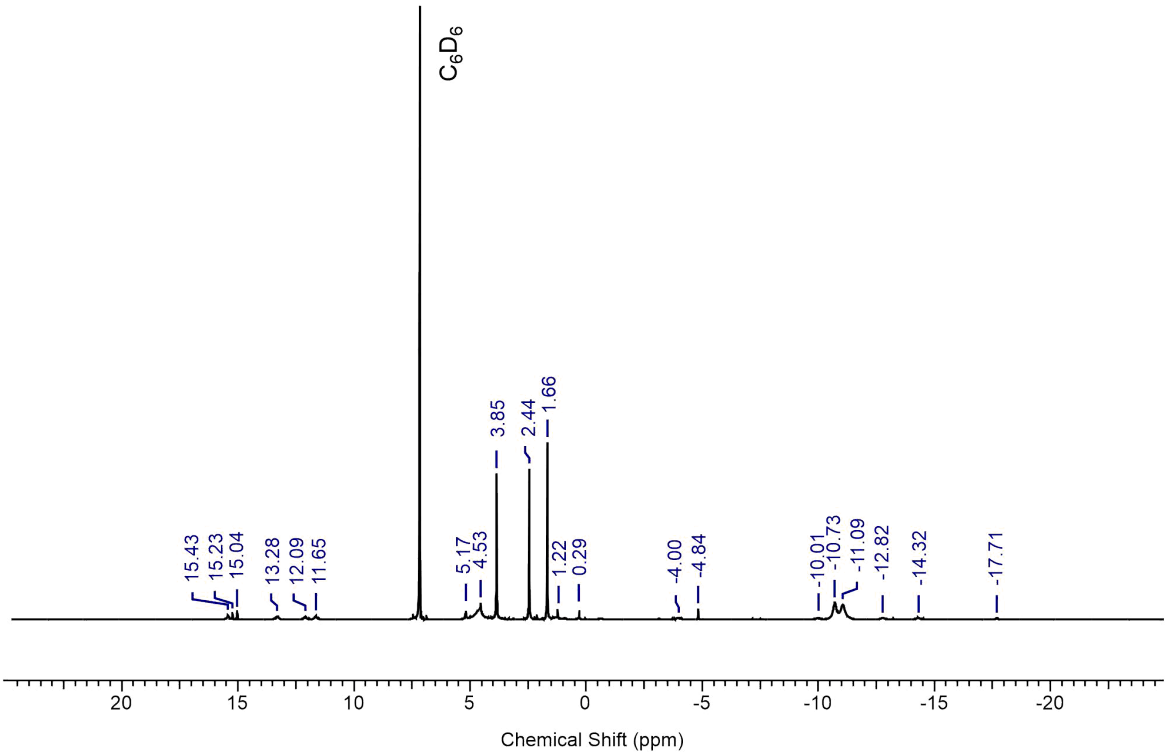

Figure S11: : ^{1}H NMR spectrum of the U(V) oxido complex **6**, recorded at 270 MHz at room temperature in benzene-d_6.

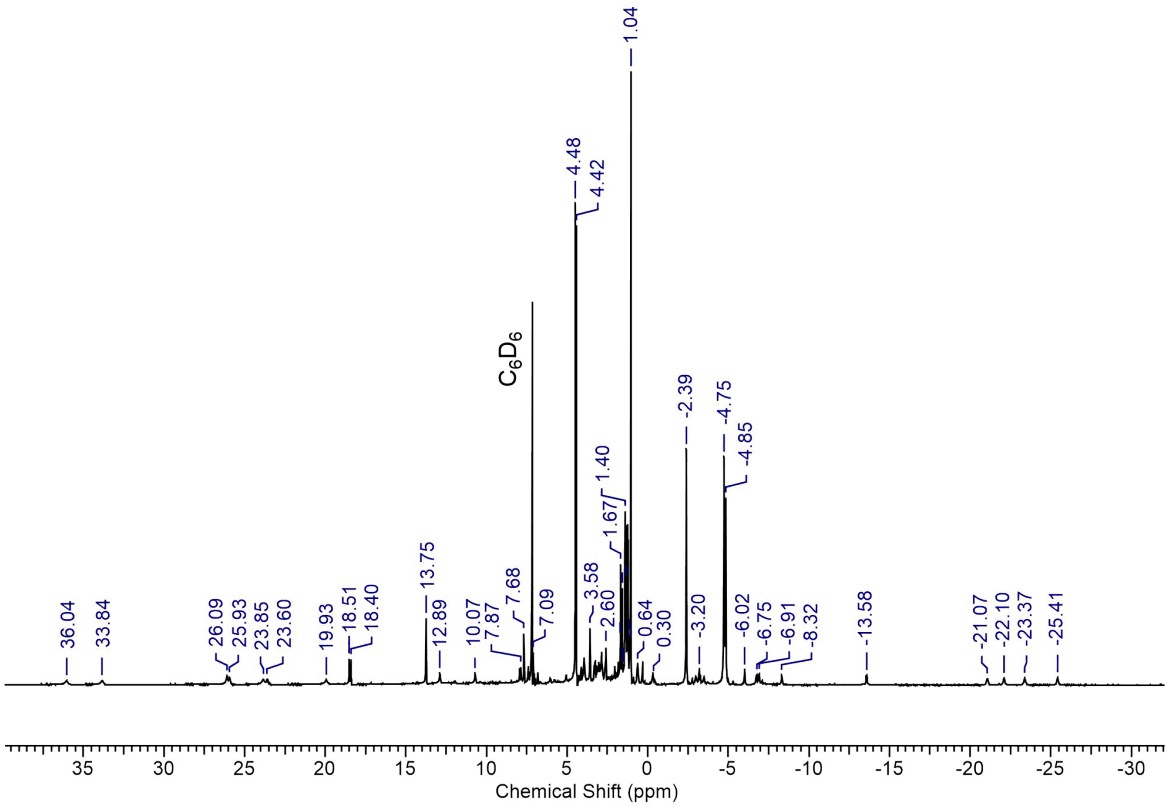

Figure S12: ^{1}H NMR spectrum of the U(V) hydroxido complex **7**, recorded at 270 MHz at room temperature in benzene-d_6.

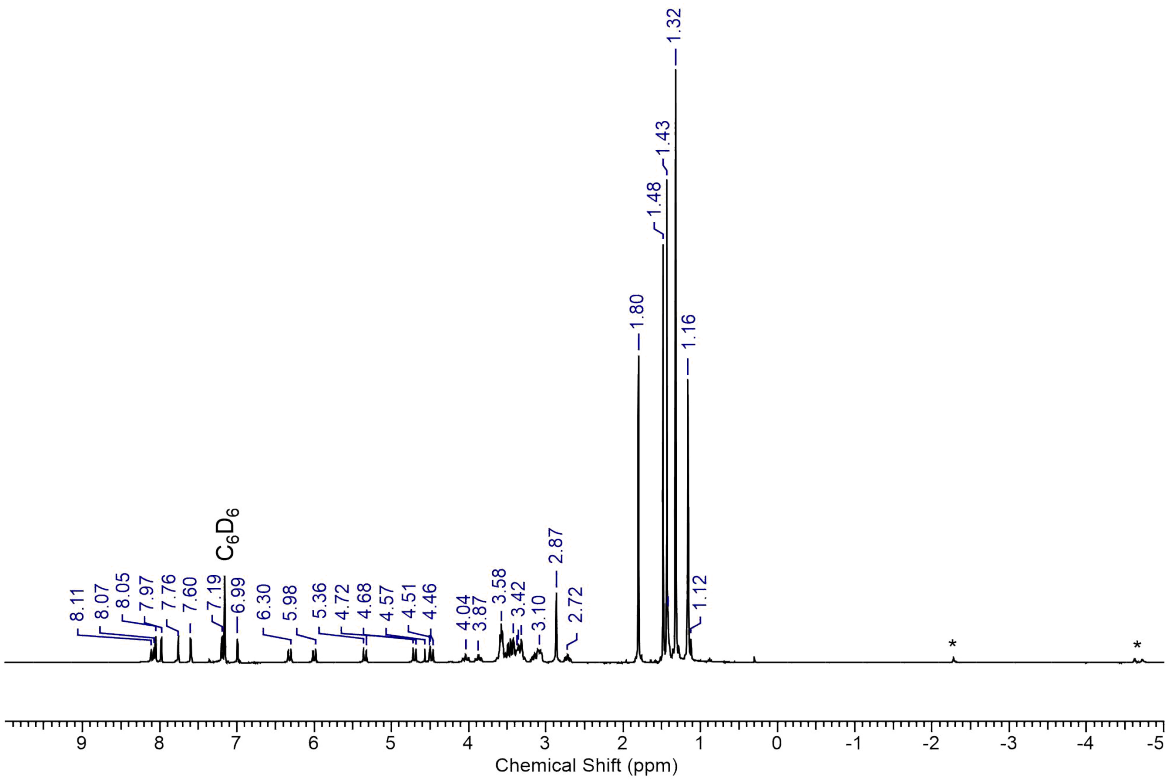

Figure S13: ^{1}H NMR spectrum of the U(VI) oxido complex **8**, recorded at 270 MHz at room temperature in benzene-d_6. Paramagnetic impurities are marked with *.

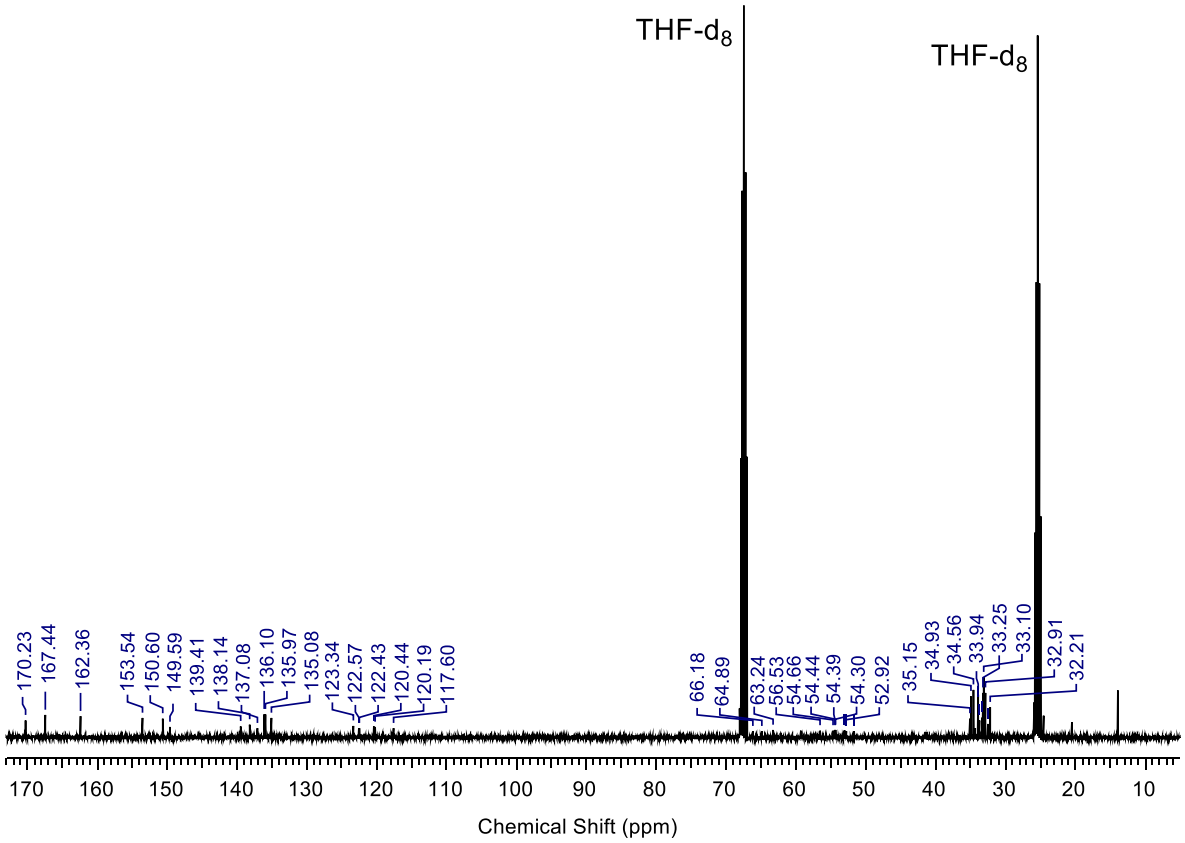

Figure S14: ^{13}C NMR spectrum of the U(VI) oxido complex **8**, recorded at 101 MHz at room temperature in THF-d_8.

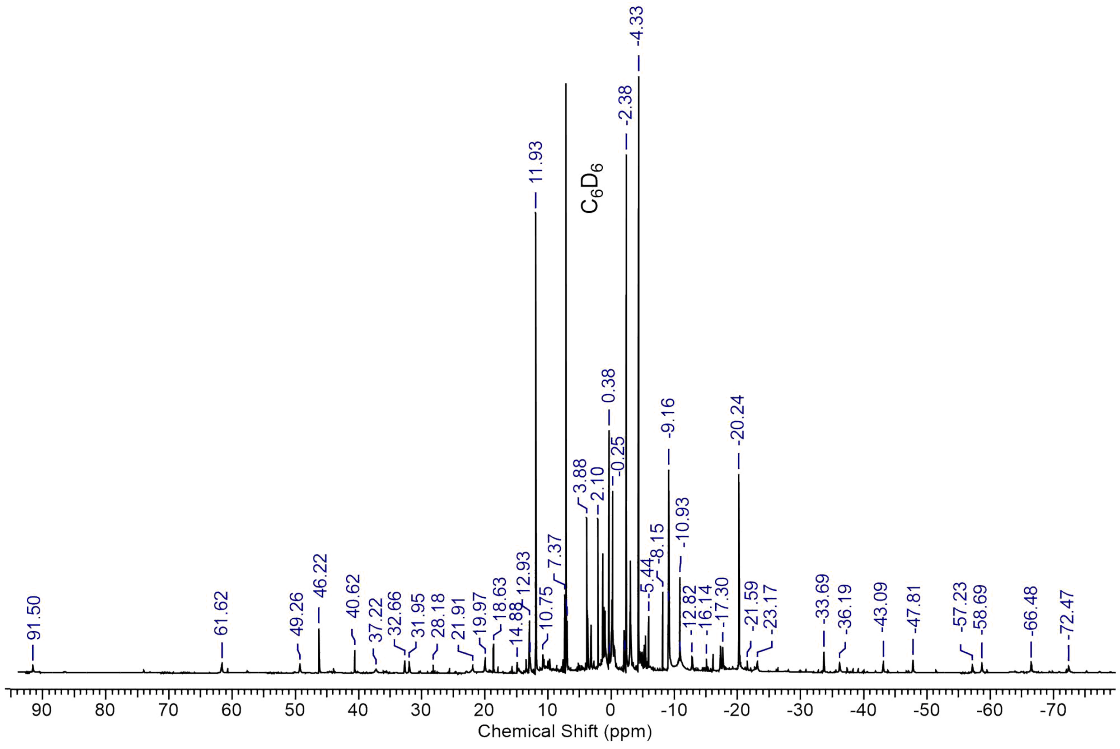

Figure S15: ^{1}H NMR spectrum of the U(IV) oxido complex **9**, recorded at 270 MHz at room temperature in benzene-d_6.

Assignment of the paramagnetic impurity in samples of complex 8

The paramagnetic impurity turned out to be the U(V) hydroxo complex **7**. This was identified with two samples of **7** (green line) and **8** (red line), measured in benzene-d_6. The first three figures S16 - S18 show the 6 signals of the t-butyl groups of **7** (see also Figure S19 for full spectrum), which can also be detected in the spectrum of **8** due to their high intensity.

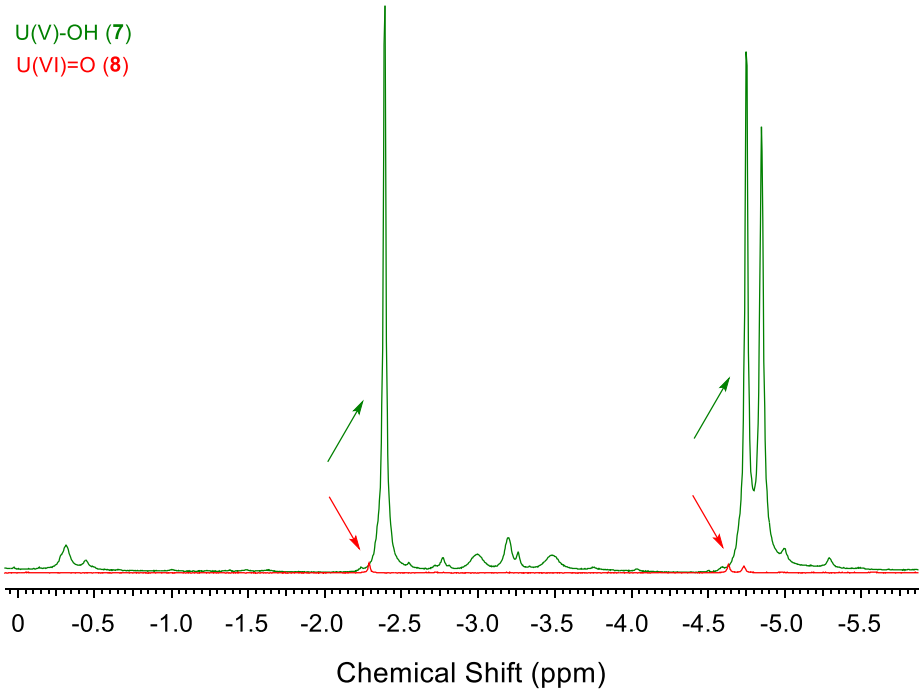

Figure S16: Zoom of the ^{1}H NMR spectrum of **7** (green) and **8** (red), recorded at 270 MHz at room temperature in benzene-d_6 with three of the six t-butyl signals of **7**.

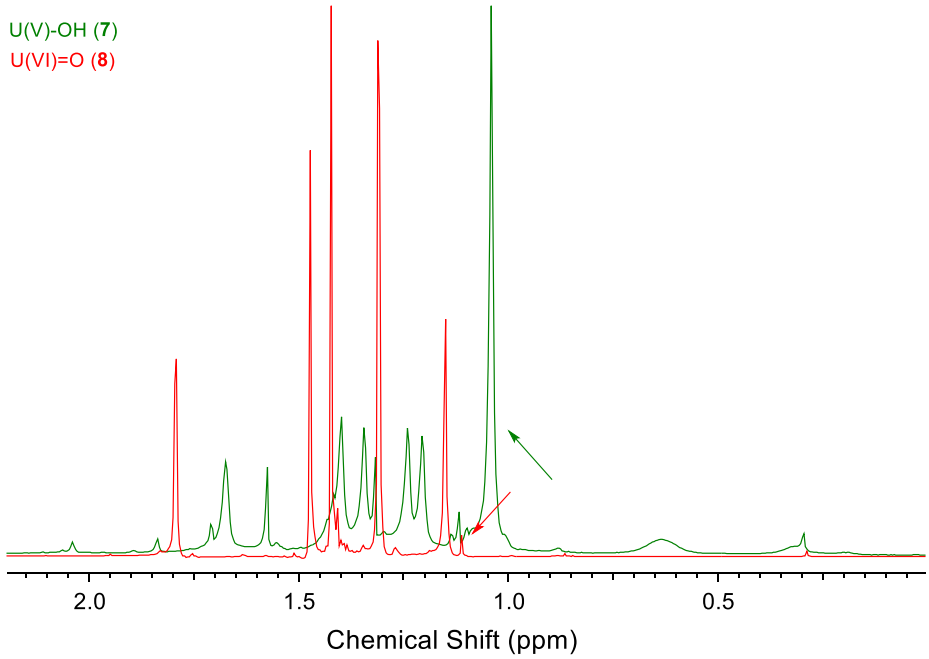

Figure S17: Zoom of the ^{1}H NMR spectrum of **7** (green) and **8** (red), recorded at 270 MHz at room temperature in benzene-d_6 with one of the six t-butyl signals of **7**.

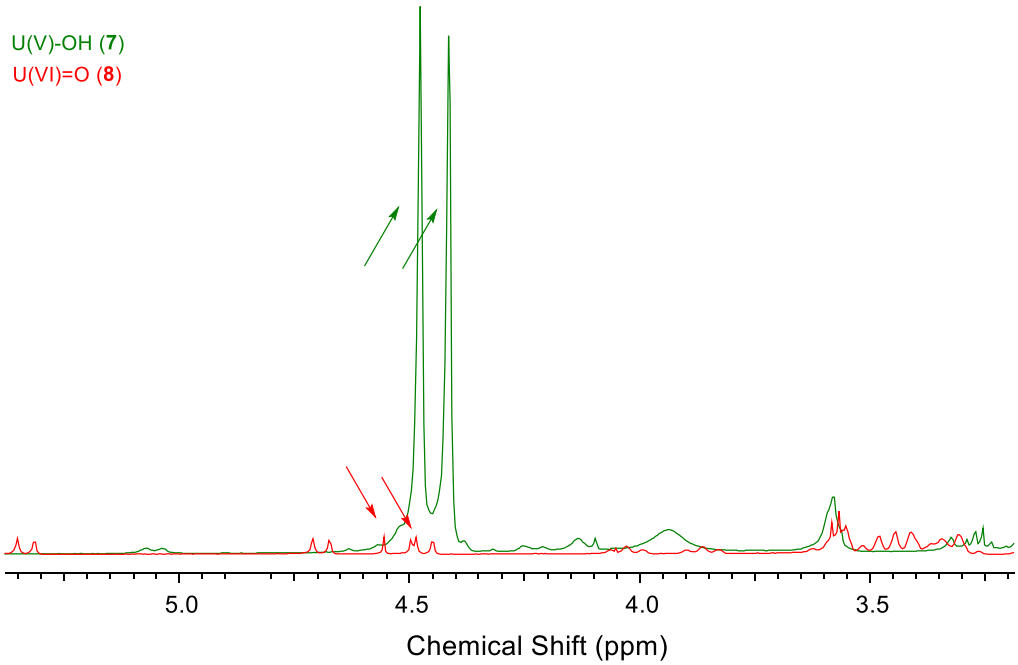

Figure S18: Zoom of the ^{1}H NMR spectrum of **7** (green) and **8** (red), recorded at 270 MHz at room temperature in benzene-d_6 with two of the six t-butyl signals of **7**.

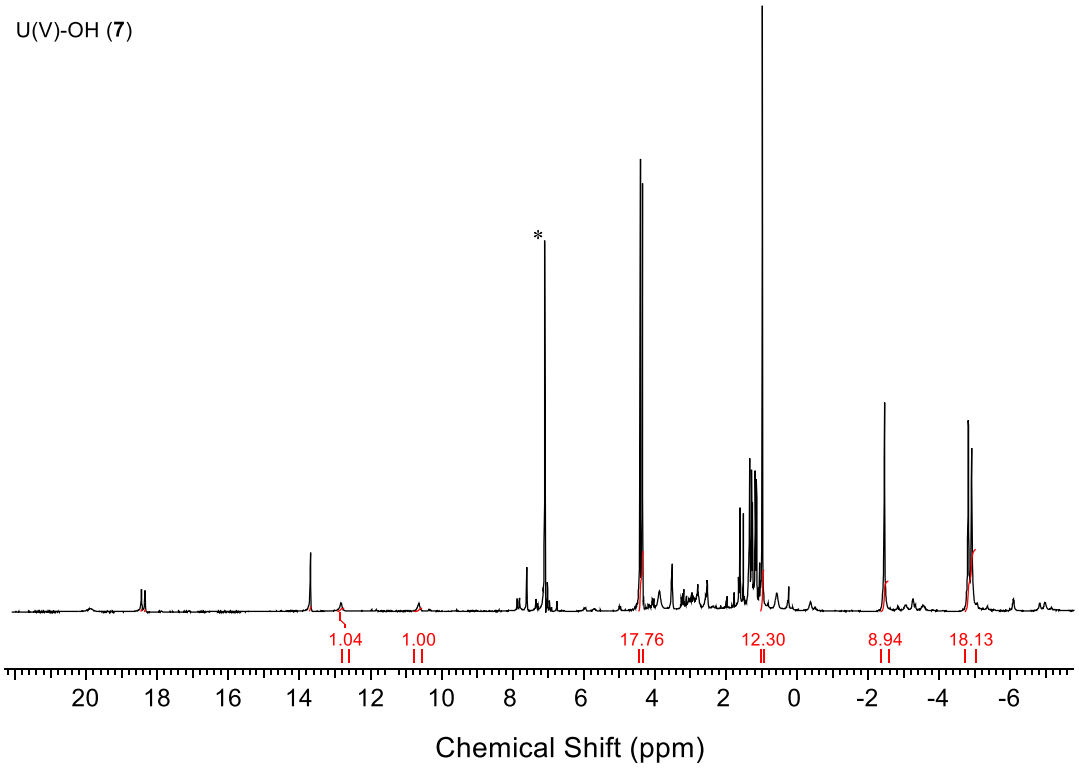

Figure S19: ^{1}H NMR spectrum of **7**, recorded at 270 MHz at room temperature in benzene-d_6 (*). The spectrum shows the integration and detection of the six signals of the t-butyl groups.

With this information, the minor impurities of **7** in the spectrum of **8** accounted for 3%, according to the integration of the t-butyl signals (Figure S20). Even in a solid sample of **8**, after 3 weeks stored at –30 °C, the impurity **7** increases up to 20% (Figure S21, measured in THF-d_8).

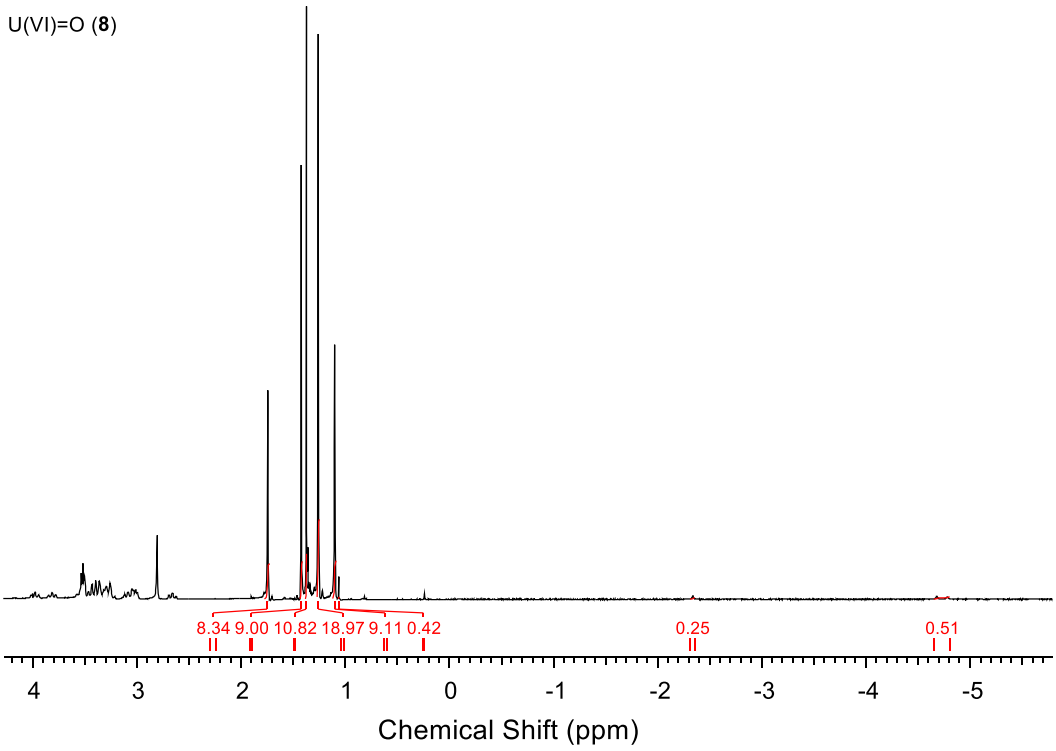

Figure S20: ^{1}H NMR spectrum of **8**, recorded at 270 MHz at room temperature in benzene-d_6 (*). The spectrum shows the integration and detection of the six signals of the t-butyl groups.

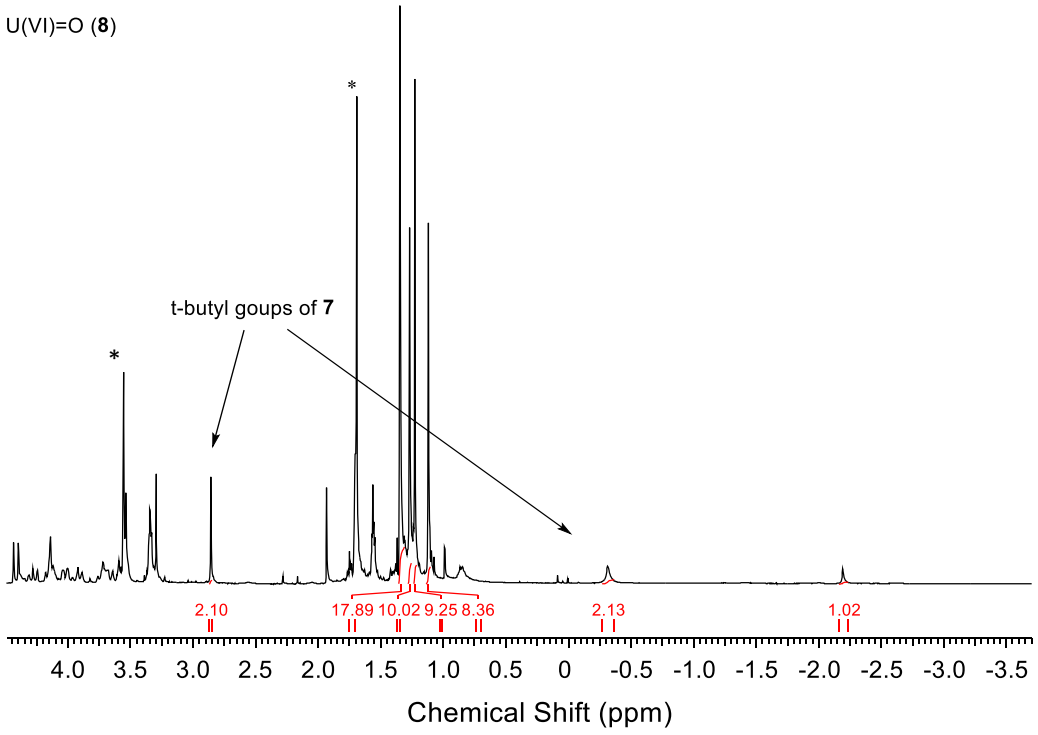

Figure S21: ^{1}H NMR spectrum of **8**, recorded at 400 MHz at room temperature in THF-d_8 (*). The spectrum shows the integration and detection of two signals of the six t-butyl groups.

VT ^{1}H NMR studies between –90 °C and 25 °C were performed. It is shown that the diamagnetic signals of **8** shift insignificantly. As expected, the paramagnetic signals of the impurity (**7**), however, do shift significantly (Figure S22).

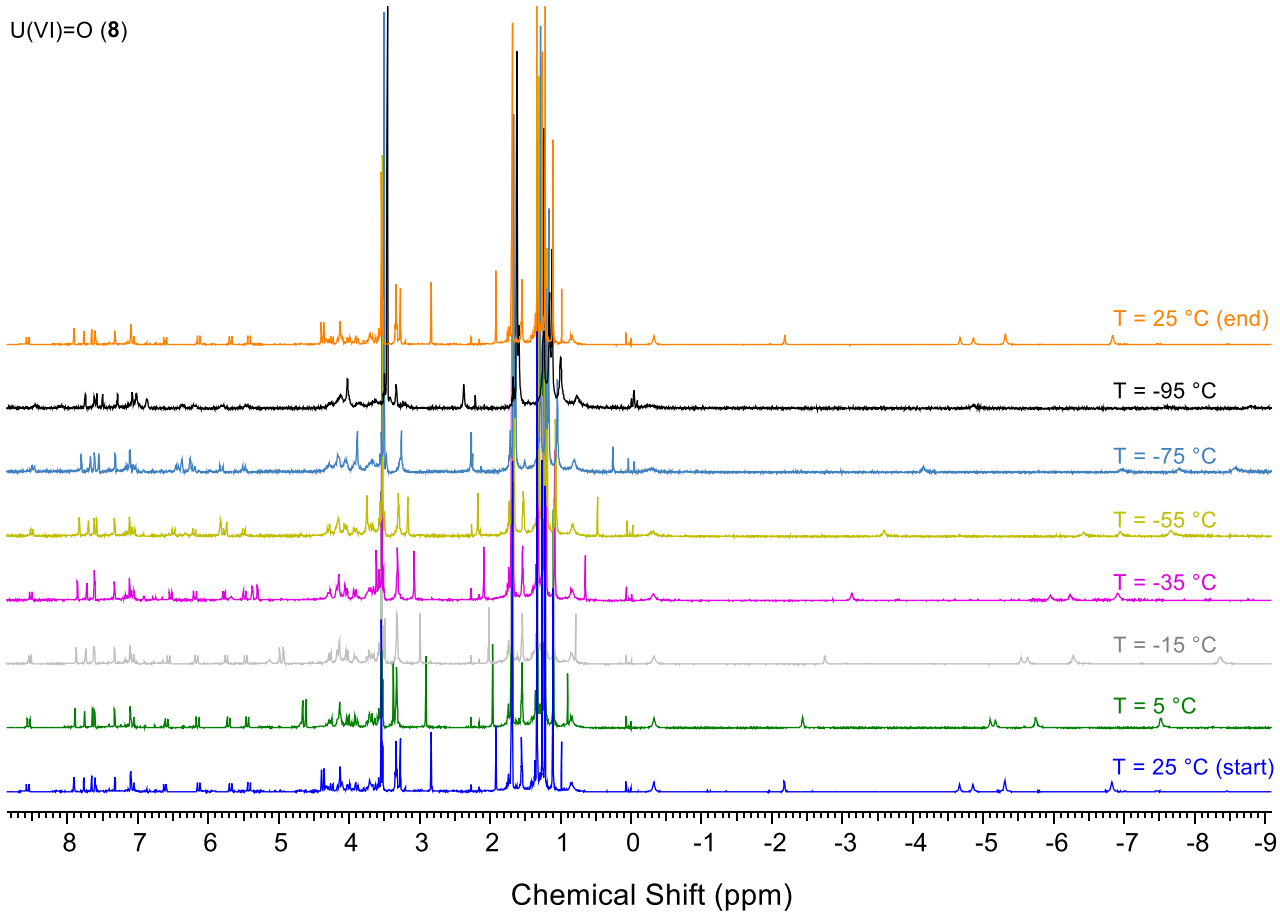

Figure S22: VT ^{1}H NMR spectra of complex **8**, measured in THF-d_8.

We collected data at our group's routine 400 MHz NMR spectrometer and a benchtop 80 MHz instrument. We found that the chemical shifts of **8** are not field dependent (Figure S23); further suggesting that the additional signals stem from an impurity rather than TIP and/or an excited state.

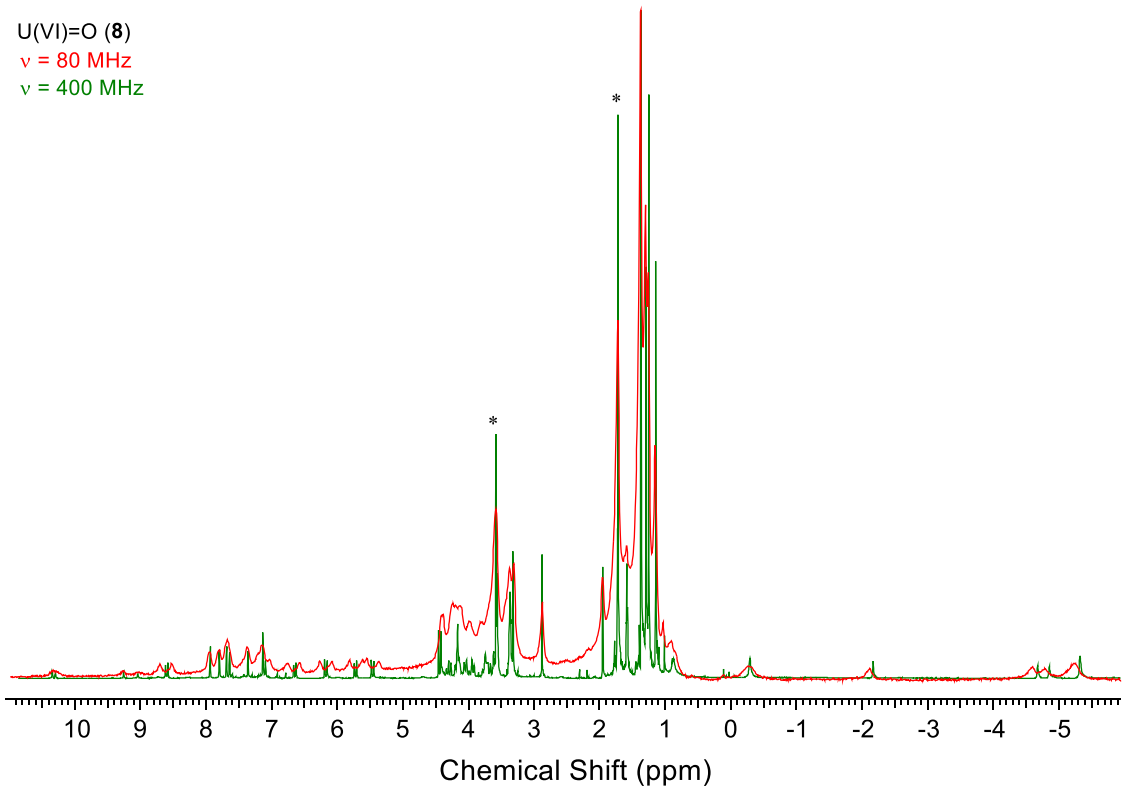

Figure S23: ^{1}H NMR spectra of **8**, recorded at 80 Mhz and 400 MHz, respectively, at room temperature in THF-d_8 (*).

IR Vibrational Spectroscopy

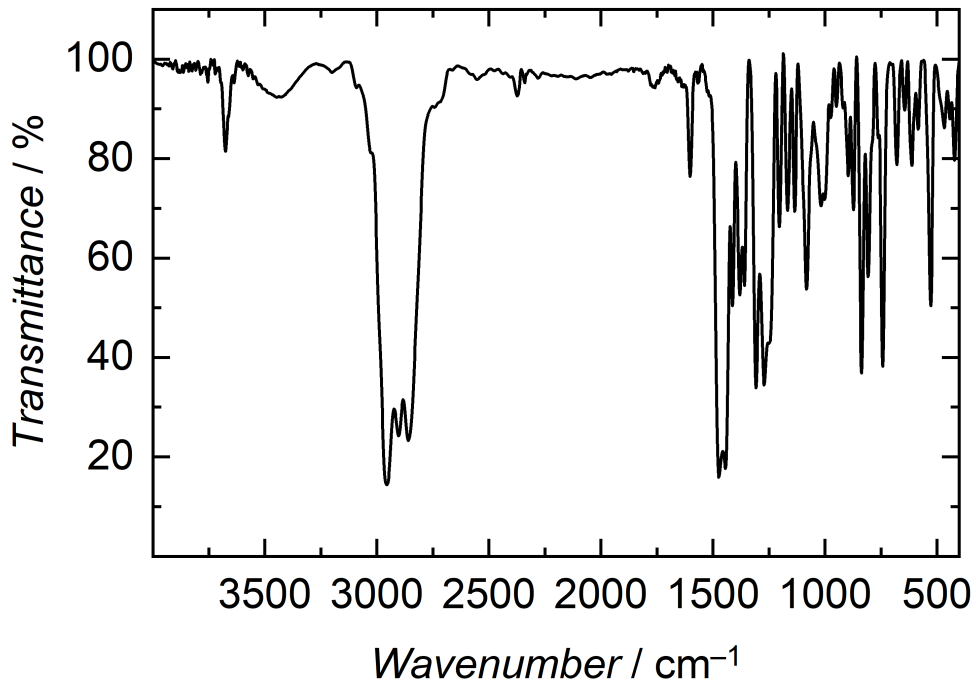

Figure S24: Infrared vibrational spectrum of **4**, recorded as KBr pellet.

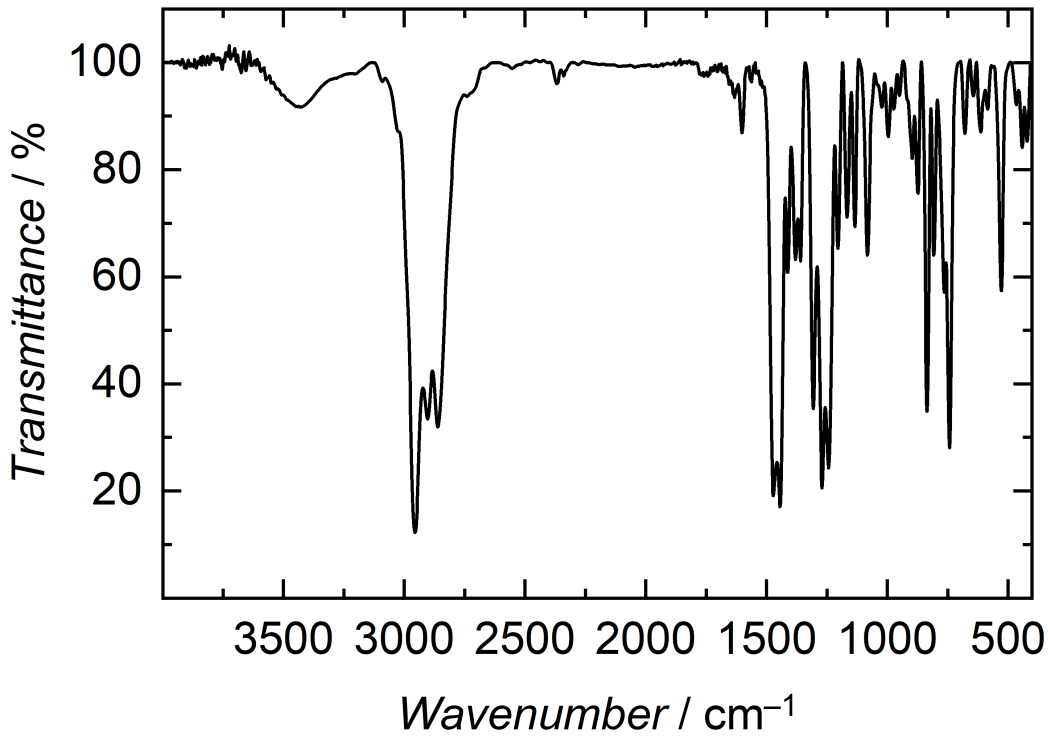

Figure S25: Infrared vibrational spectrum of **6**, recorded as KBr pellet.

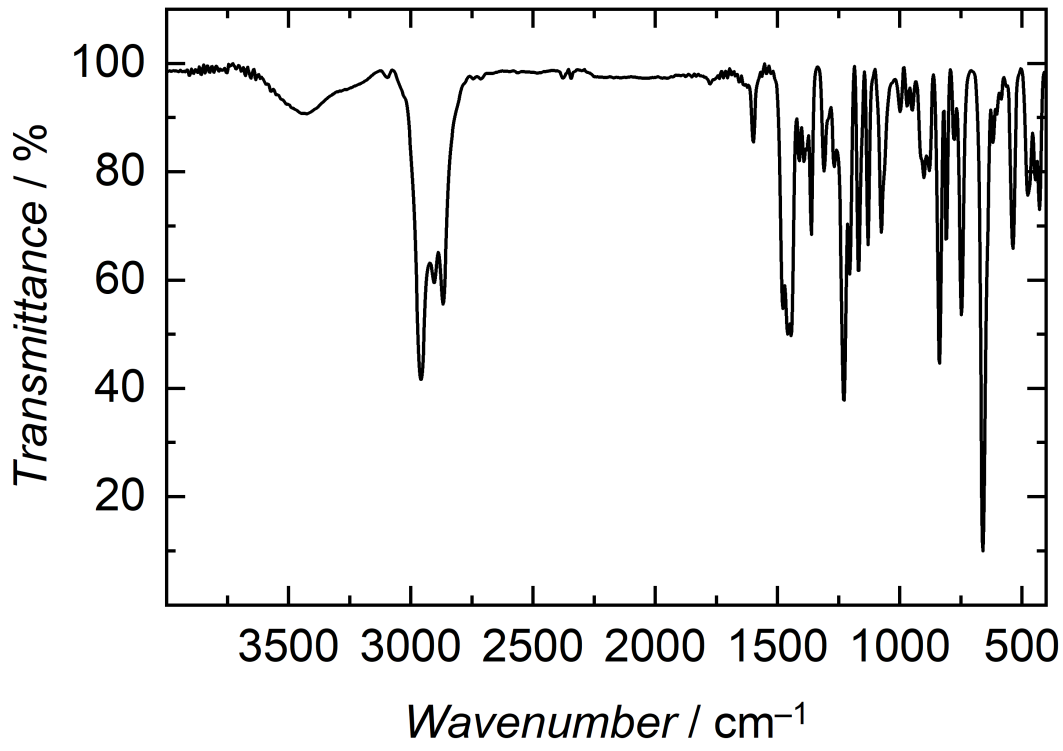

Figure S26: Infrared vibrational spectrum of **7**, recorded as KBr pellet.

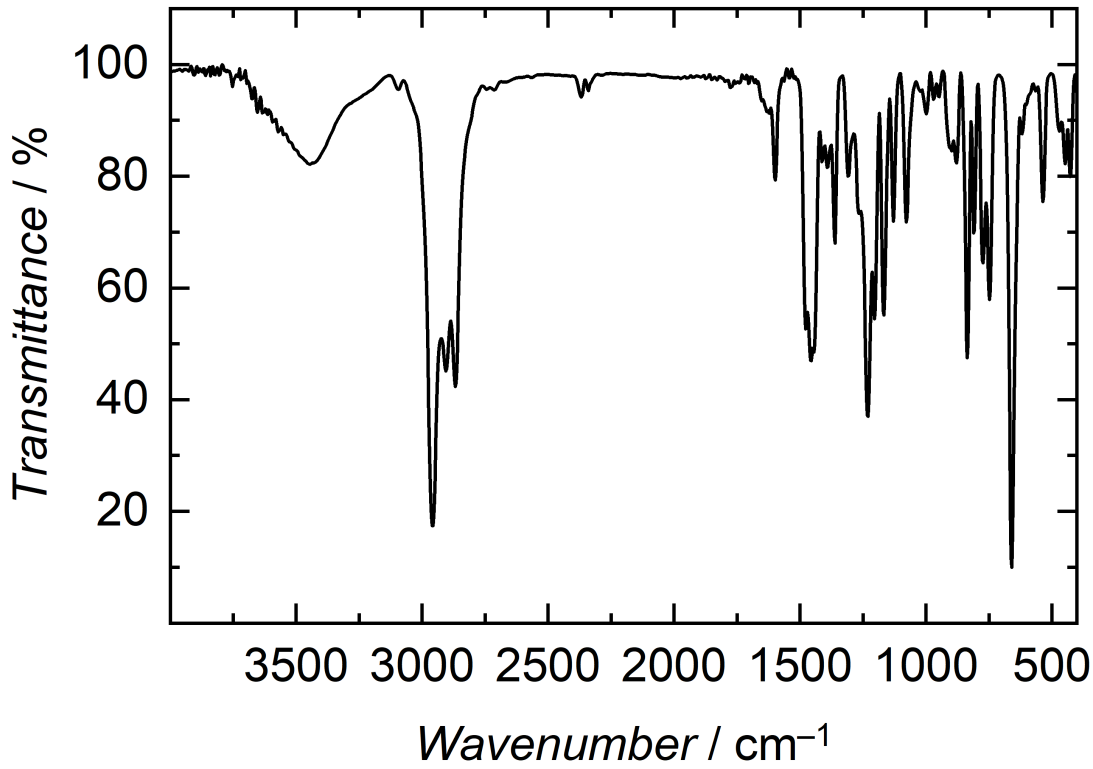

Figure S27: Infrared vibrational spectrum of **8**, recorded as KBr pellet.

UV/Vis/NIR Electronic Absorption Spectroscopy

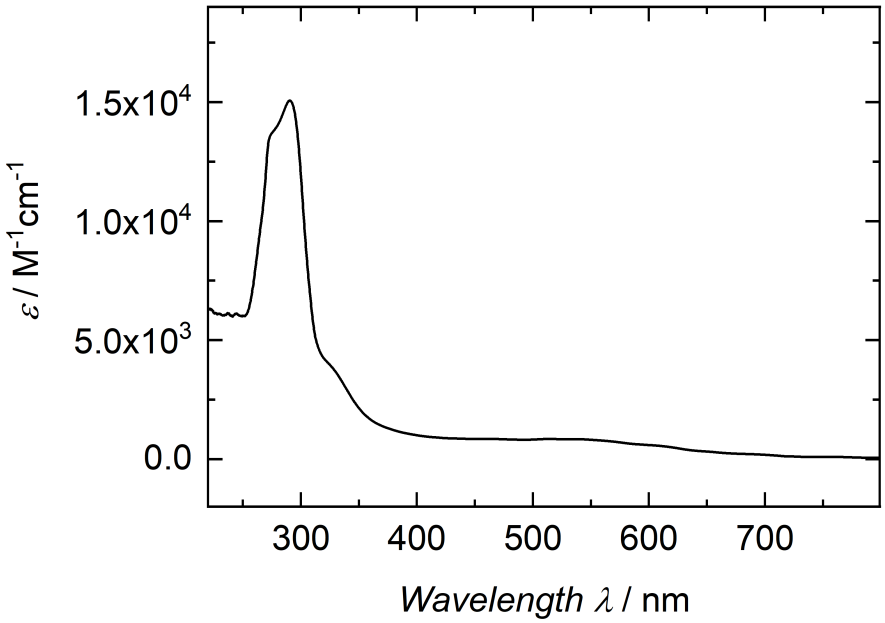

Figure S28: UV/Vis electronic absorption spectrum of **1**, recorded in a 0.17 mM benzene solution.

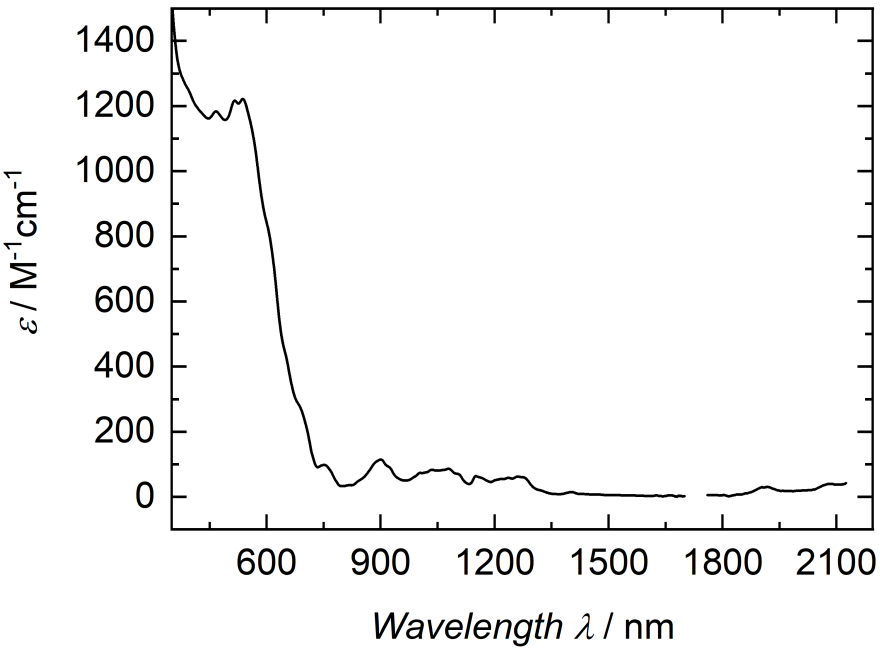

Figure S29: Vis/NIR electronic absorption spectrum of **1**, recorded in a 1.7 mM benzene solution. Data points from 1700 nm to 1760 nm are omitted due to a detector change from a PbS to an In/Ga/As detector.

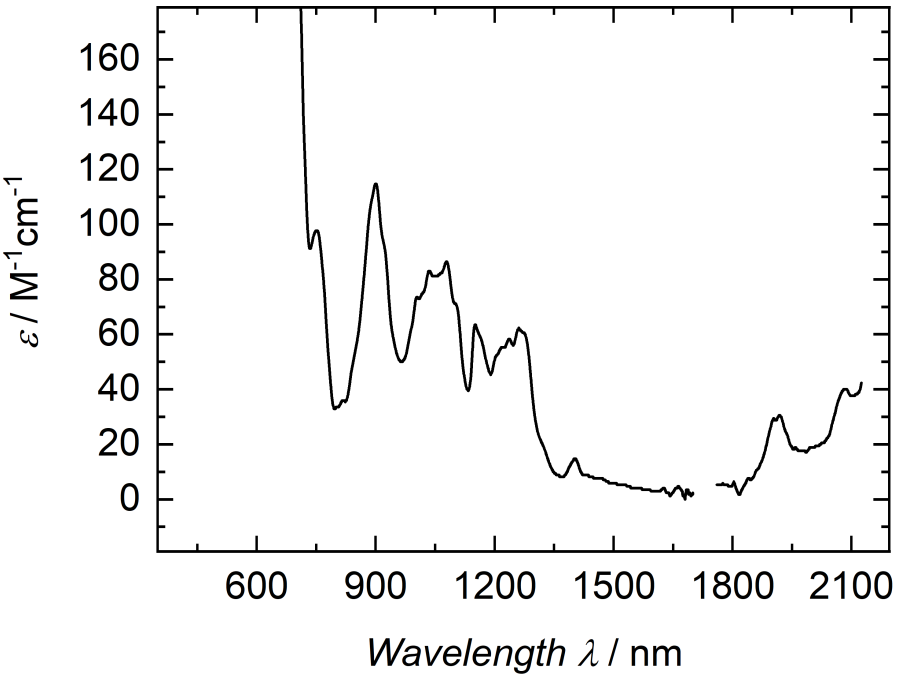

Figure S30: Vis/NIR electronic absorption spectrum of **1**, recorded in a 1.7 mM benzene solution. Data points from 1700 nm to 1760 nm are omitted due to a detector change from a PbS to an In/Ga/As detector.

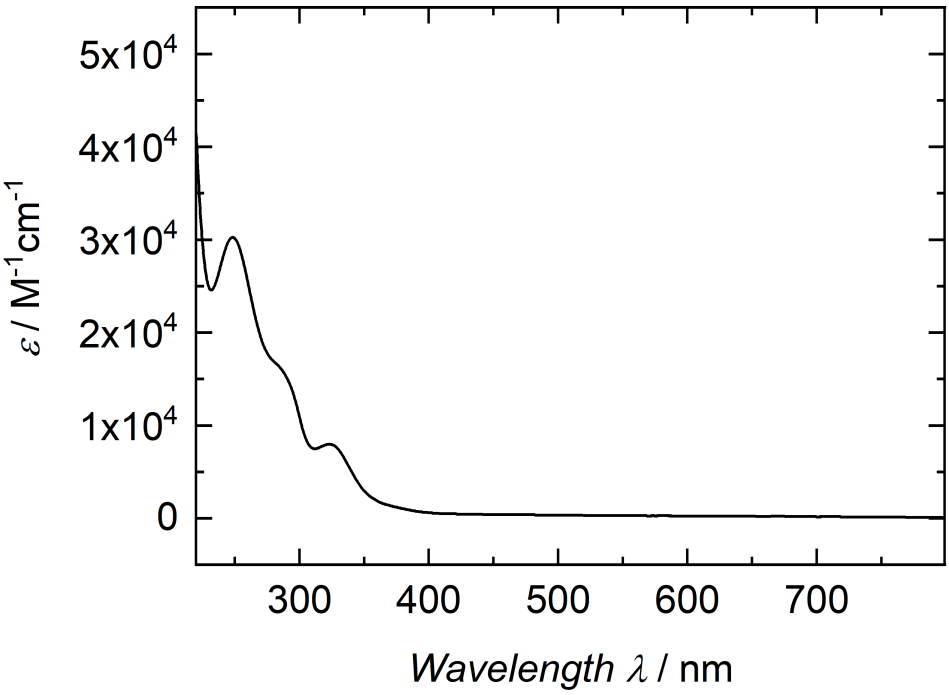

Figure S31: UV/Vis electronic absorption spectrum of **2**, recorded in a 0.02 mM THF solution.

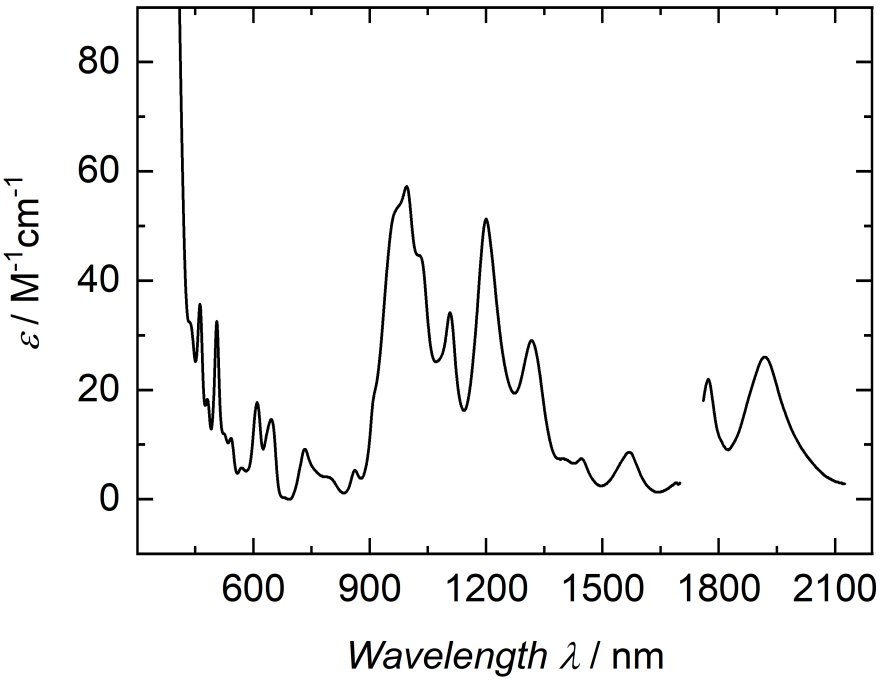

Figure S32: Vis/NIR electronic absorption spectrum of **2**, recorded in a 7 mM THF solution. Data points from 1700 nm to 1760 nm are omitted due to a detector change from a PbS to an In/Ga/As detector.

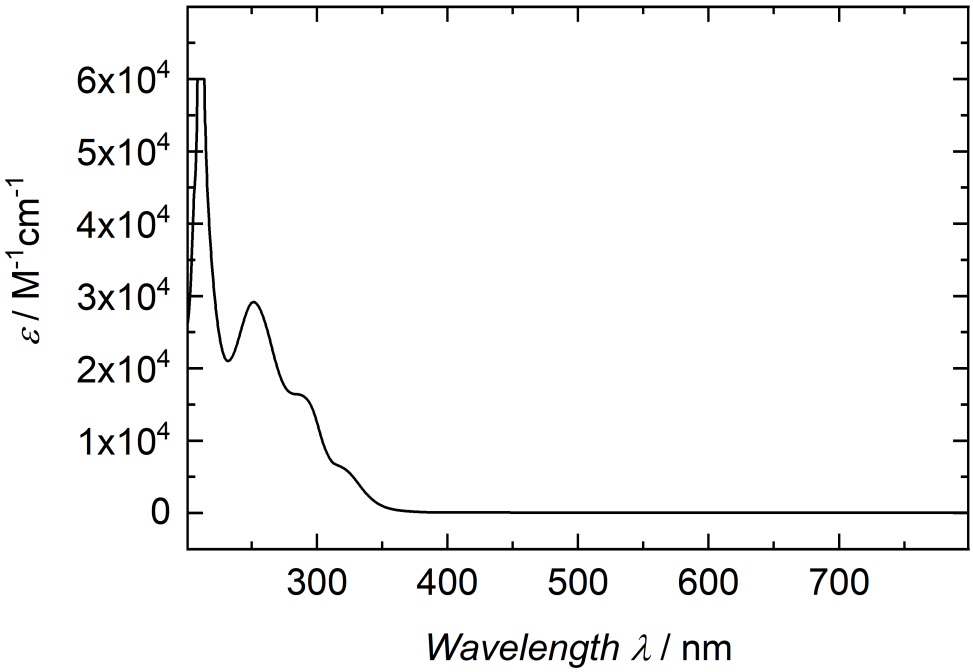

Figure S33: UV/Vis electronic absorption spectrum of **3**, recorded in a 0.1 mM THF solution.

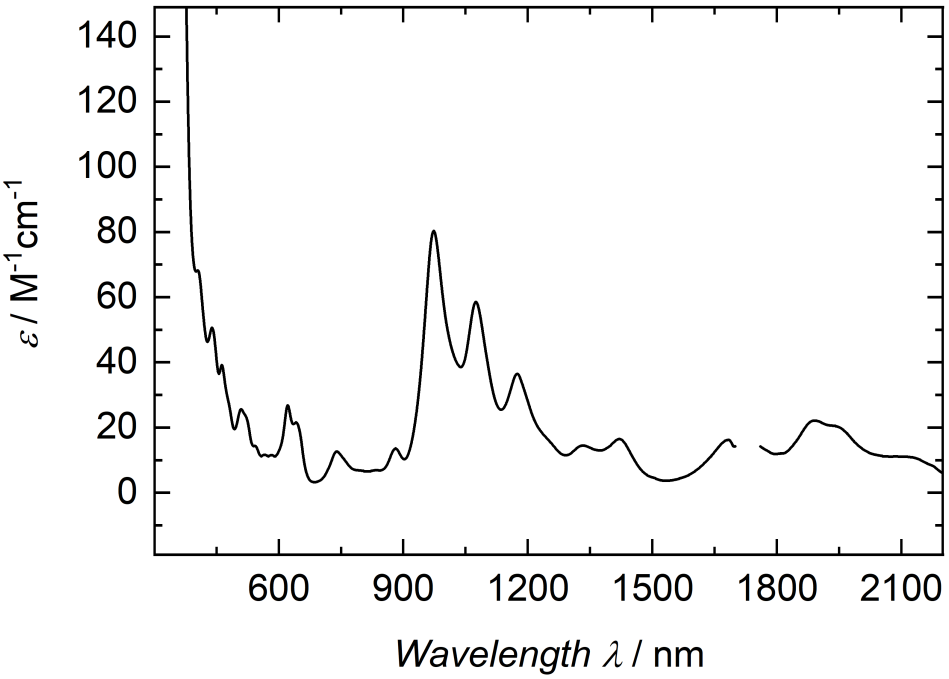

Figure S34: Vis/NIR electronic absorption spectrum of **3**, recorded in a 10 mM THF solution. Data points from 1700 nm to 1760 nm are omitted due to a detector change from a PbS to an In/Ga/As detector.

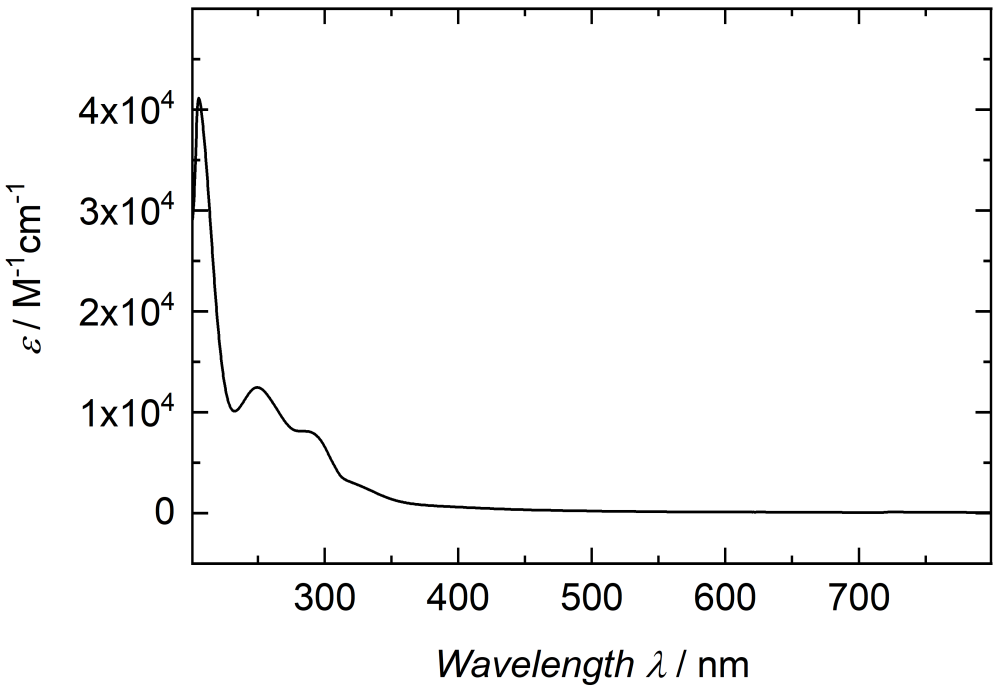

Figure S35: UV/Vis electronic absorption spectrum of **4**, recorded in a 0.1 mM THF solution.

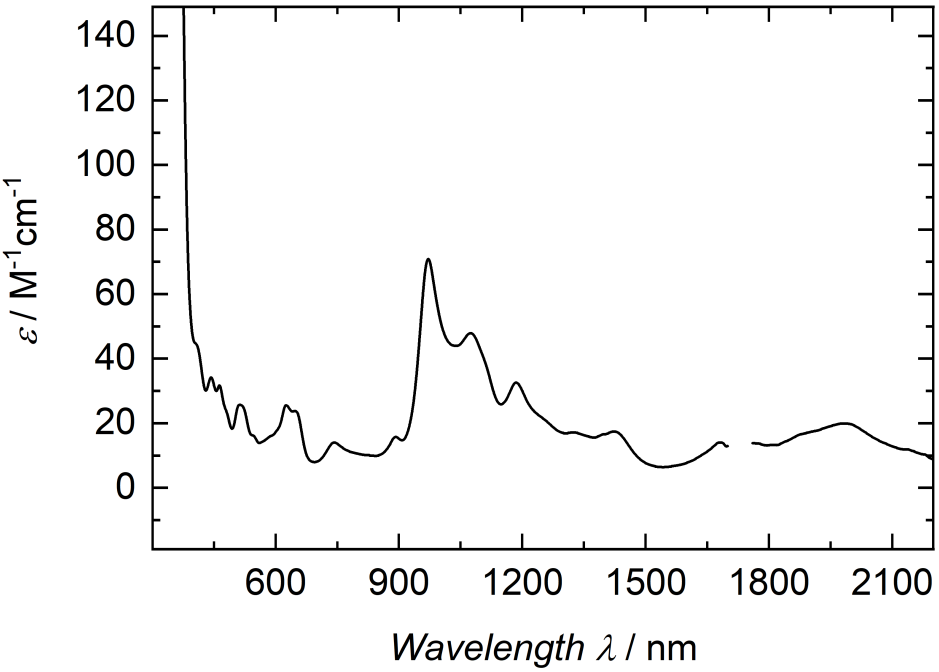

Figure S36: Vis/NIR electronic absorption spectrum of **4**, recorded in a 10 mM THF solution. Data points from 1700 nm to 1760 nm are omitted due to a detector change from a PbS to an In/Ga/As detector.

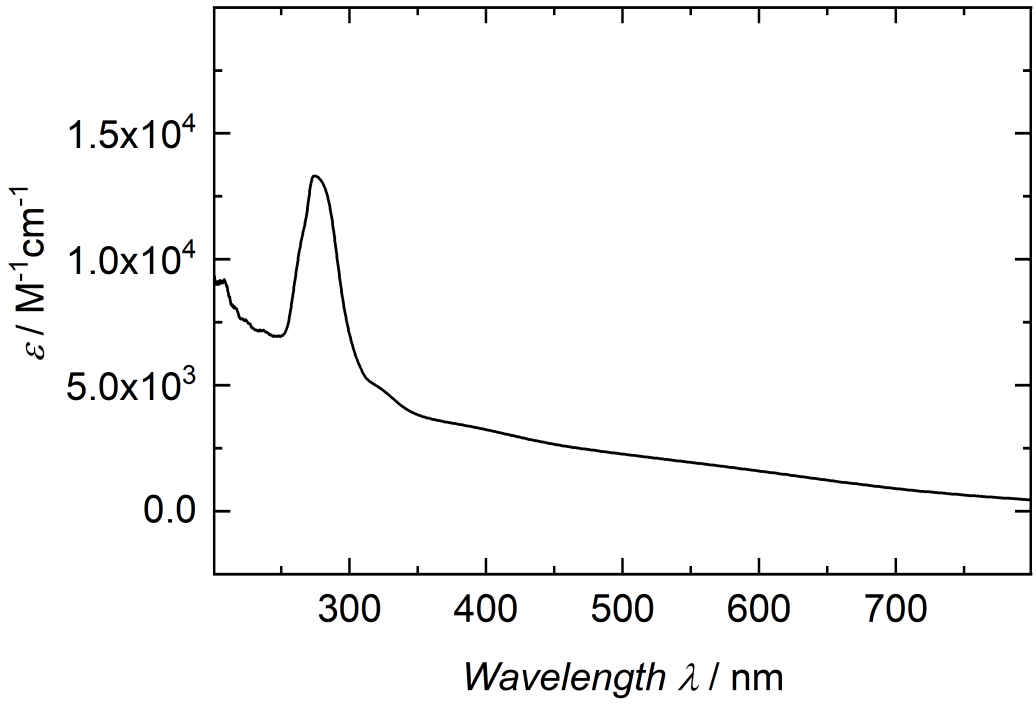

Figure S37: UV/Vis electronic absorption spectrum of **5**, recorded in a 0.1 mM benzene solution.

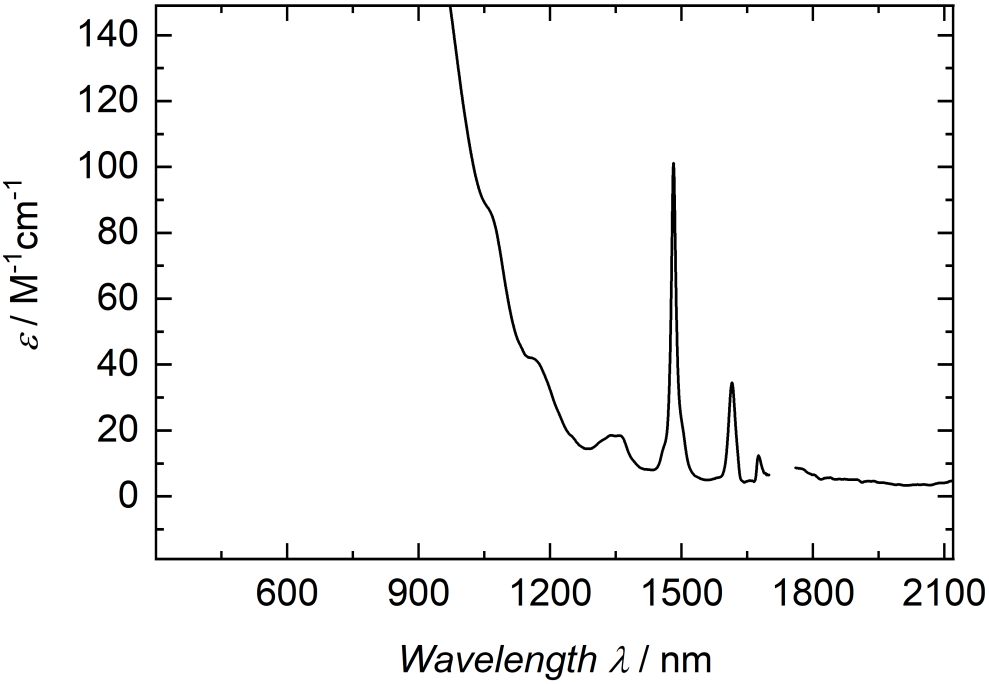

Figure S38: Vis/NIR electronic absorption spectrum of **5**, recorded in a 10 mM benzene solution. Data points from 1700 nm to 1760 nm are omitted due to a detector change from a PbS to an In/Ga/As detector.

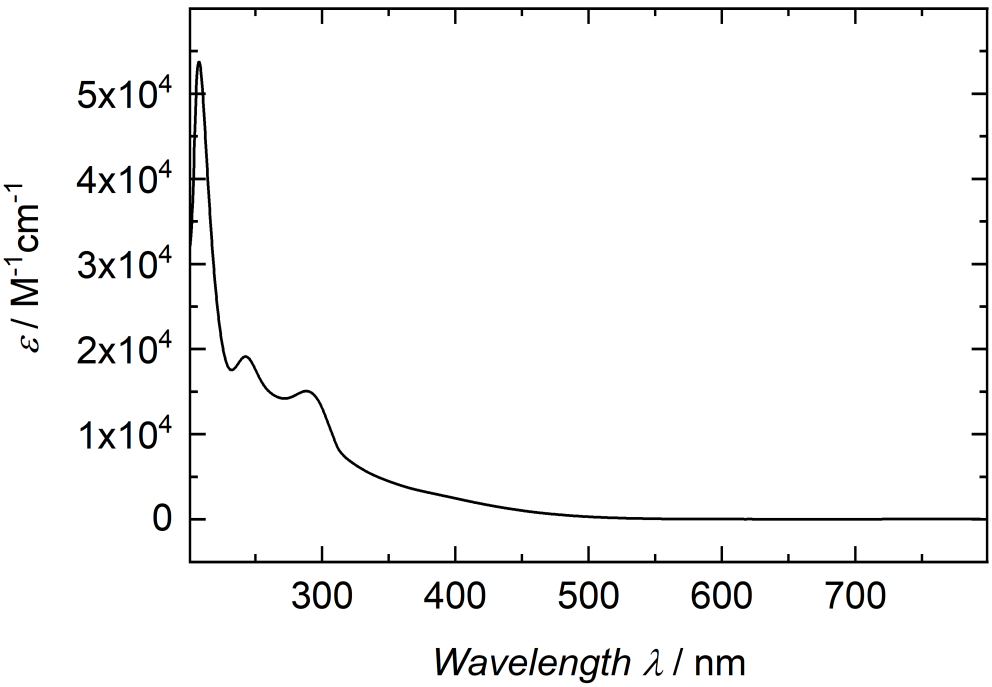

Figure S39: UV/Vis electronic absorption spectrum of **6**, recorded in a 0.07 mM THF solution.

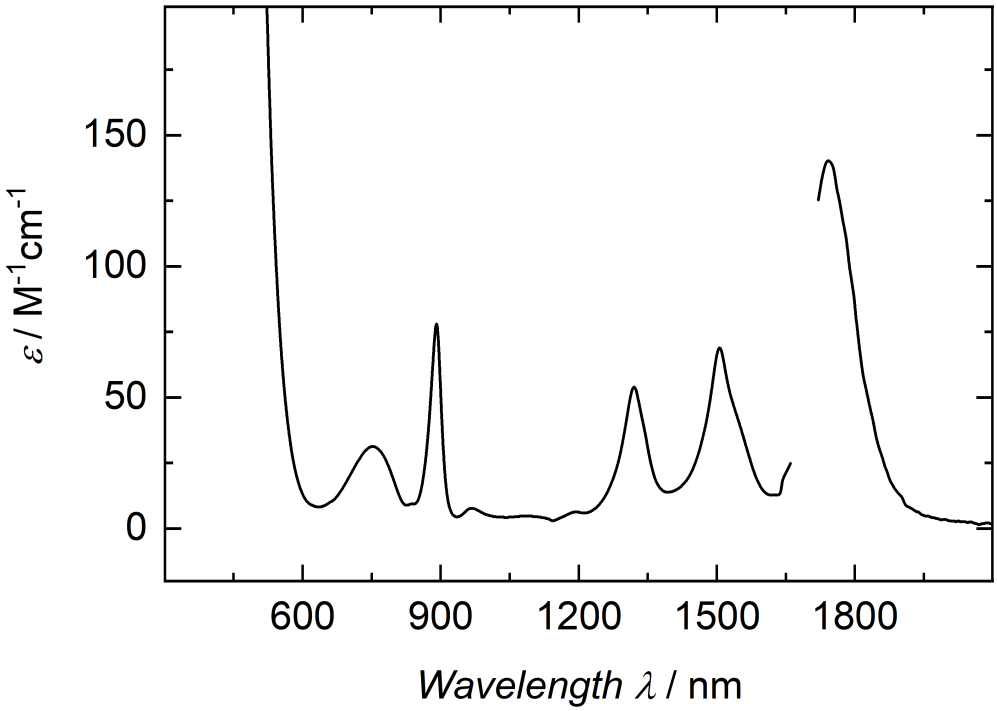

Figure S40: Vis/NIR electronic absorption spectrum of **6**, recorded in a 7 mM benzene solution. Data points from 1660 nm to 1720 nm are omitted due to a detector change from a PbS to an In/Ga/As detector.

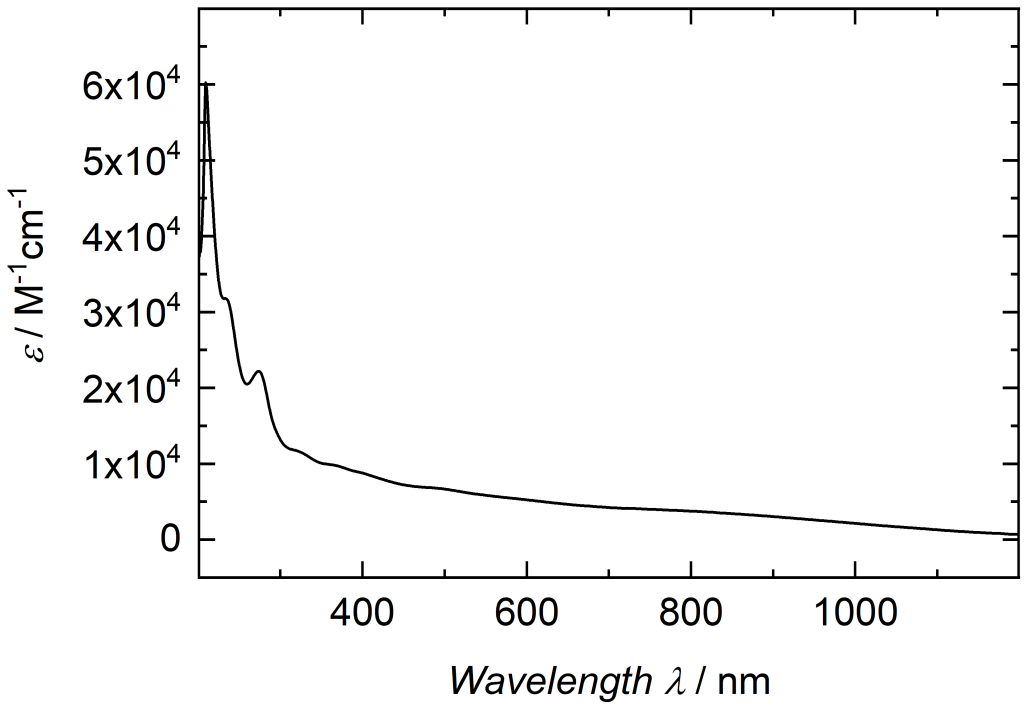

Figure S41: UV/Vis/NIR electronic absorption spectrum of **7**, recorded in a 0.06 mM THF solution.

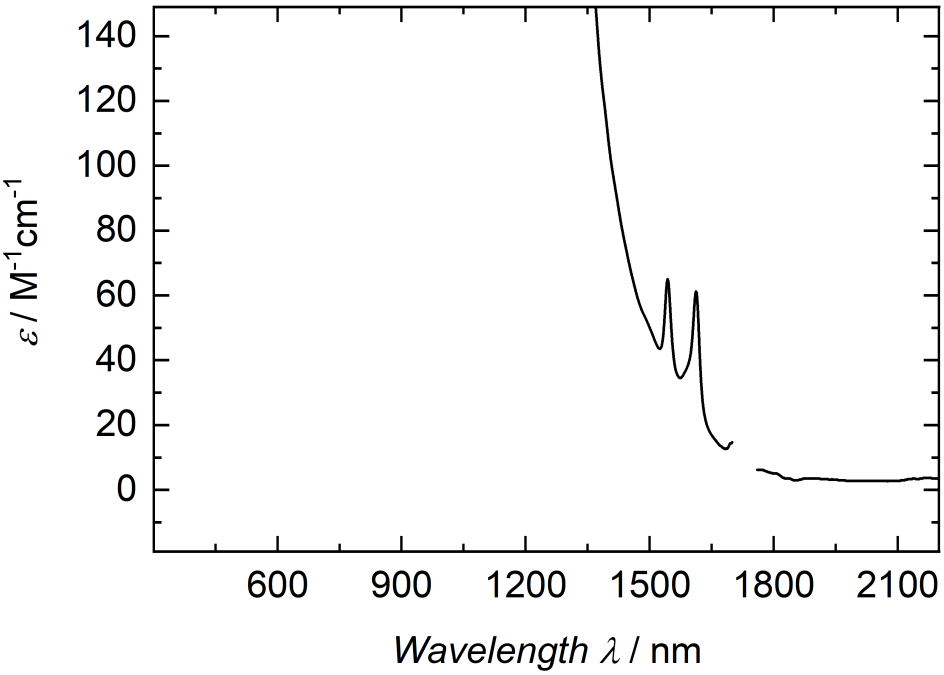

Figure S42: Vis/NIR electronic absorption spectrum of **7**, recorded in a 5.7 mM THF solution. Data points from 1700 nm to 1760 nm are omitted due to a detector change from a PbS to an In/Ga/As detector.

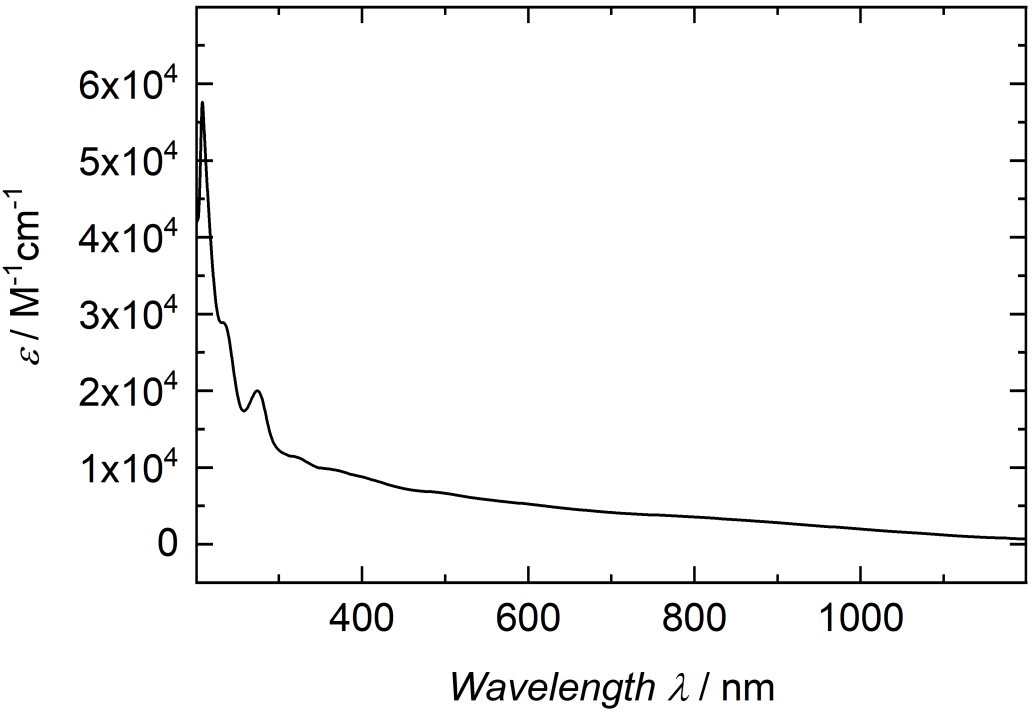

Figure S43: UV/Vis/NIR electronic absorption spectrum of **8**, recorded in a 0.025 mM THF solution.

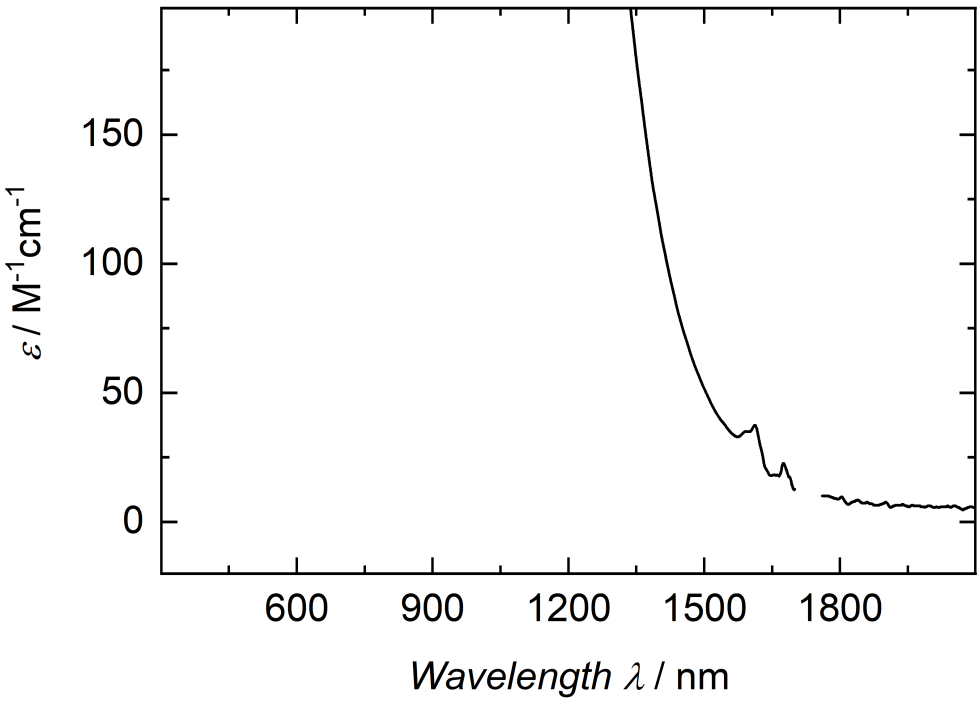

Figure S44: Vis/NIR electronic absorption spectrum of **8**, recorded in a 3.4 mM benzene solution. Data points from 1700 nm to 1760 nm are omitted due to a detector change from a PbS to an In/Ga/As detector.

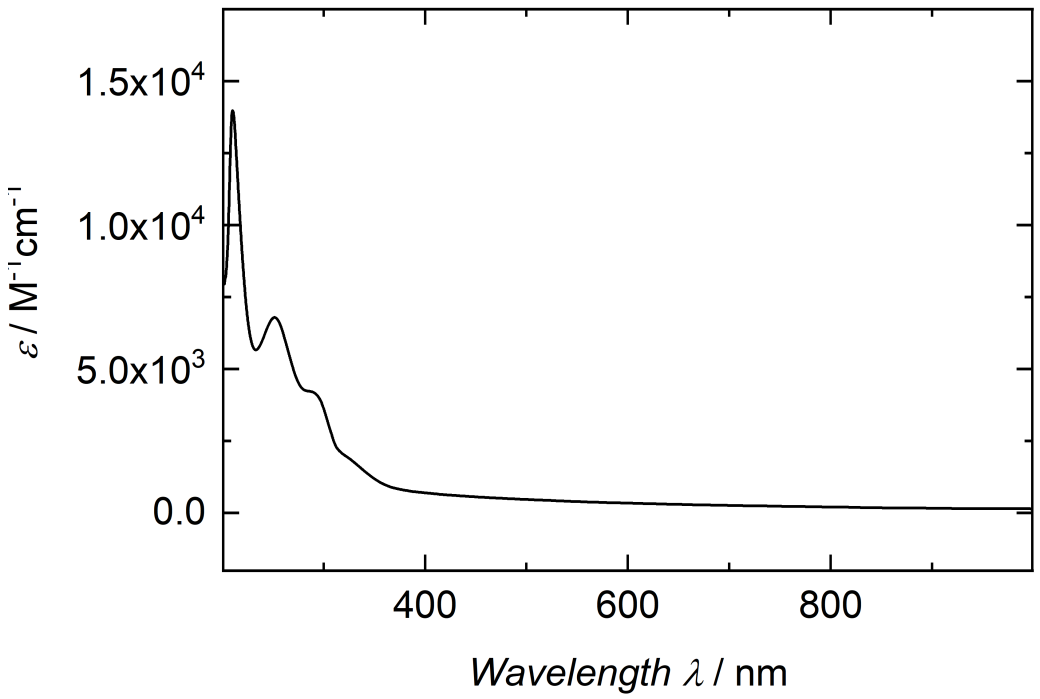

Figure S45: UV/Vis/NIR electronic absorption spectrum of **9**, recorded in a 0.12 mM benzene solution.

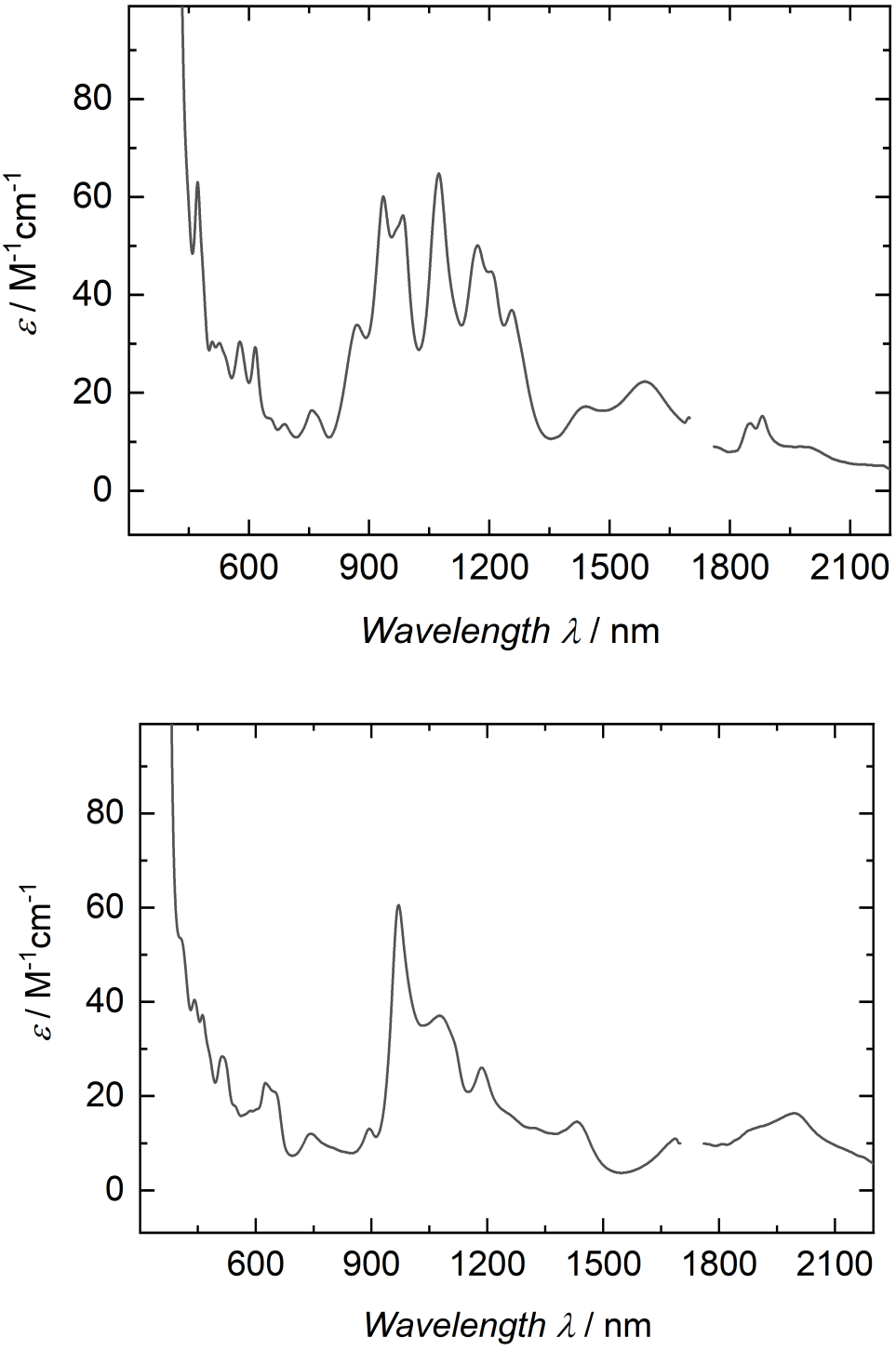

Figure S46: Vis/NIR electronic absorption spectrum of **9**, recorded in an 11 mM benzene (top) and a 9 mM THF (bottom) solution. Data points from 1700 nm to 1760 nm are omitted due to a detector change from a PbS to an In/Ga/As detector.

VT SQUID Magnetization

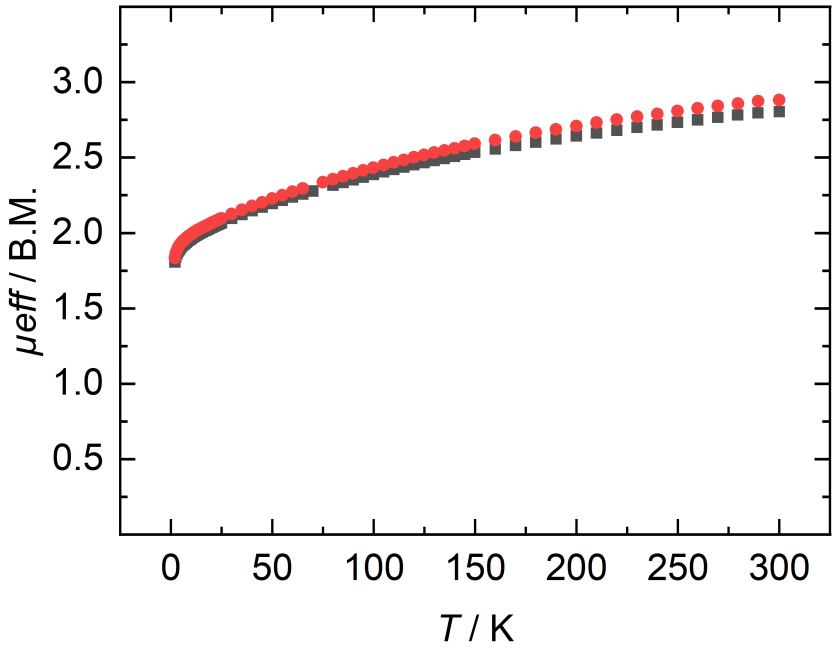

Figure S47: Temperature-dependent SQUID magnetization measurements of two independently synthesized samples of **1**; temperature dependency of μ_{eff} with an applied DC field of 1 T.

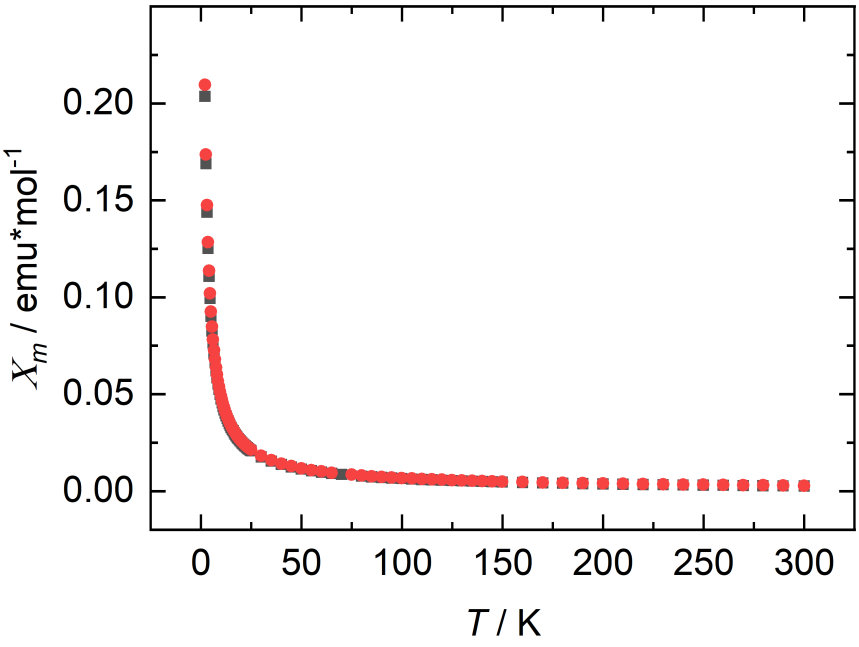

Figure S48: Temperature-dependent SQUID magnetization measurements of two independently synthesized samples of **1**; temperature dependency of X_m with an applied DC field of 1 T.

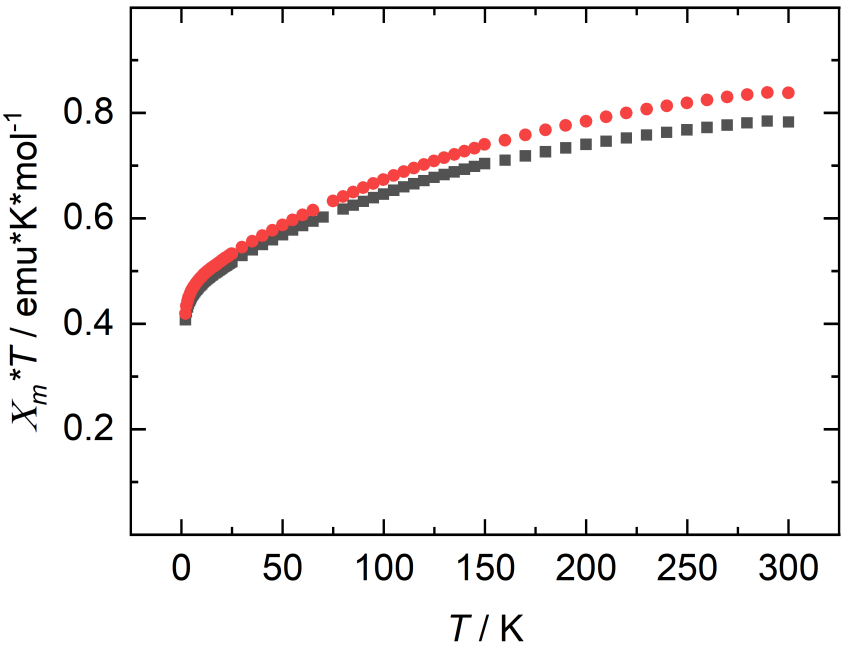

Figure S49: Temperature-dependent SQUID magnetization measurements of two independently synthesized samples of **1**; temperature dependency of X_mT with an applied DC field of 1 T.

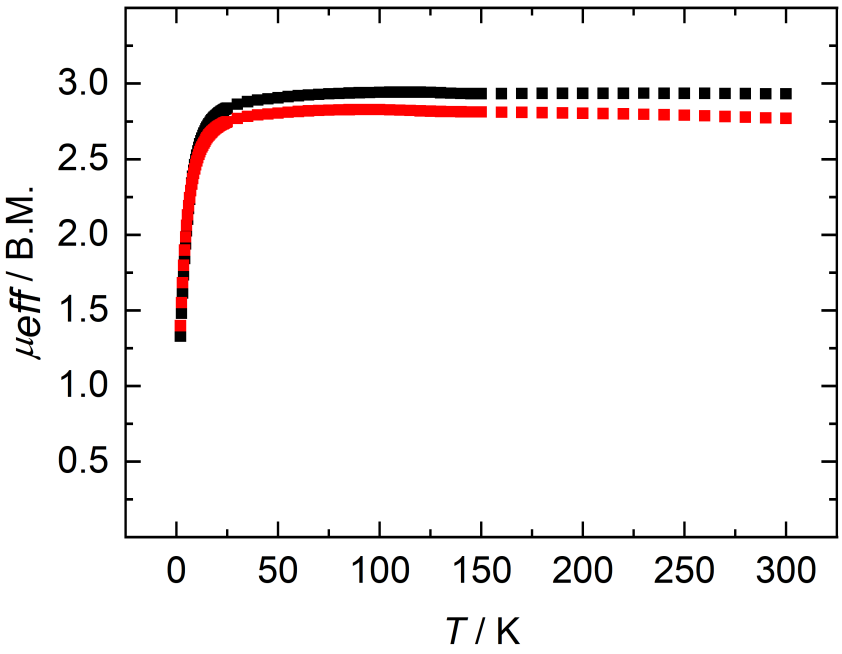

Figure S50: Temperature-dependent SQUID magnetization measurements of two independently synthesized samples of **2**; temperature dependency of μ_{eff} with an applied DC field of 1 T.

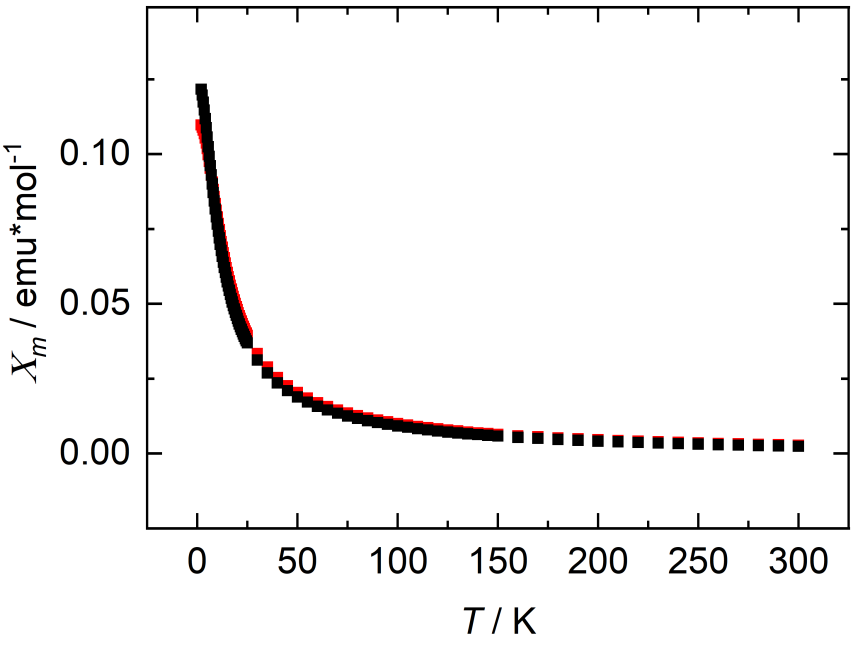

Figure S51: Temperature-dependent SQUID magnetization measurements of two independently synthesized samples of **2**; temperature dependency of X_m with an applied DC field of 1 T.

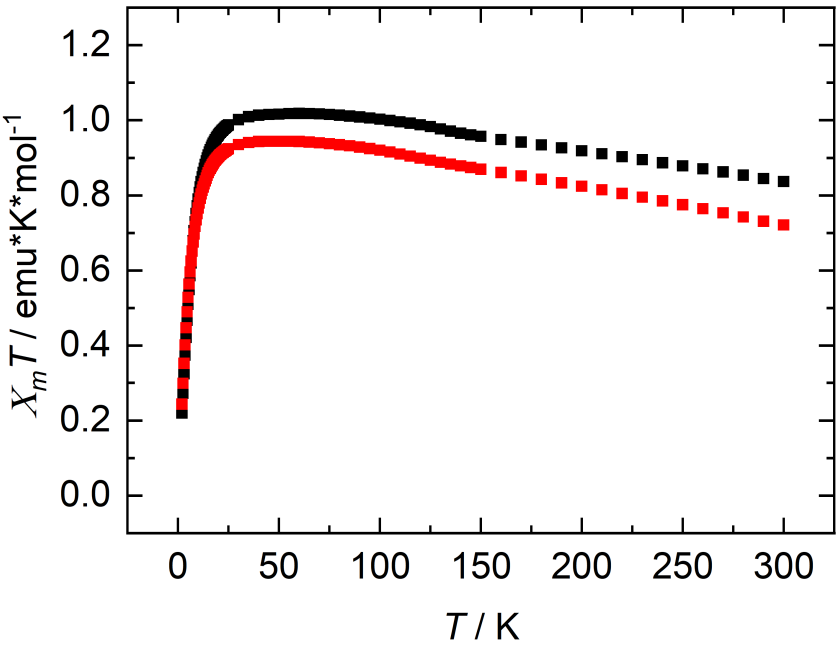

Figure S52: Temperature-dependent SQUID magnetization measurements of two independently synthesized samples of **2**; temperature dependency of X_mT with an applied DC field of 1 T.

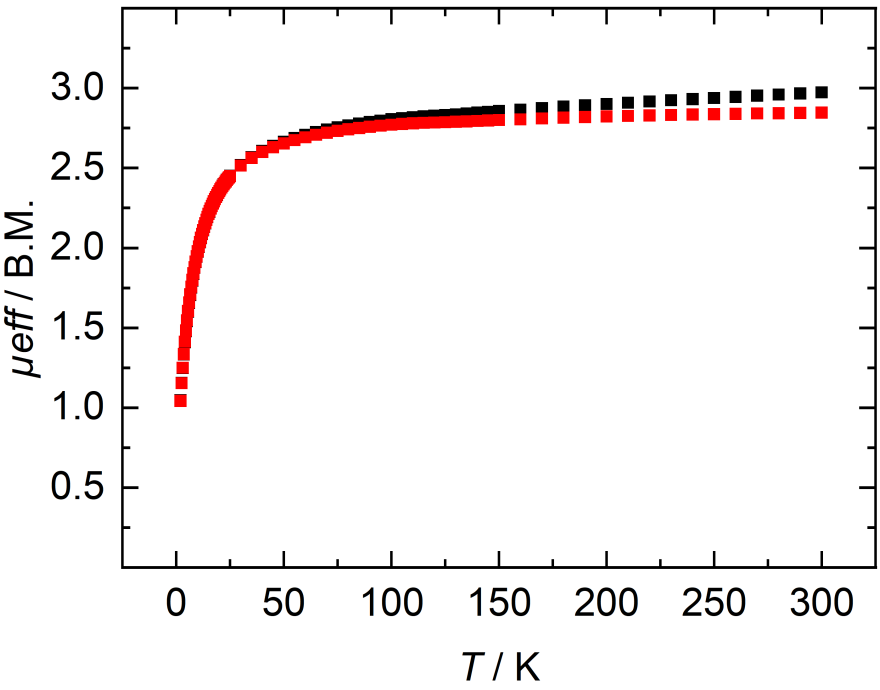

Figure S53: Temperature-dependent SQUID magnetization measurements of two independently synthesized samples of **3**; temperature dependency of μ_{eff} with an applied DC field of 1 T.

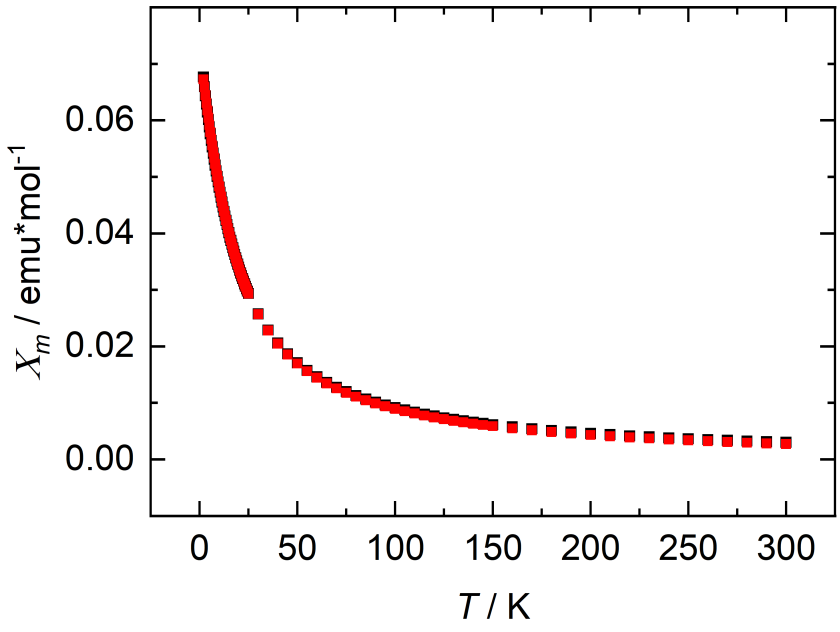

Figure S54: Temperature-dependent SQUID magnetization measurements of two independently synthesized samples of **3**; temperature dependency of X_m with an applied DC field of 1 T.

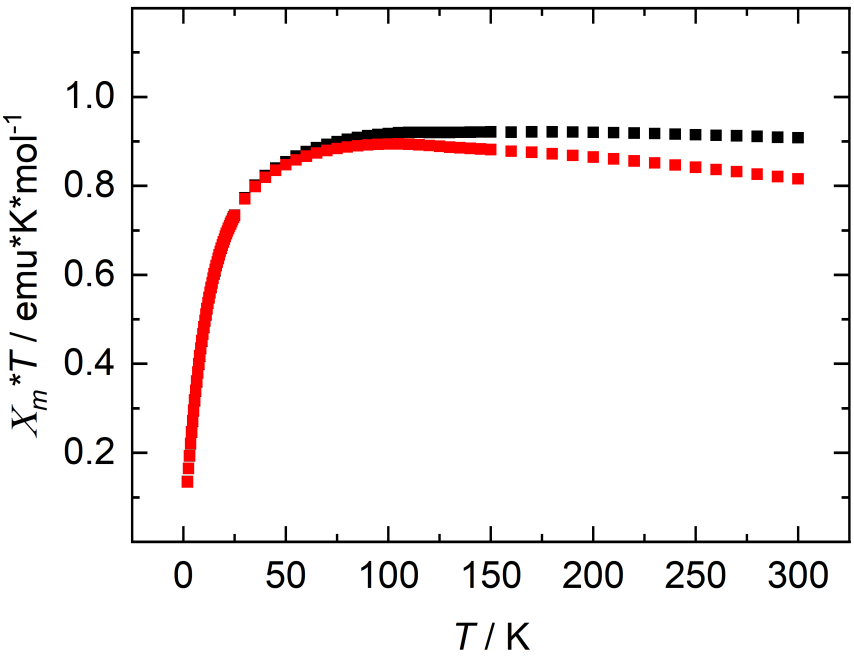

Figure S55: Temperature-dependent SQUID magnetization measurements of two independently synthesized samples of **3**; temperature dependency of X_mT with an applied DC field of 1 T.

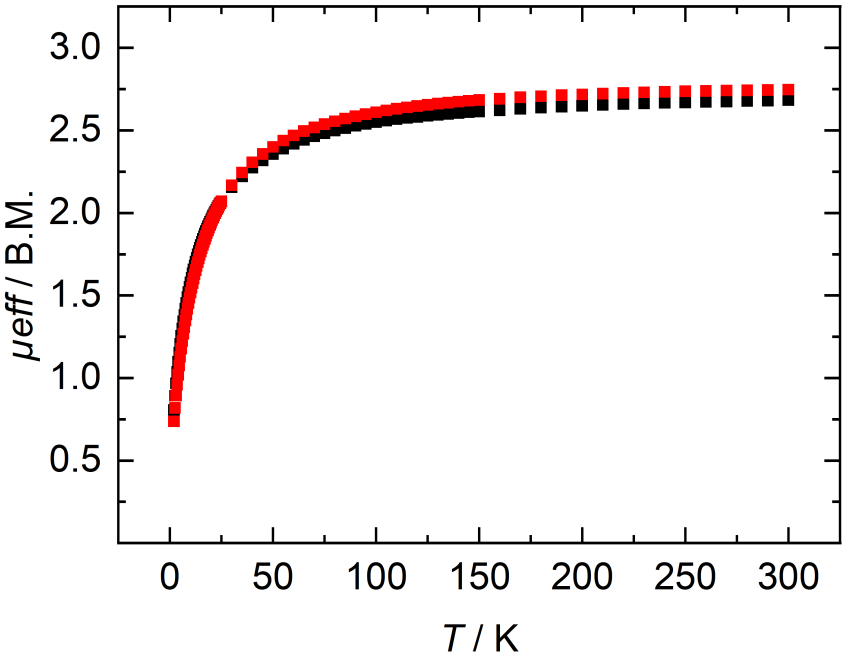

Figure S56: Temperature-dependent SQUID magnetization measurements of two independently synthesized samples of **4**; temperature dependency of μ_{eff} with an applied DC field of 1 T.

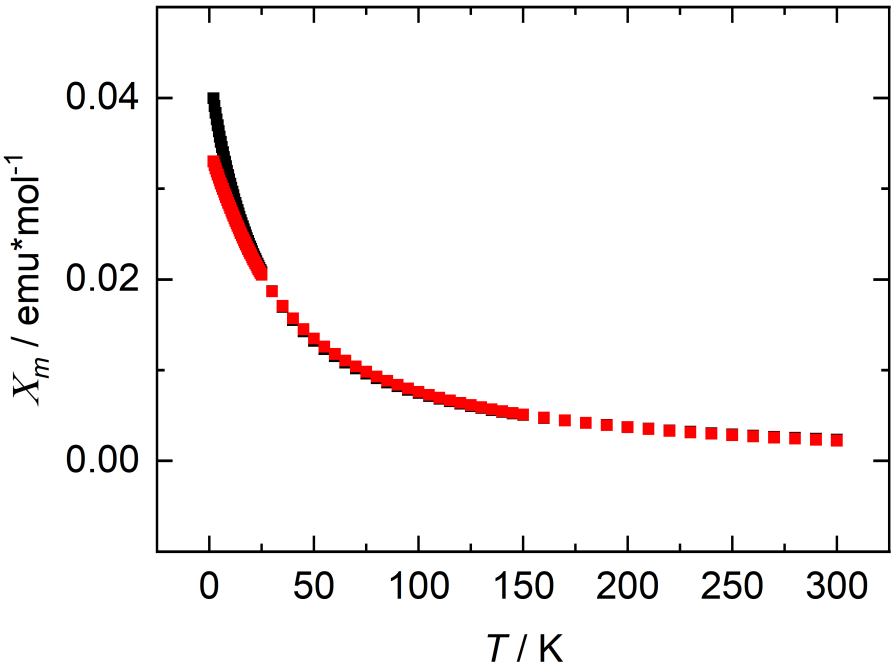

Figure S57: Temperature-dependent SQUID magnetization measurements of two independently synthesized samples of **4**; temperature dependency of X_m with an applied DC field of 1 T.

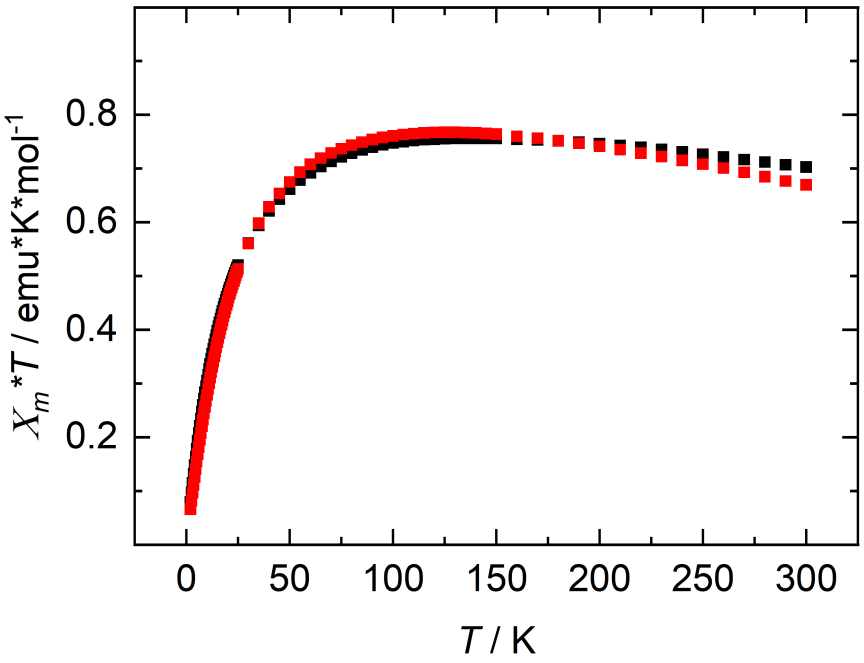

Figure S58: Temperature-dependent SQUID magnetization measurements of two independently synthesized samples of **4**; temperature dependency of X_mT with an applied DC field of 1 T.

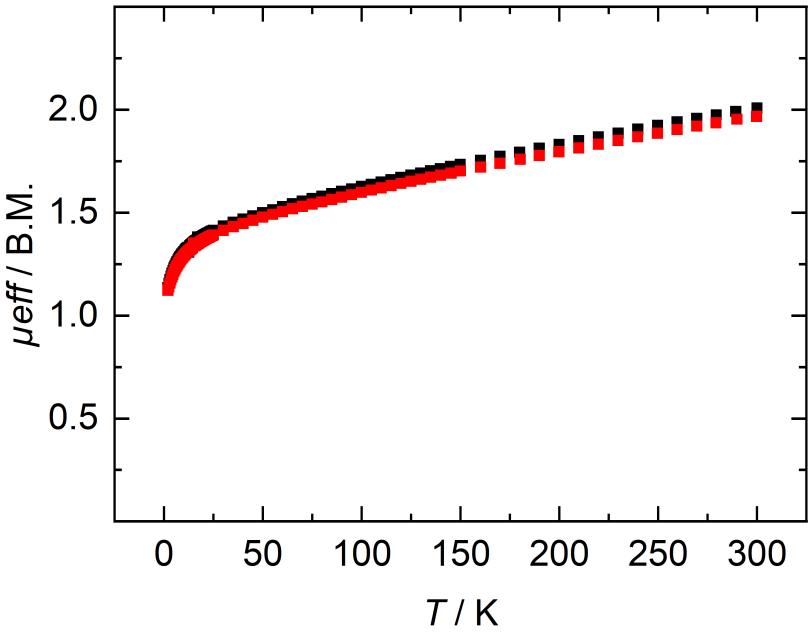

Figure S59: Temperature-dependent SQUID magnetization measurements of two independently synthesized samples of **5**; temperature dependency of μ_{eff} with an applied DC field of 1 T.

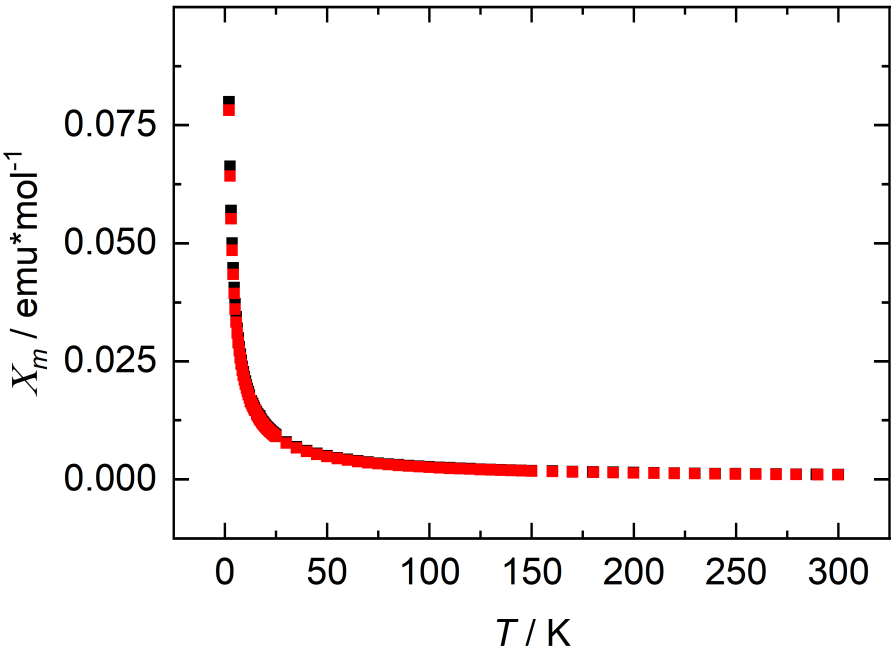

Figure S60: Temperature-dependent SQUID magnetization measurements of two independently synthesized samples of **5**; temperature dependency of X_m with an applied DC field of 1 T.

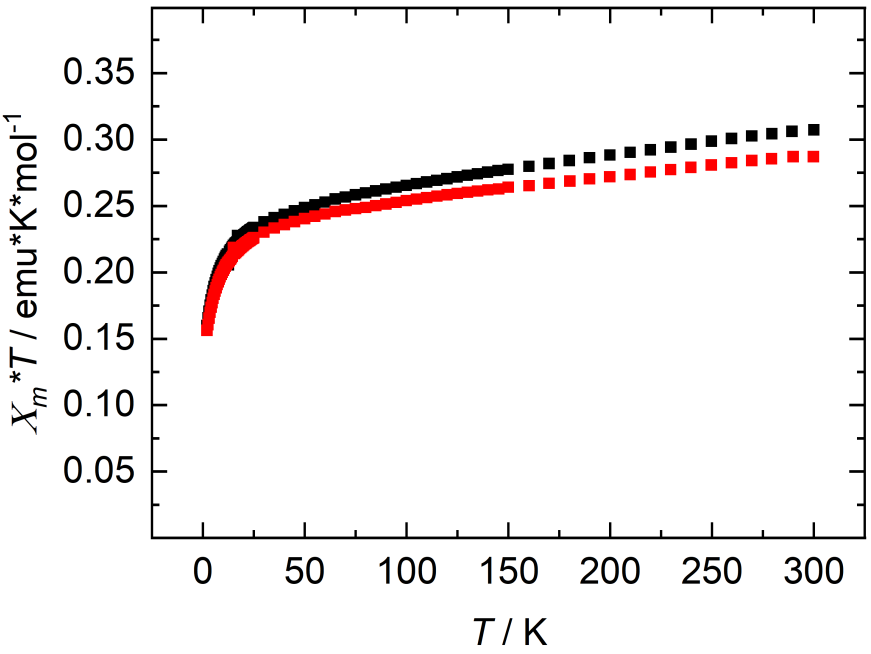

Figure S61: Temperature-dependent SQUID magnetization measurements of two independently synthesized samples of **5**; temperature dependency of X_mT with an applied DC field of 1 T.

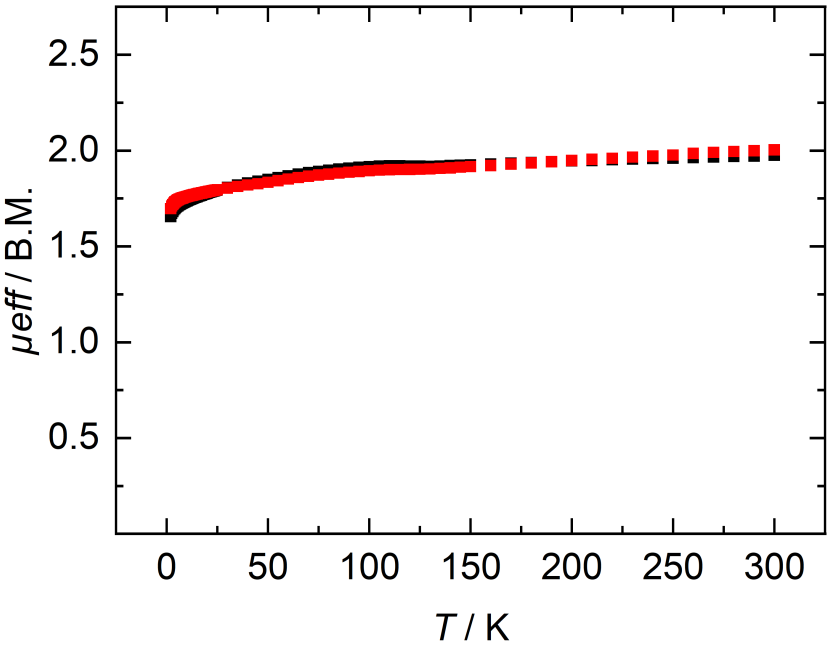

Figure S62: Temperature-dependent SQUID magnetization measurements of two independently synthesized samples of **6**; temperature dependency of μ_{eff} with an applied DC field of 1 T.

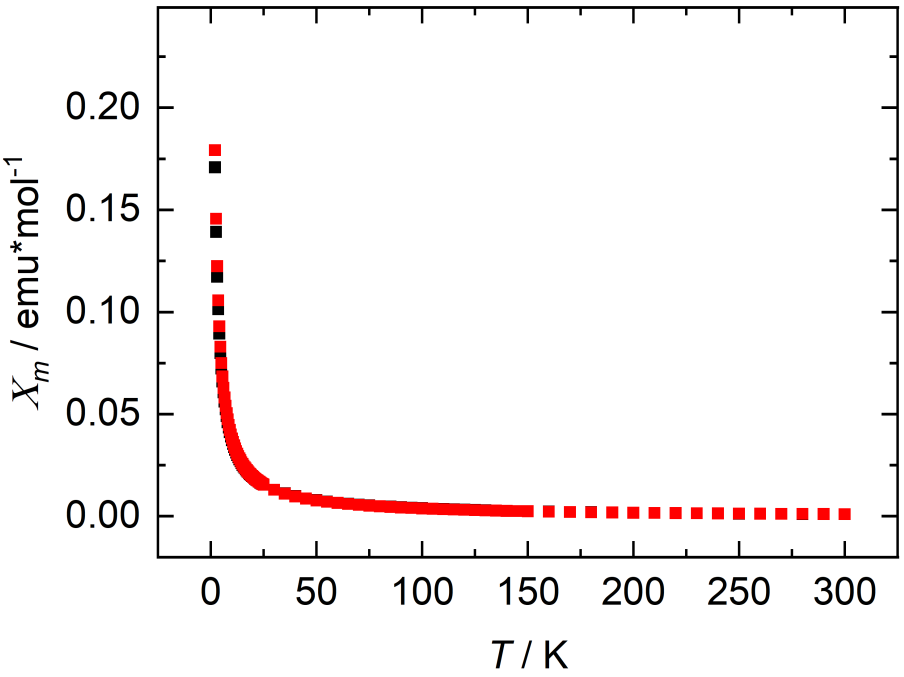

Figure S63: Temperature-dependent SQUID magnetization measurements of two independently synthesized samples of **6**; temperature dependency of X_m with an applied DC field of 1 T.

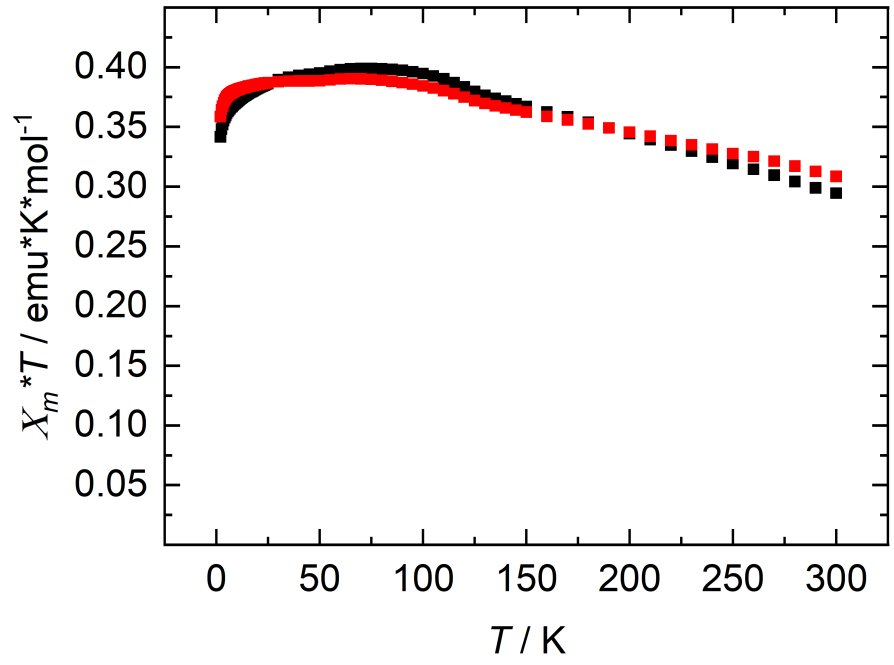

Figure S64: Temperature-dependent SQUID magnetization measurements of two independently synthesized samples of **6**; temperature dependency of X_mT with an applied DC field of 1 T.

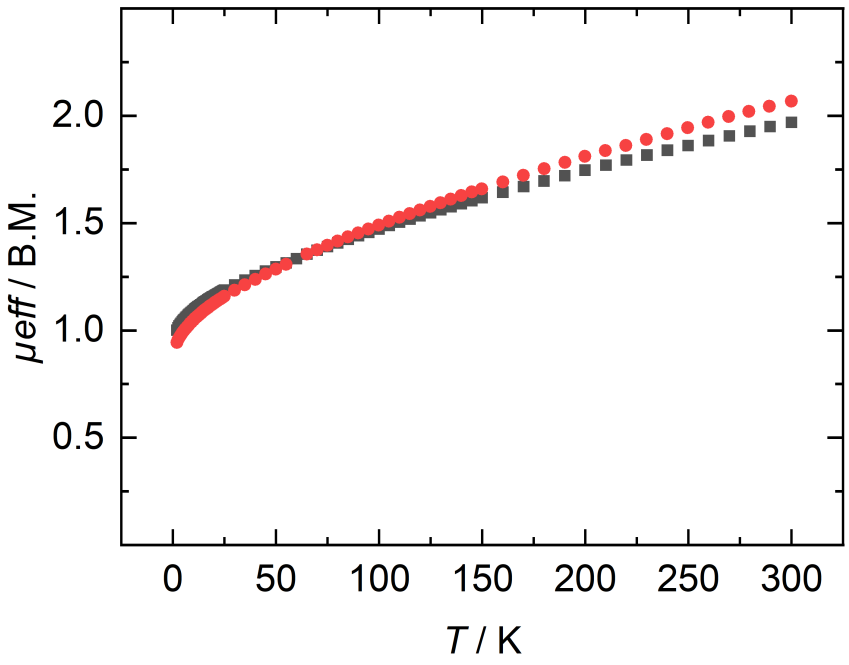

Figure S65: Temperature-dependent SQUID magnetization measurements of two independently synthesized samples of **7**; temperature dependency of μ_{eff} with an applied DC field of 1 T.

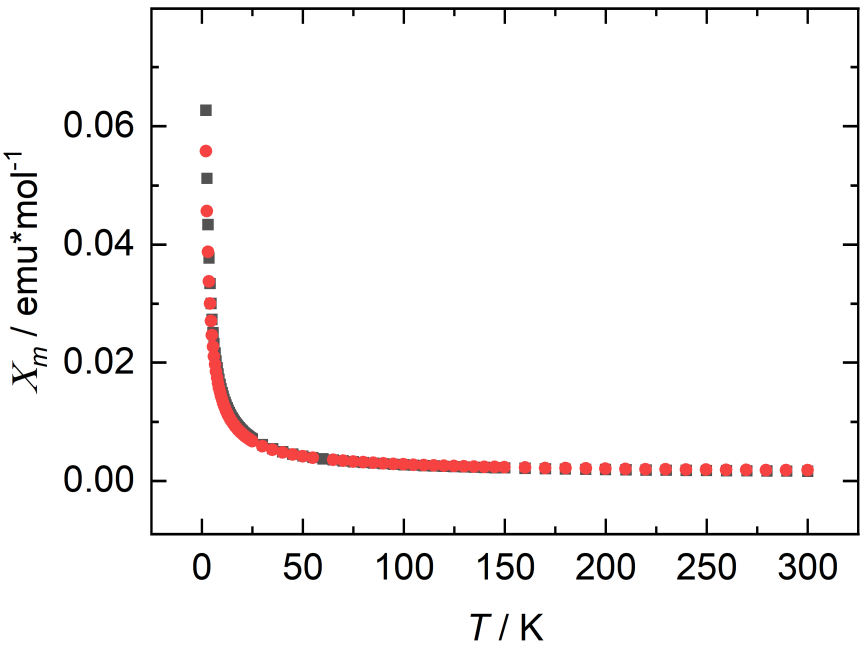

Figure S66: Temperature-dependent SQUID magnetization measurements of two independently synthesized samples of **7**; temperature dependency of X_m with an applied DC field of 1 T.

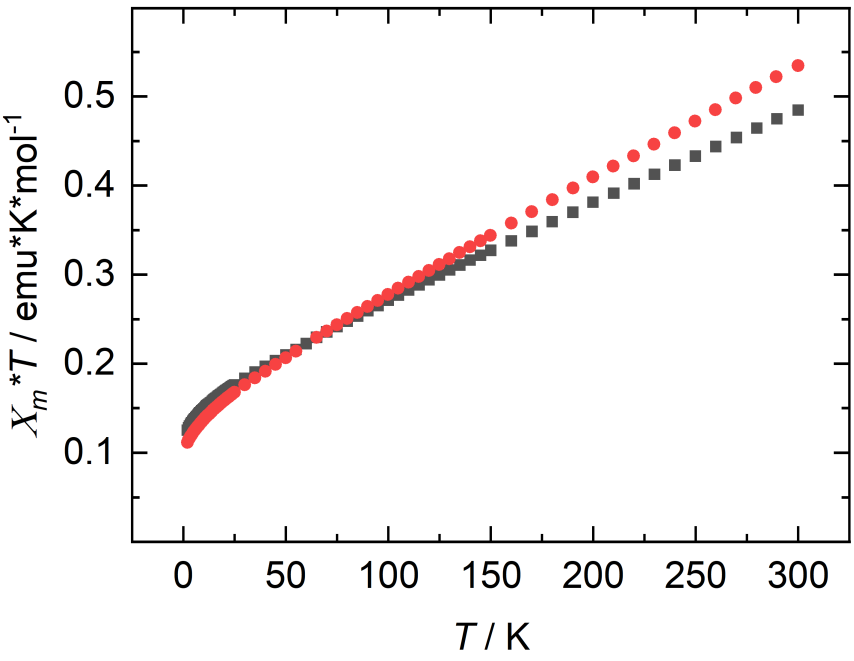

Figure S67: Temperature-dependent SQUID magnetization measurements of two independently synthesized samples of **7**; temperature dependency of X_mT with an applied DC field of 1 T.

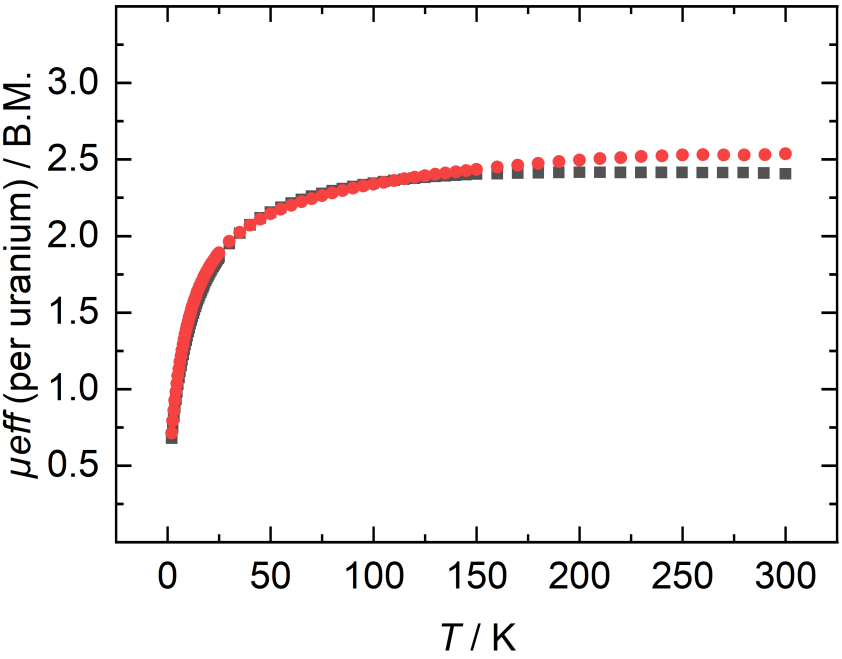

Figure S68: Temperature-dependent SQUID magnetization measurements of two independently synthesized samples of **9**; temperature dependency of μ_{eff} with an applied DC field of 1 T.

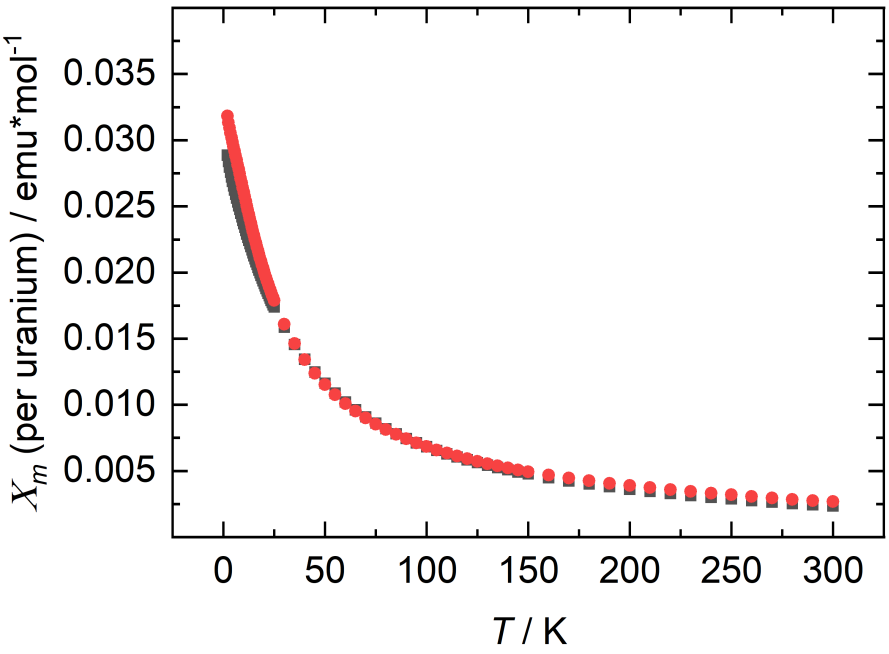

Figure S69: Temperature-dependent SQUID magnetization measurements of two independently synthesized samples of **9**; temperature dependency of X_m with an applied DC field of 1 T.

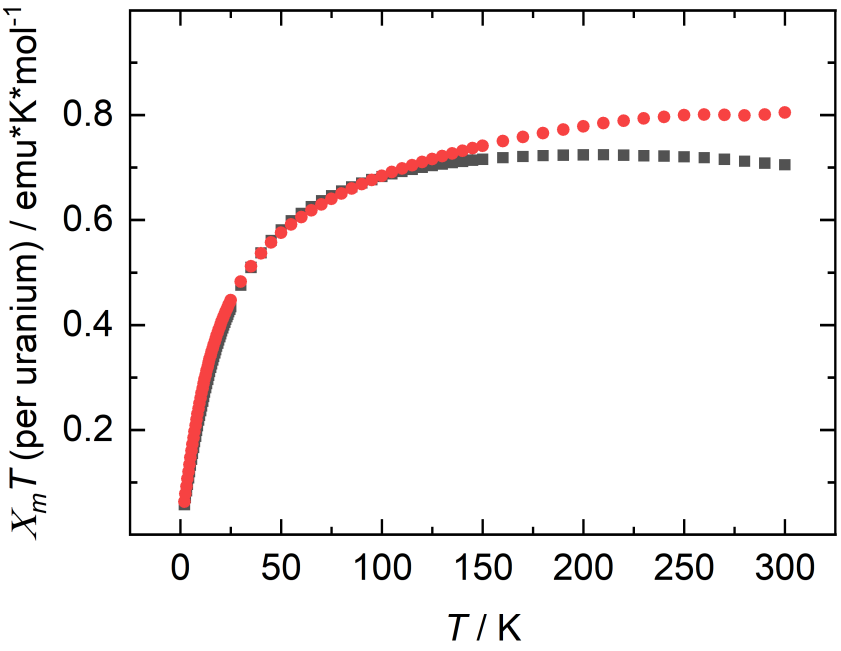

Figure S70: Temperature-dependent SQUID magnetization measurements of two independently synthesized samples of **9**; temperature dependency of X_mT with an applied DC field of 1 T.

Electrochemistry

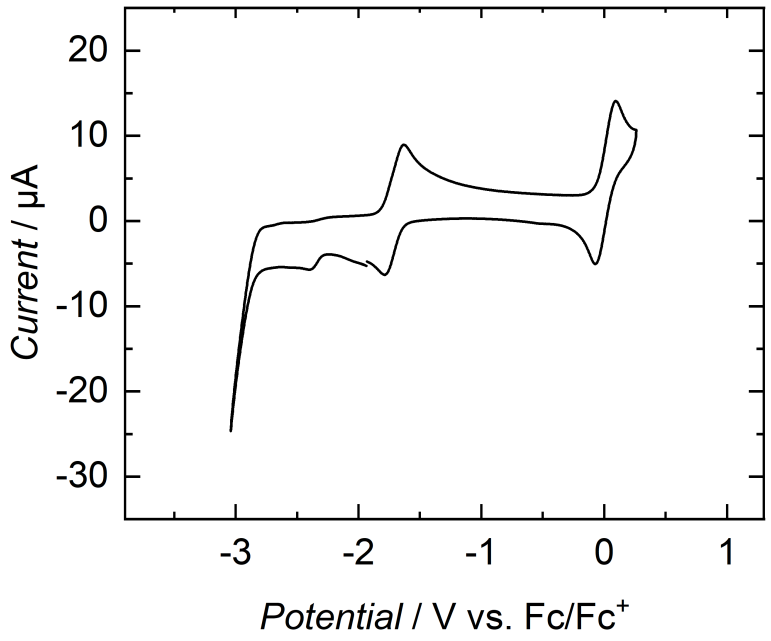

Figure S71: Cyclic voltammogram of **1** in 1 mM THF solution with $TBAPF_6$ (1 mM) as supporting electrolyte at 0.2 V s^{-1}.

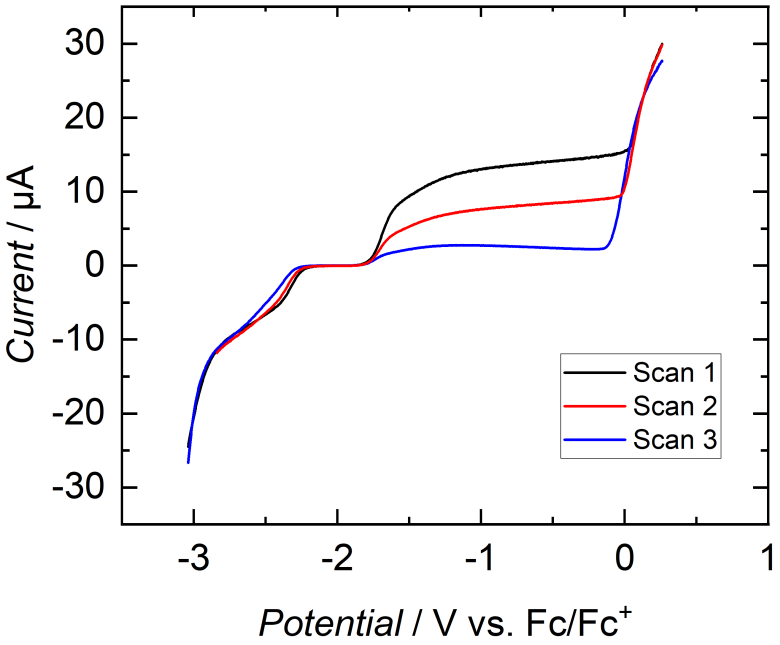

Figure S72: Linear sweep measurement of **1** in 1 mM THF solution with $TBAPF_6$ (1 mM) as supporting electrolyte at 50 mV s^{-1} and 2000 rpm. The three scans show the decomposition and bulk oxidation via electrolysis over time.

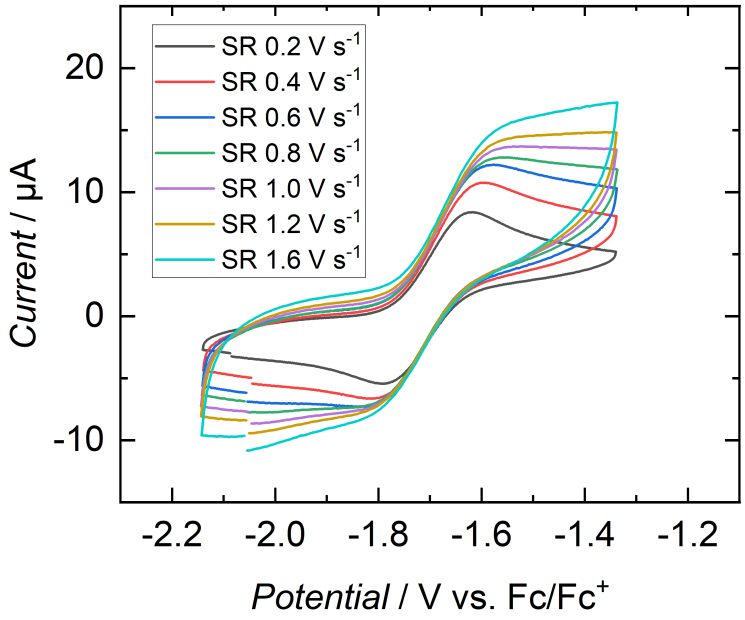

Figure S73: Cyclic voltammogram of the redox event at $E_{1/2}$ = –1.71 V *vs* Fc/Fc^+ of **1** in 1 mM THF solution with $TBAPF_6$ (1 mM) as supporting electrolyte at various scan rates (SR).

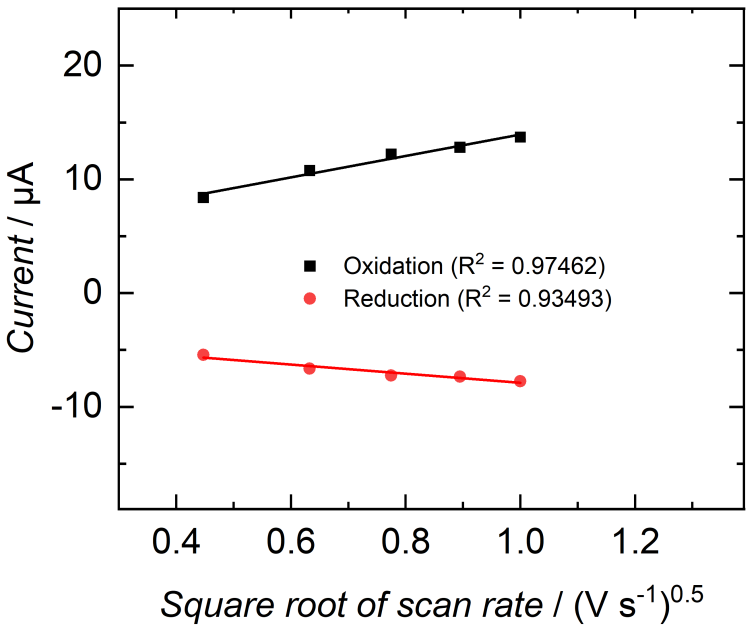

Figure S74: Randles-Sevcik-Plot of the positive and negative peak currents of the redox event at $E_{1/2}$ = –1.71 V *vs* Fc/Fc^+ of **1** (Figure S73).

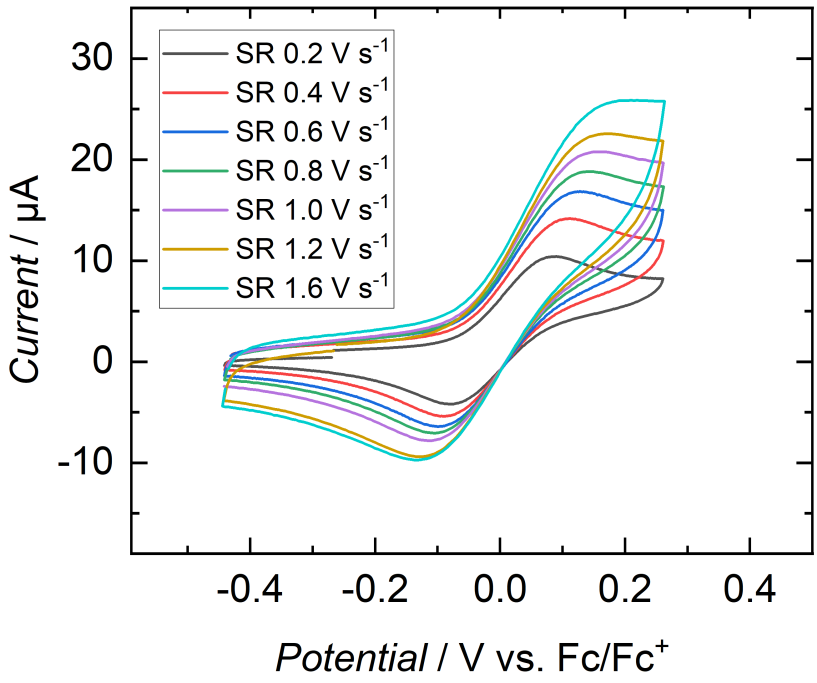

Figure S75: Cyclic voltammogram of the redox event at $E_{1/2}$ = 0.00 V *vs* Fc/Fc^+ of **1** in 1 mM THF solution with $TBAPF_6$ (1 mM) as supporting electrolyte at various scan rates (SR).

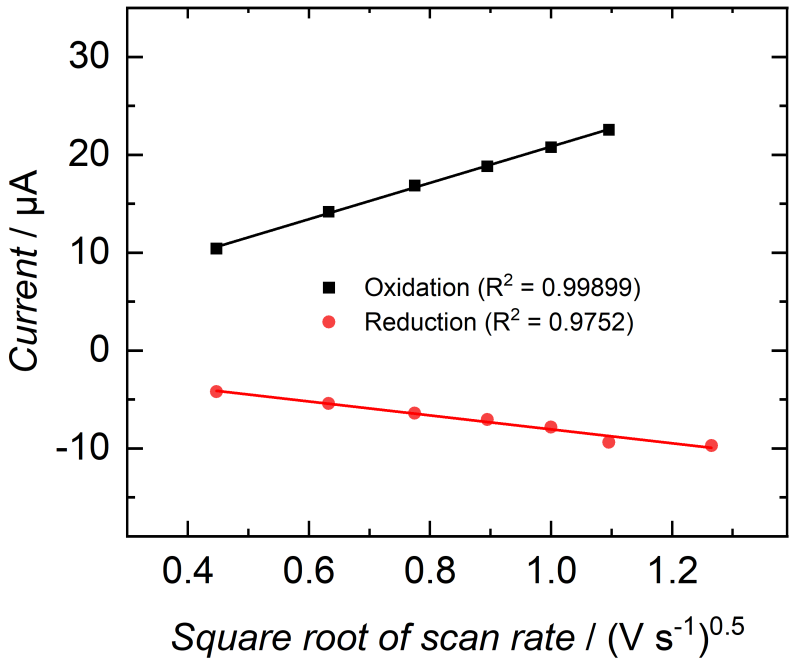

Figure S76: Randles-Sevcik-Plot of the positive and negative peak currents of the redox event at $E_{1/2}$ = 0.00 V *vs* Fc/Fc^+ of **1** (Figure S75).

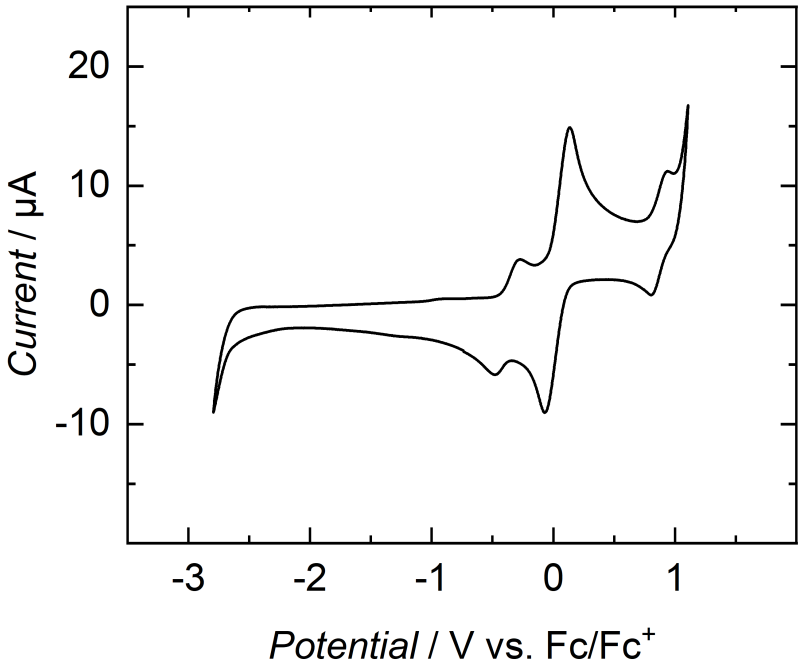

Figure S77: Cyclic voltammogram of **2** in 1 mM THF solution with $TBAPF_6$ (1 mM) as supporting electrolyte at 0.2 V s^{-1}.

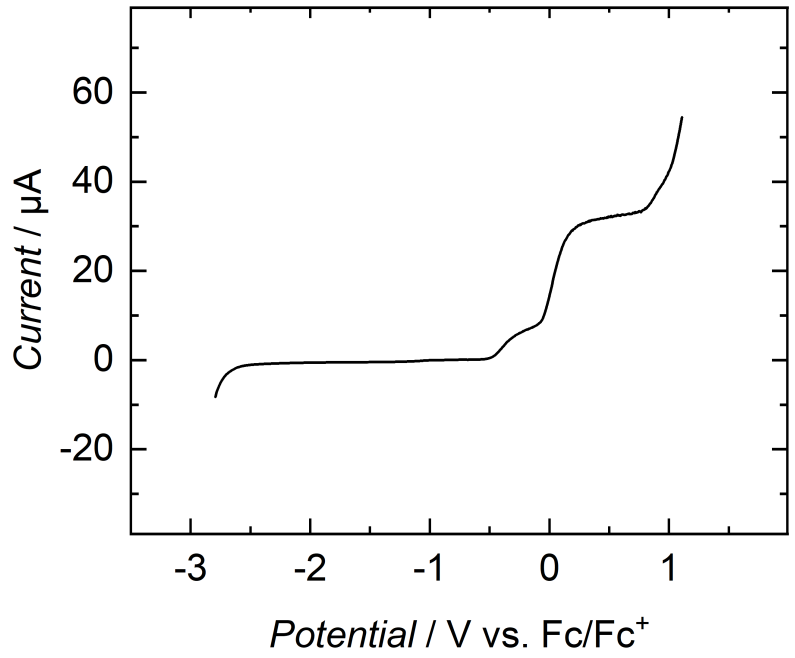

Figure S78: Linear sweep measurement of **2** in 1 mM THF solution with $TBAPF_6$ (1 mM) as supporting electrolyte at 50 mV s^{-1} and 2000 rpm.

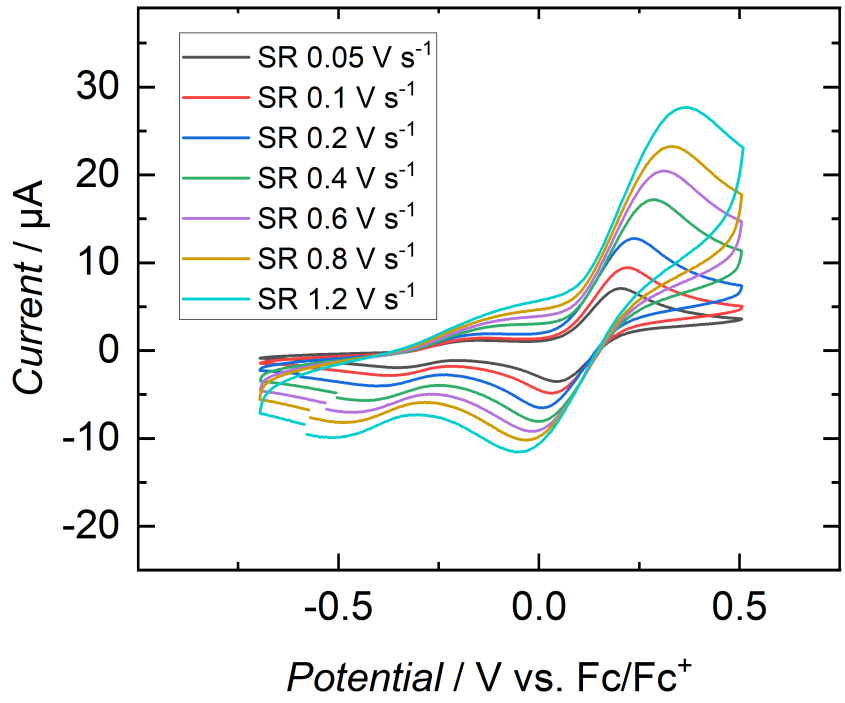

Figure S79: Cyclic voltammogram of the redox event at $E_{1/2}$ = 0.12 V *vs* Fc/Fc^+ of **2** in 1 mM THF solution with $TBAPF_6$ (1 mM) as supporting electrolyte at various scan rates (SR).

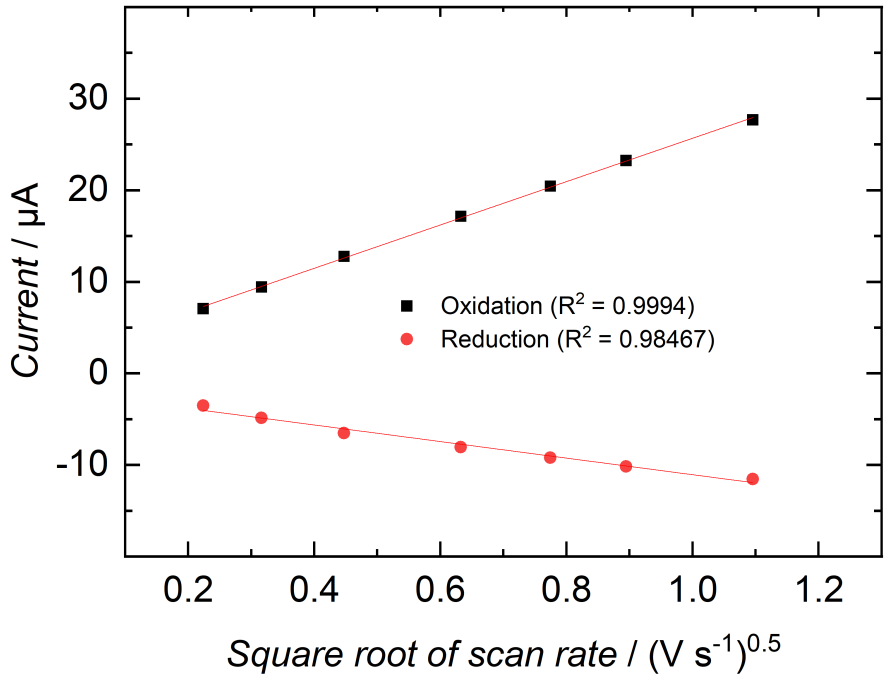

Figure S80: Randles-Sevcik-Plot of the positive and negative peak currents of the redox event at $E_{1/2}$ = 0.12 V *vs* Fc/Fc^+ of **2** (Figure S79).

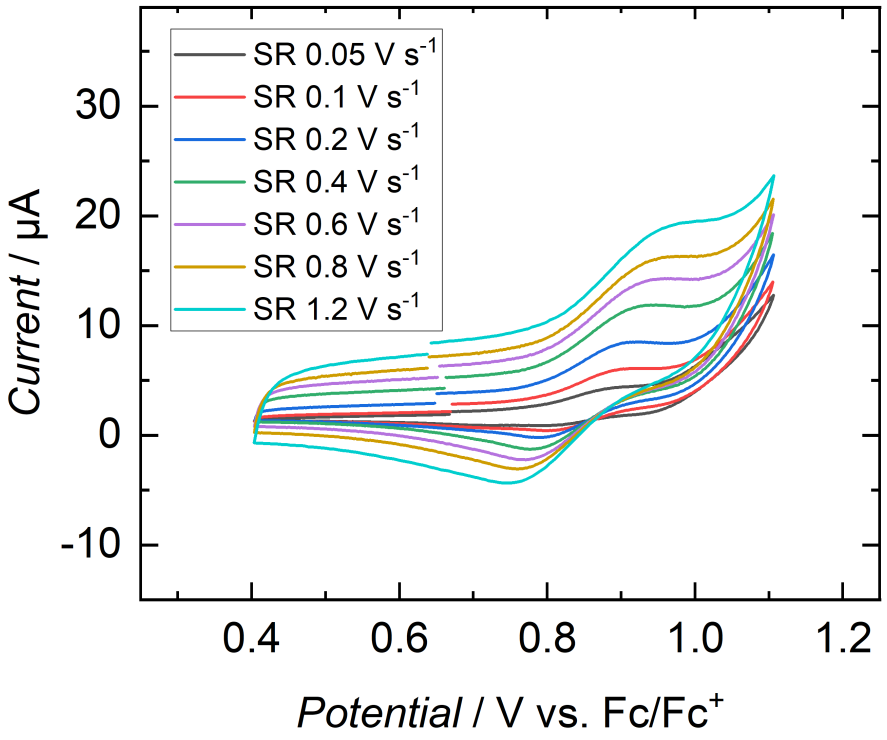

Figure S81: Cyclic voltammogram of the redox event at $E_{1/2}$ = 0.85 V *vs* Fc/Fc^+ of **2** in 1 mM THF solution with $TBAPF_6$ (1 mM) as supporting electrolyte at various scan rates (SR).

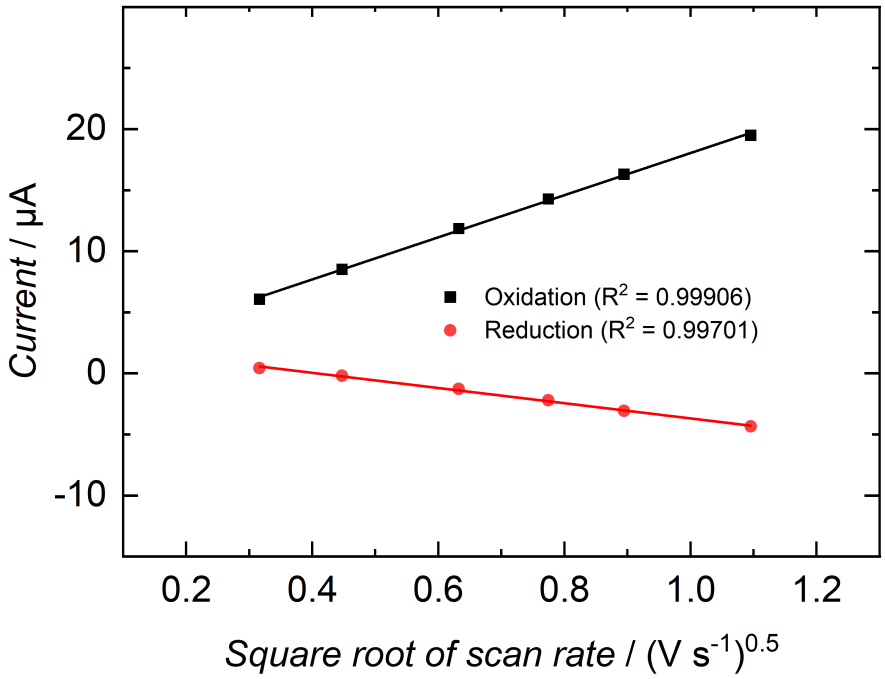

Figure S82: Randles-Sevcik-Plot of the positive and negative peak currents of the redox event at $E_{1/2}$ = 0.85 V *vs* Fc/Fc^+ of **2** (Figure S81).

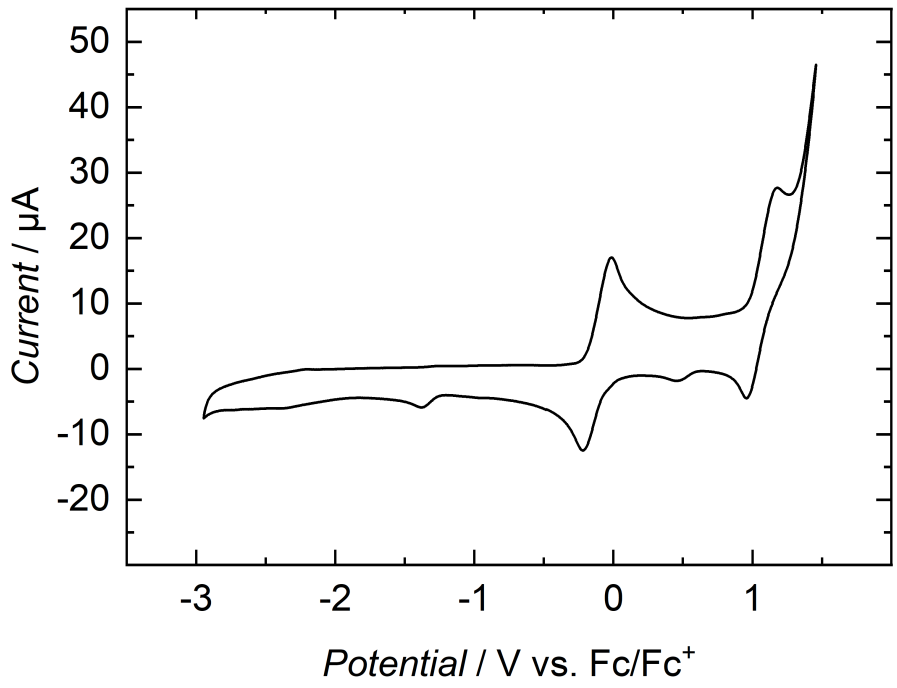

Figure S83: Cyclic voltammogram of **3** in 1 mM THF solution with $TBAPF_6$ (1 mM) as supporting electrolyte at 0.2 V s^{-1}.

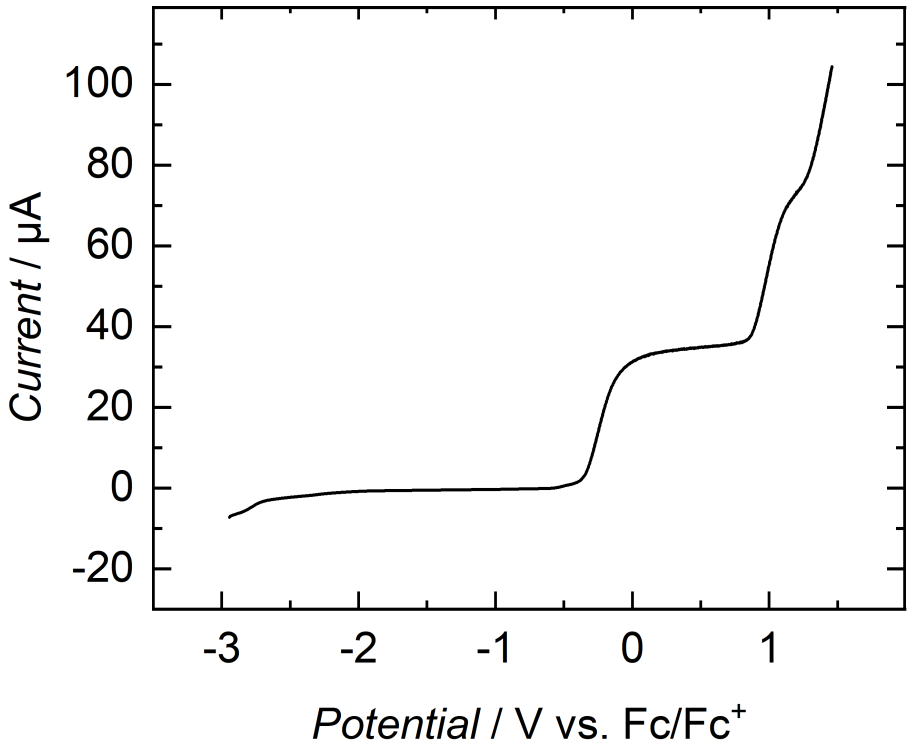

Figure S84: Linear sweep measurement of **3** in 1 mM THF solution with $TBAPF_6$ (1 mM) as supporting electrolyte at 50 mV s^{-1} and 2000 rpm.

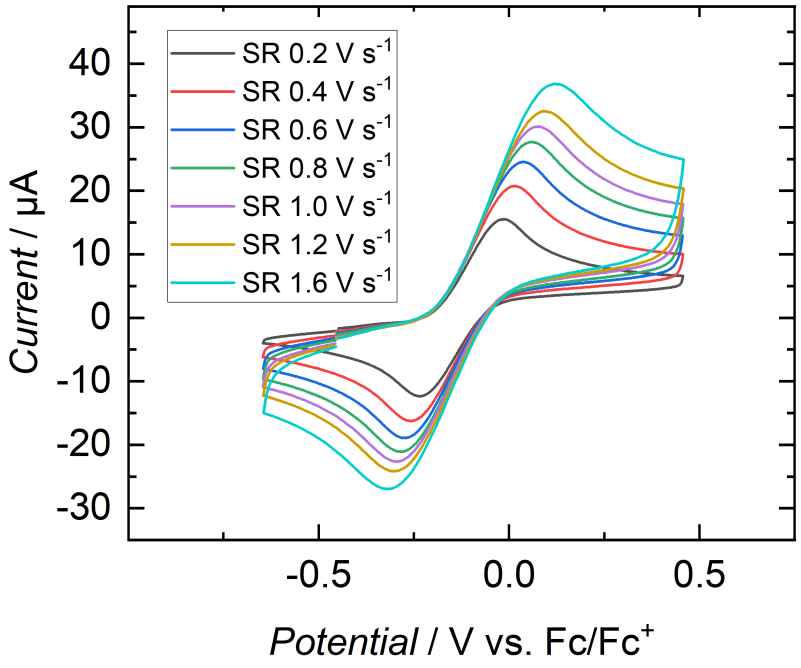

Figure S85: Cyclic voltammogram of the redox event at $E_{1/2}$ = –0.12 V *vs* Fc/Fc^+ of **3** in 1 mM THF solution with $TBAPF_6$ (1 mM) as supporting electrolyte at various scan rates (SR).

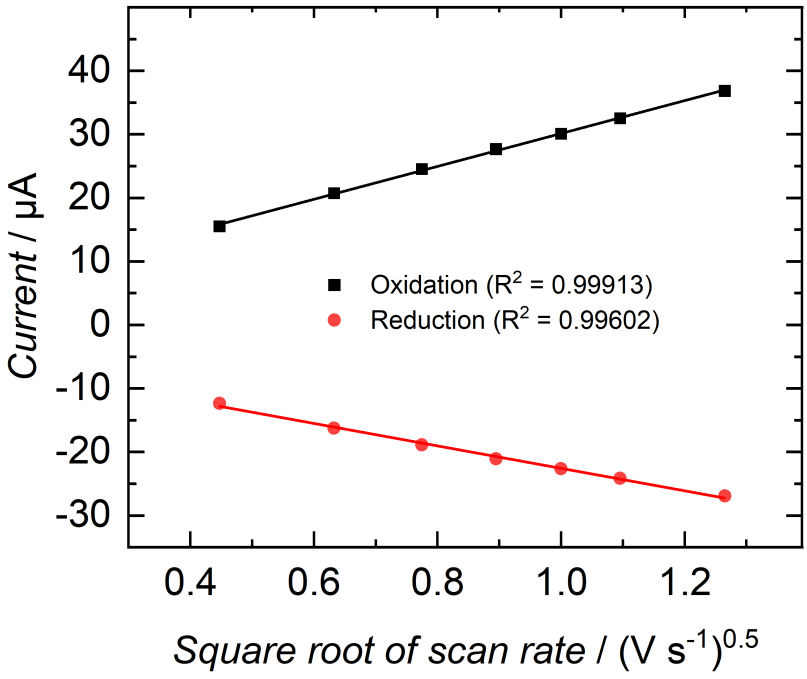

Figure S86: Randles-Sevcik-Plot of the positive and negative peak currents of the redox event at $E_{1/2}$ = –0.12 V *vs* Fc/Fc^+ of **3** (Figure S85).

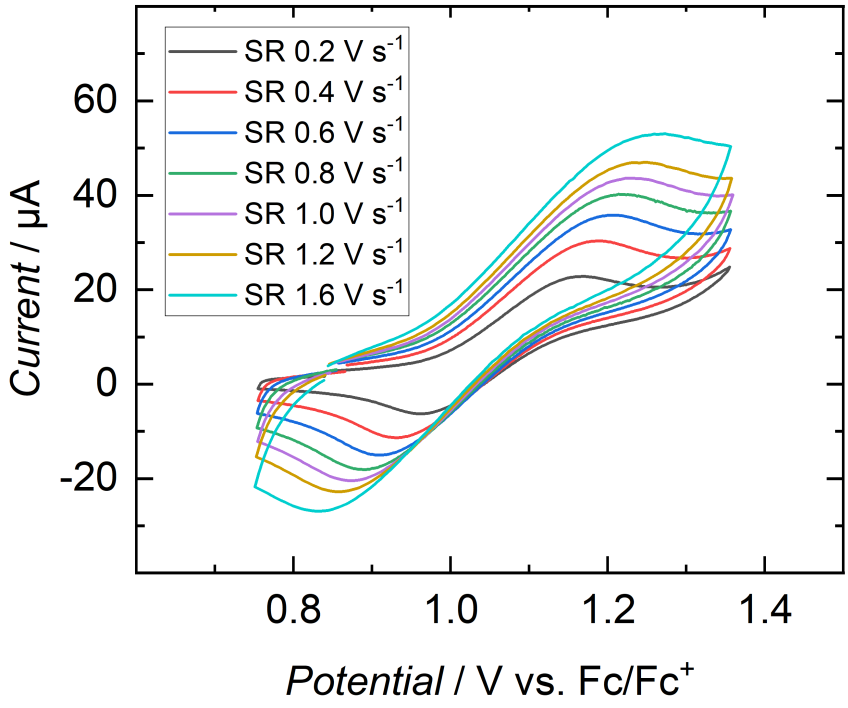

Figure S87: Cyclic voltammogram of the redox event at $E_{1/2}$ = 1.06 V *vs* Fc/Fc^+ of **3** in 1 mM THF solution with $TBAPF_6$ (1 mM) as supporting electrolyte at various scan rates (SR).

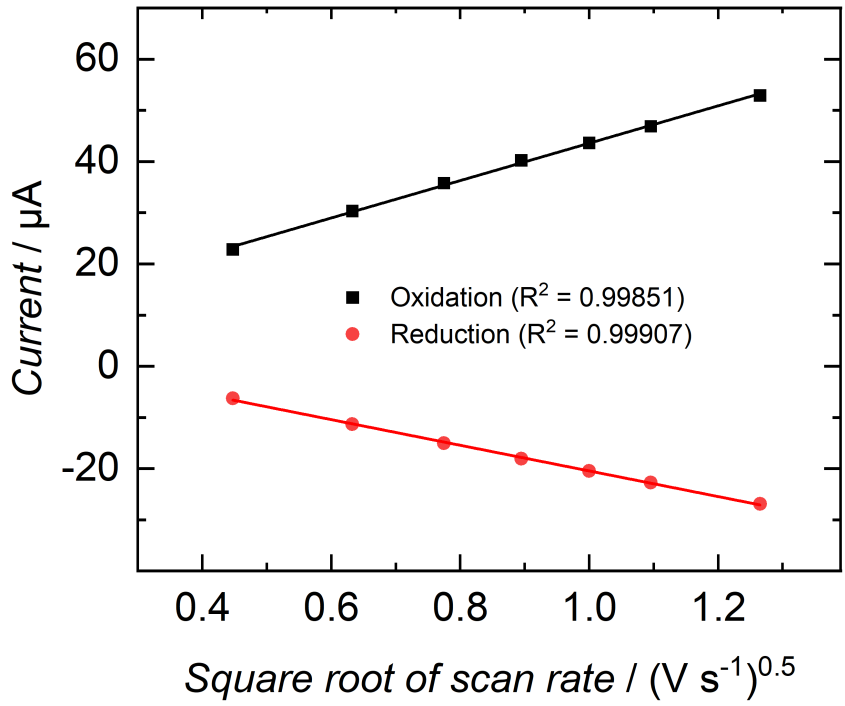

Figure S88: Randles-Sevcik-Plot of the positive and negative peak currents of the redox event at $E_{1/2}$ = 1.06 V *vs* Fc/Fc^+ of **3** (Figure S87).

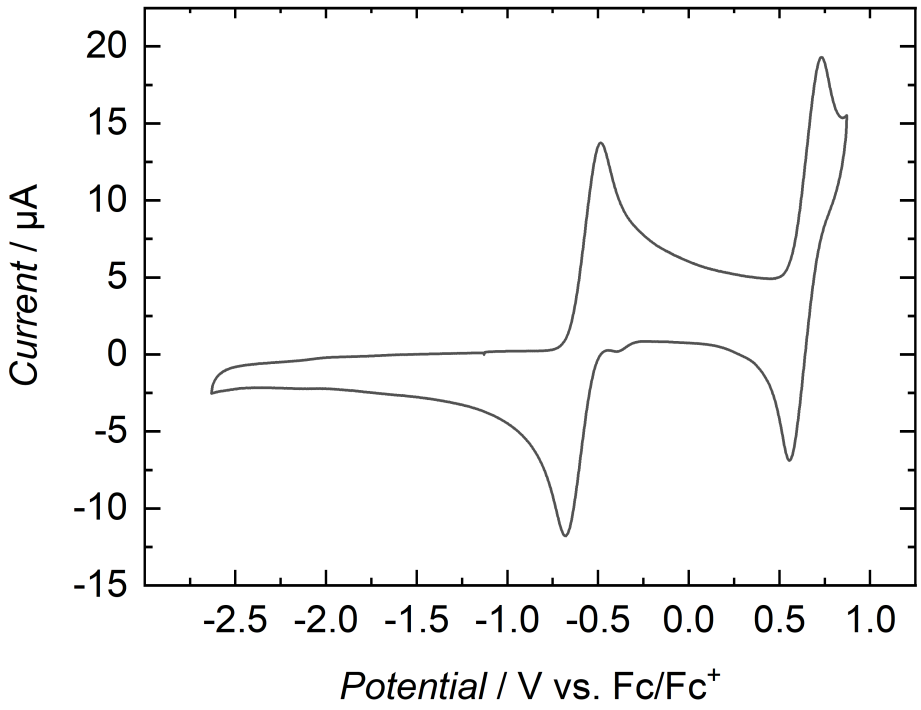

Figure S89: Cyclic voltammogram of **4** in 1 mM THF solution with $TBAPF_6$ (1 mM) as supporting electrolyte at 0.2 V s^{-1}.

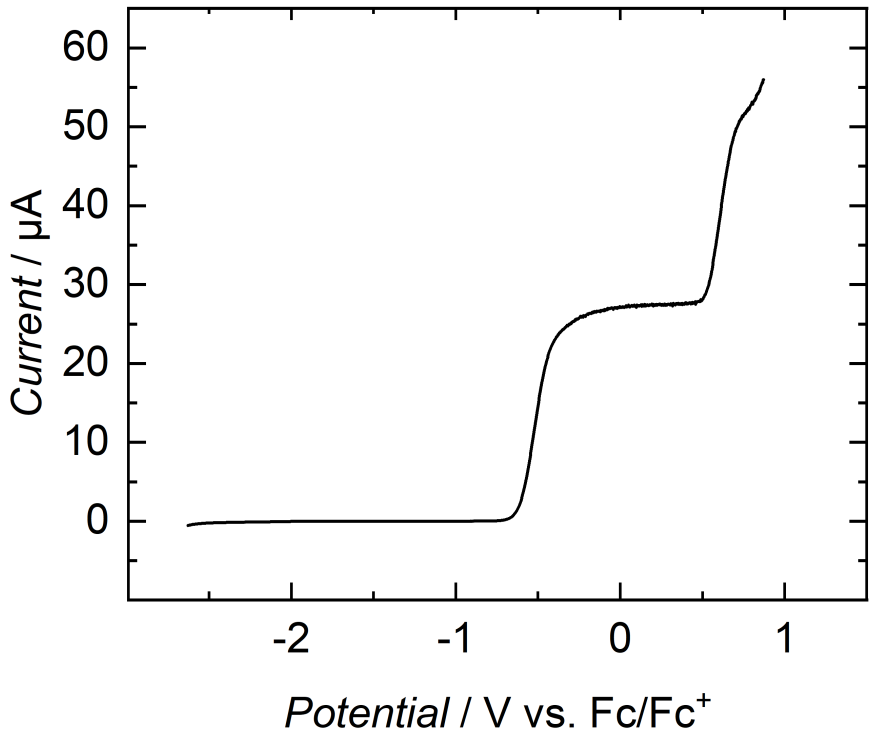

Figure S90: Linear sweep measurement of **4** in 1 mM THF solution with $TBAPF_6$ (1 mM) as supporting electrolyte at 50 mV s^{-1} and 2000 rpm.

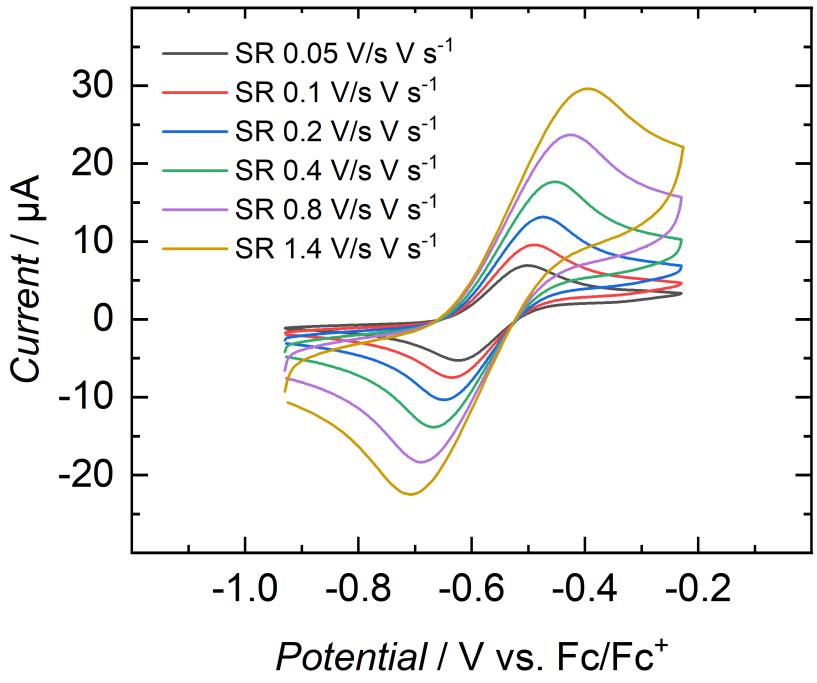

Figure S91: Cyclic voltammogram of the redox event at $E_{1/2}$ = –0.59 V *vs* Fc/Fc^+ of **4** in 1 mM THF solution with $TBAPF_6$ (1 mM) as supporting electrolyte at various scan rates (SR).

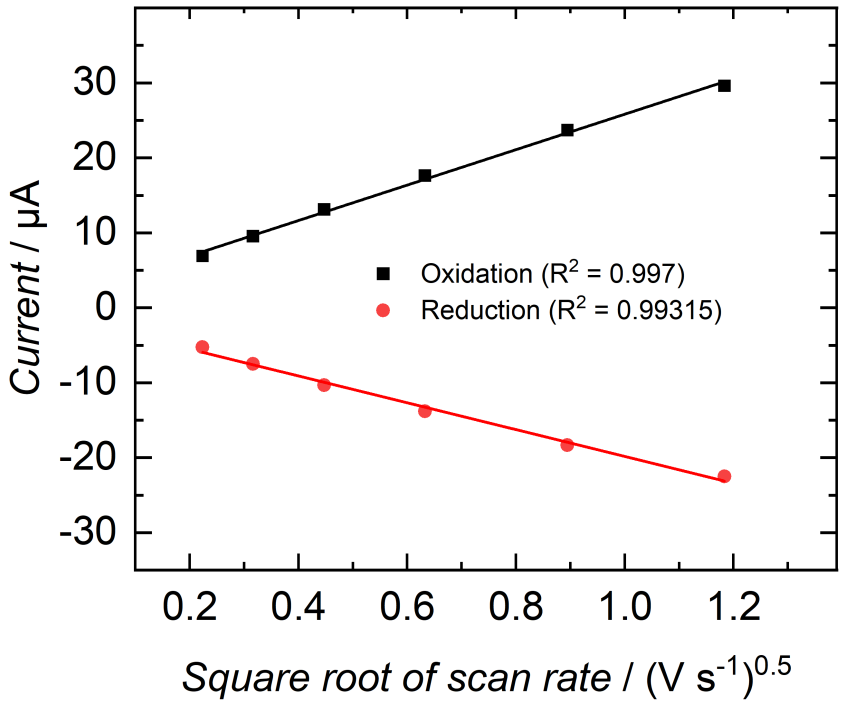

Figure S92: Randles-Sevcik-Plot of the positive and negative peak currents of the redox event at $E_{1/2}$ = –0.59 V *vs* Fc/Fc^+ of **4** (Figure S91).

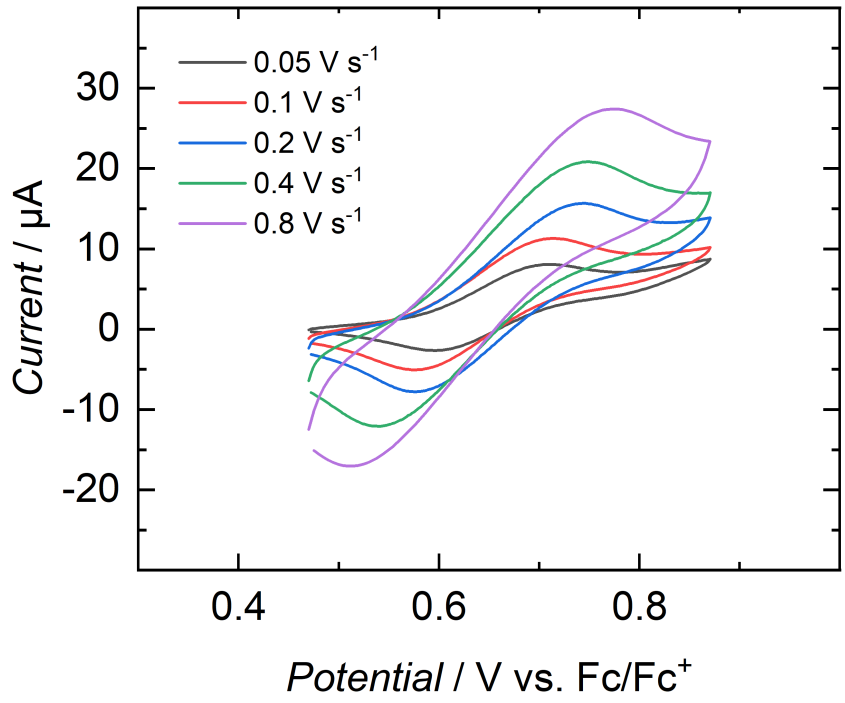

Figure S93: Cyclic voltammogram of the redox event at $E_{1/2}$ = 0.64 V *vs* Fc/Fc^+ of **4** in 1 mM THF solution with $TBAPF_6$ (1 mM) as supporting electrolyte at various scan rates (SR).

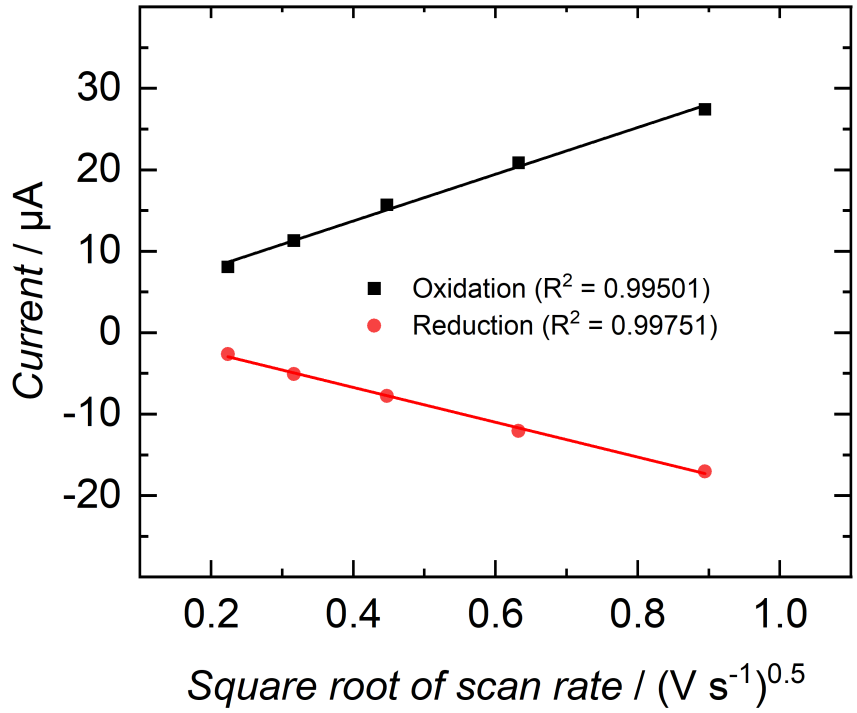

Figure S94: Randles-Sevcik-Plot of the positive and negative peak currents of the redox event at $E_{1/2}$ = 0.64 V *vs* Fc/Fc^+ of **4** (Figure S93).

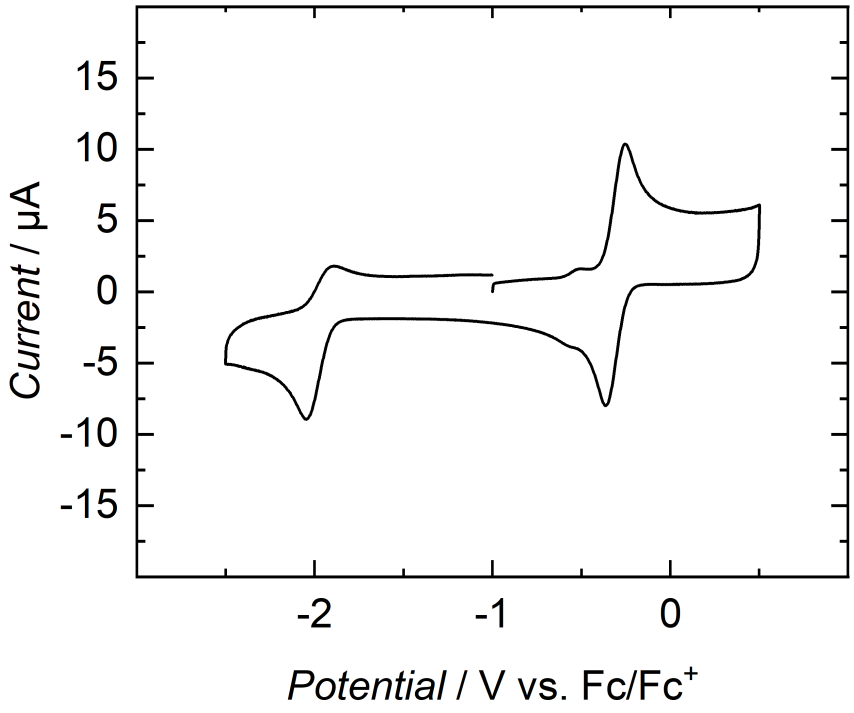

Figure S95: Cyclic voltammogram of **6** in 1 mM THF solution with $TBAPF_6$ (1 mM) as supporting electrolyte at 0.2 V s^{-1}.

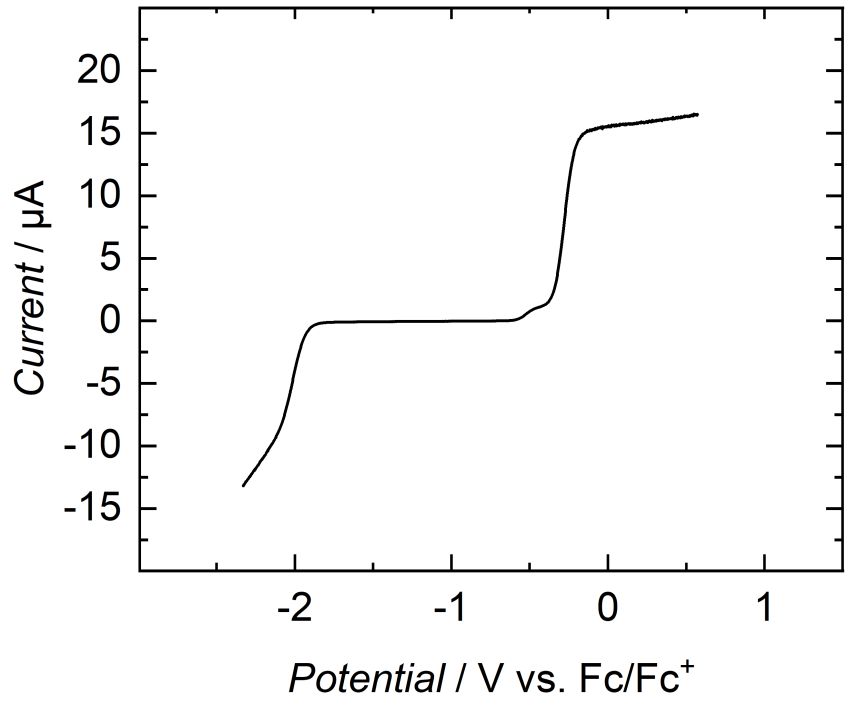

Figure S96: Linear sweep measurement of **6** in 1 mM THF solution with $TBAPF_6$ (1 mM) as supporting electrolyte at 50 mV s^{-1} and 2000 rpm.

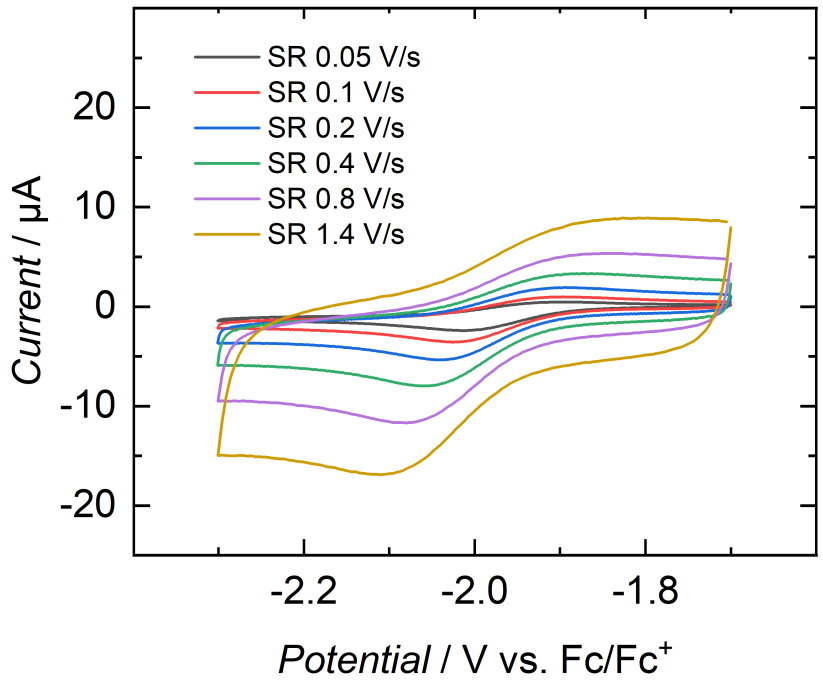

Figure S97: Cyclic voltammogram of the redox event at $E_{1/2}$ = –1.97 V *vs* Fc/Fc^+ of **6** in 1 mM THF solution with $TBAPF_6$ (1 mM) as supporting electrolyte at various scan rates (SR).

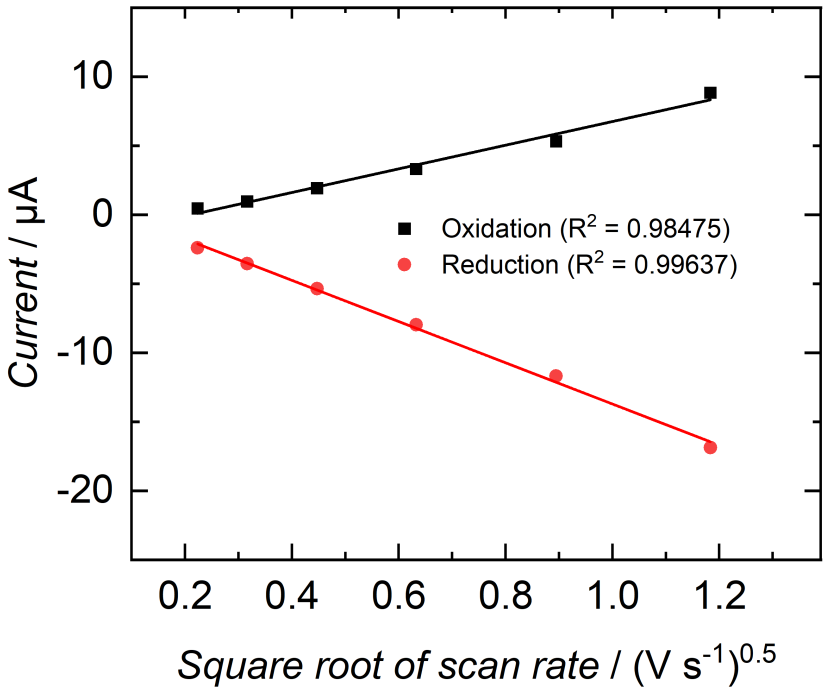

Figure S98: Randles-Sevcik-Plot of the positive and negative peak currents of the redox event at $E_{1/2}$ = –1.97 V *vs* Fc/Fc^+ of **6** (Figure S97).

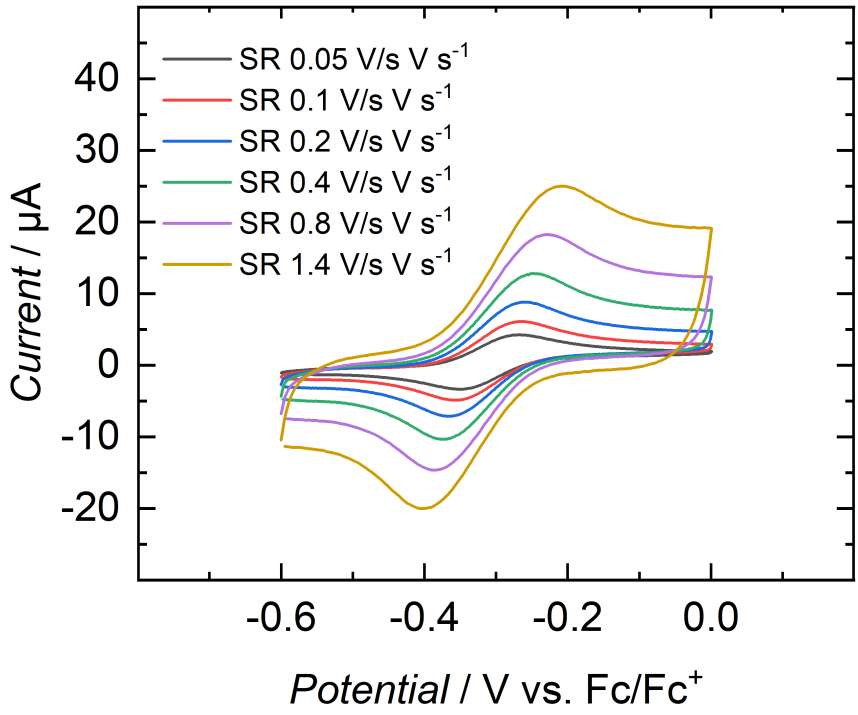

Figure S99: Cyclic voltammogram of the redox event at $E_{1/2}$ = –0.32 V *vs* Fc/Fc^+ of **6** in 1 mM THF solution with $TBAPF_6$ (1 mM) as supporting electrolyte at various scan rates (SR).

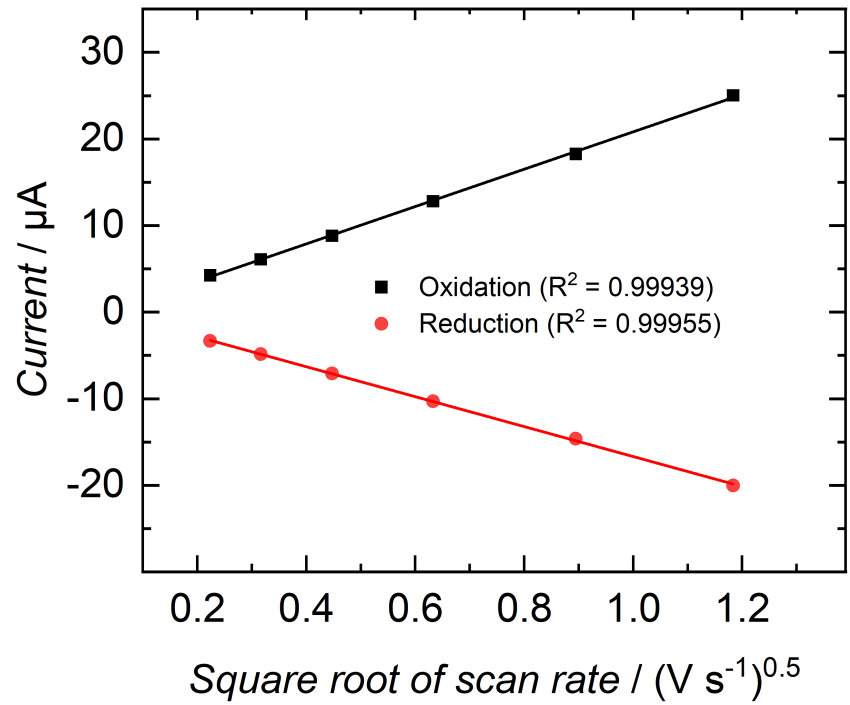

Figure S100: Randles-Sevcik-Plot of the positive and negative peak currents of the redox event at $E_{1/2}$ = –0.32 V *vs* Fc/Fc^+ of **6** (Figure S99).

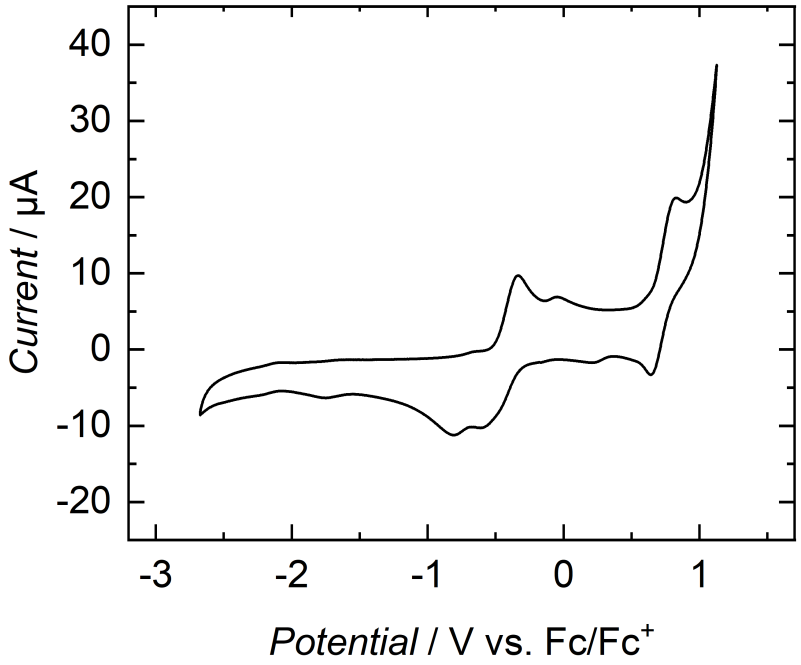

Figure S101: Cyclic voltammogram of **7** in 1 mM THF solution with $TBAPF_6$ (1 mM) as supporting electrolyte at 0.2 V s^{-1}.

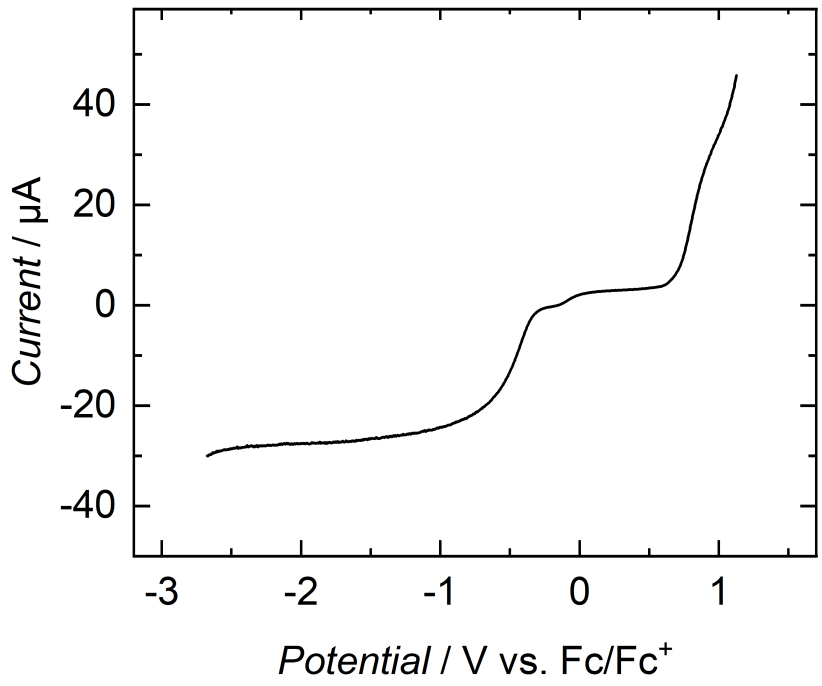

Figure S102: Linear sweep measurement of **7** in 1 mM THF solution with $TBAPF_6$ (1 mM) as supporting electrolyte at 50 mV s^{-1} and 2000 rpm.

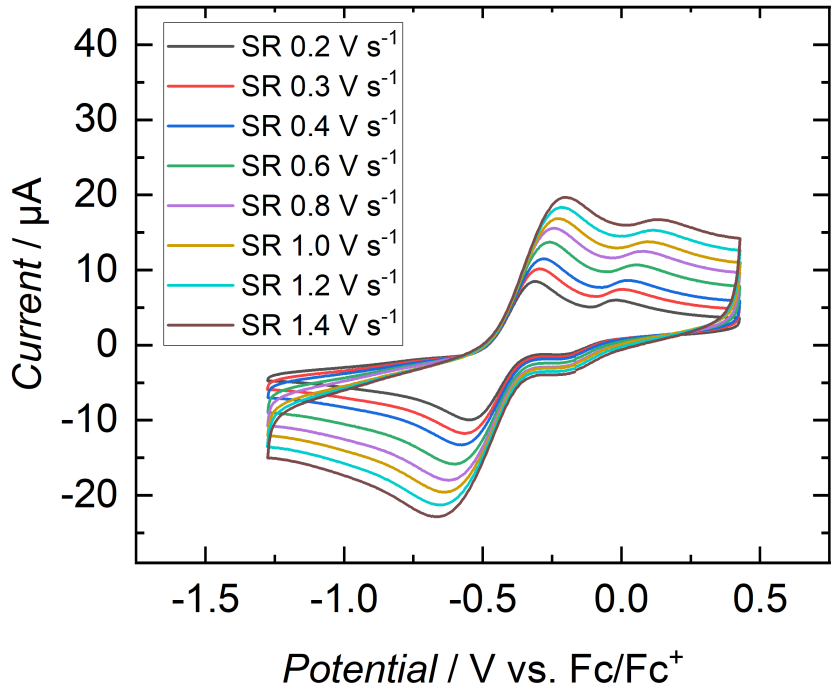

Figure S103: Cyclic voltammogram of the redox event at $E_{1/2}$ = –0.43 V *vs* Fc/Fc^+ of **7** in 1 mM THF solution with $TBAPF_6$ (1 mM) as supporting electrolyte at various scan rates (SR).

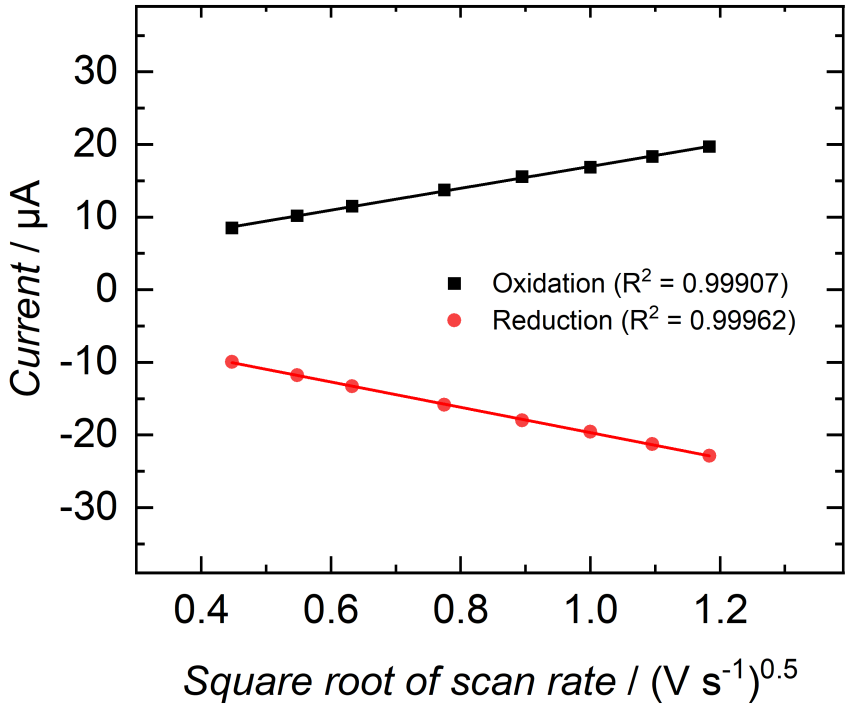

Figure S104: Randles-Sevcik-Plot of the positive and negative peak currents of the redox event at $E_{1/2}$ = –0.43 V *vs* Fc/Fc^+ of **7** (Figure S103).

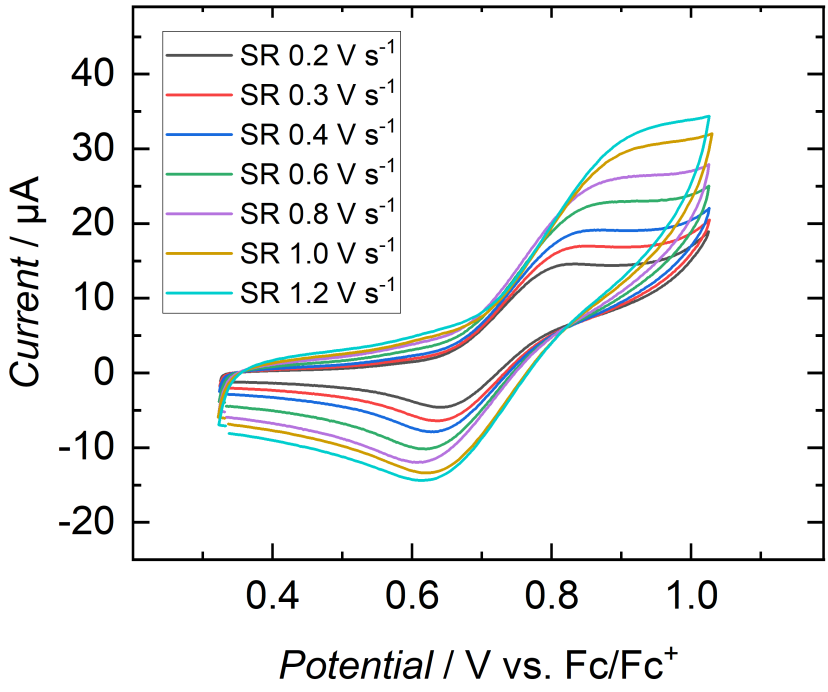

Figure S105: Cyclic voltammogram of the redox event at $E_{1/2}$ = 0.73 V *vs* Fc/Fc^+ of **7** in 1 mM THF solution with $TBAPF_6$ (1 mM) as supporting electrolyte at various scan rates (SR).

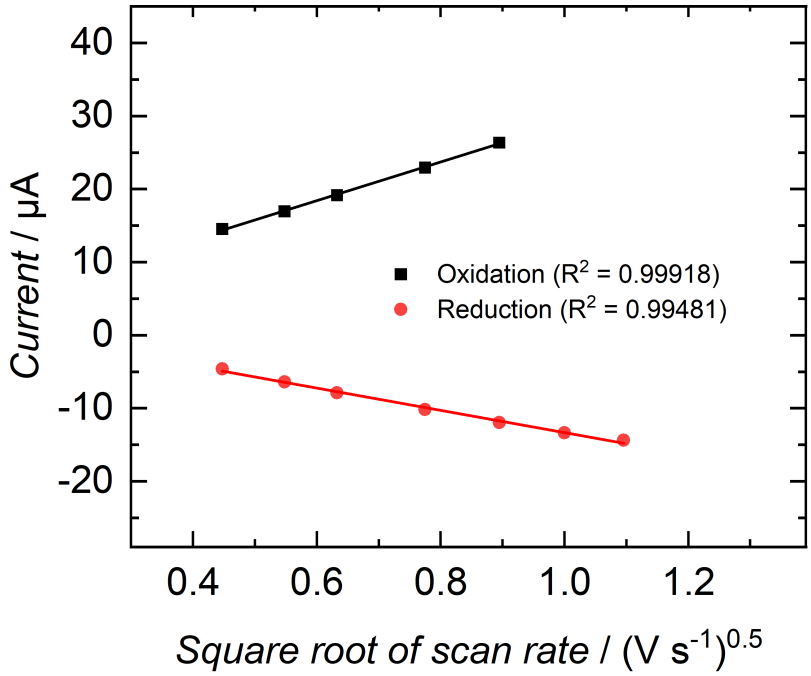

Figure S106: Randles-Sevcik-Plot of the positive and negative peak currents of the redox event at $E_{1/2}$ = 0.73 V *vs* Fc/Fc^+ of **7** (Figure S105). Peak currents of the oxidation waves at 1.0 V s^{-1} and 1.2 V s^{-1} could not be unambigously determined and were omitted.

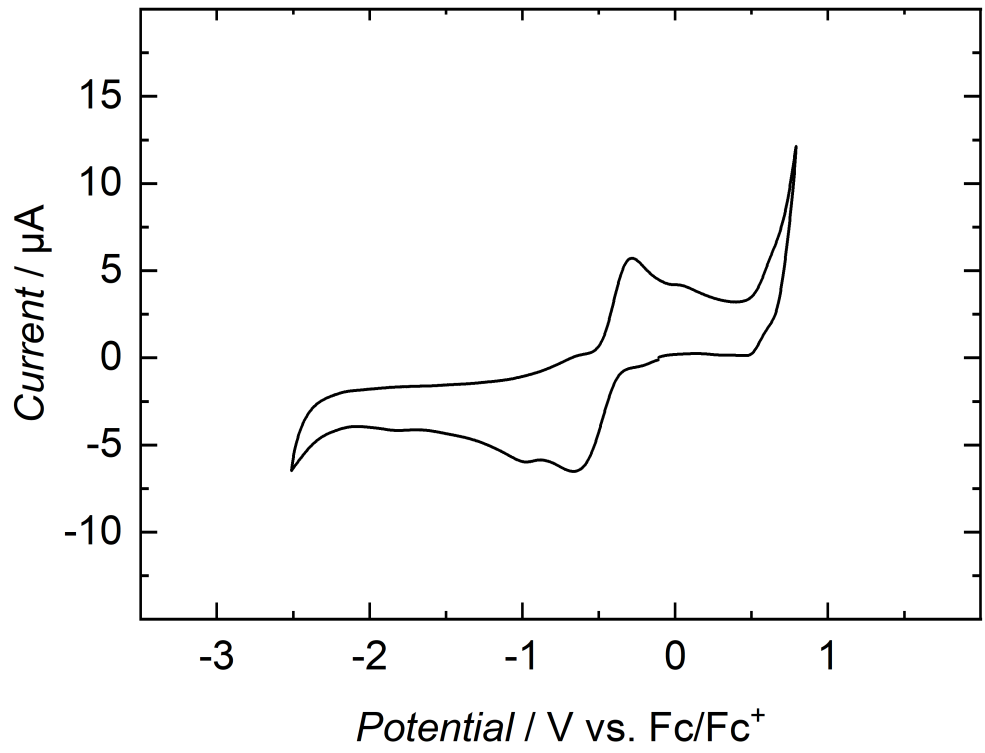

Figure S107: Cyclic voltammogram of **8** in 1 mM THF solution with $TBAPF_6$ (1 mM) as supporting electrolyte at 0.2 V s^{-1}.

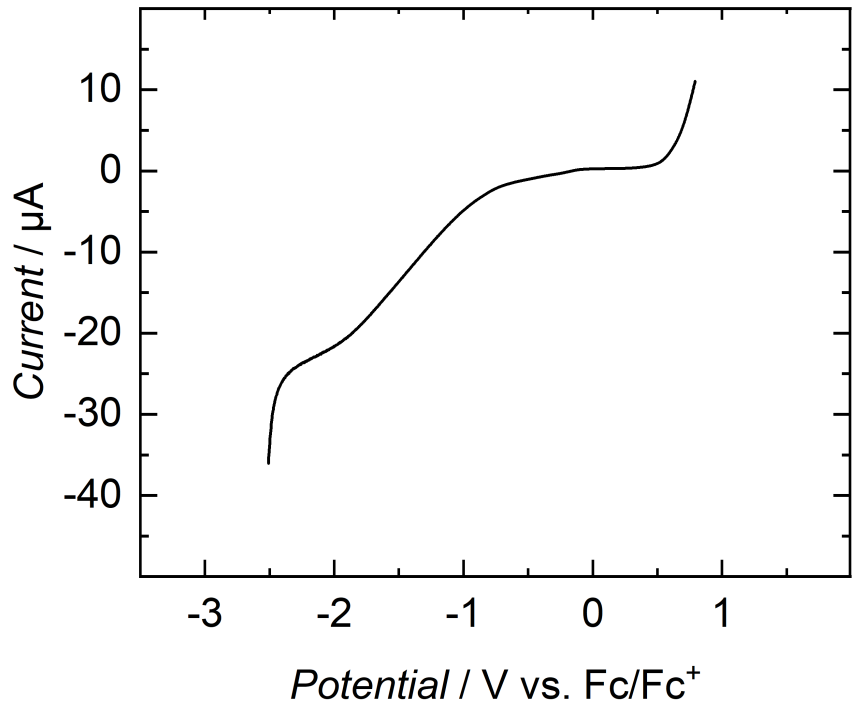

Figure S108: Linear sweep measurement of **8** in 1 mM THF solution with $TBAPF_6$ (1 mM) as supporting electrolyte at 50 mV s^{-1} and 2000 rpm.

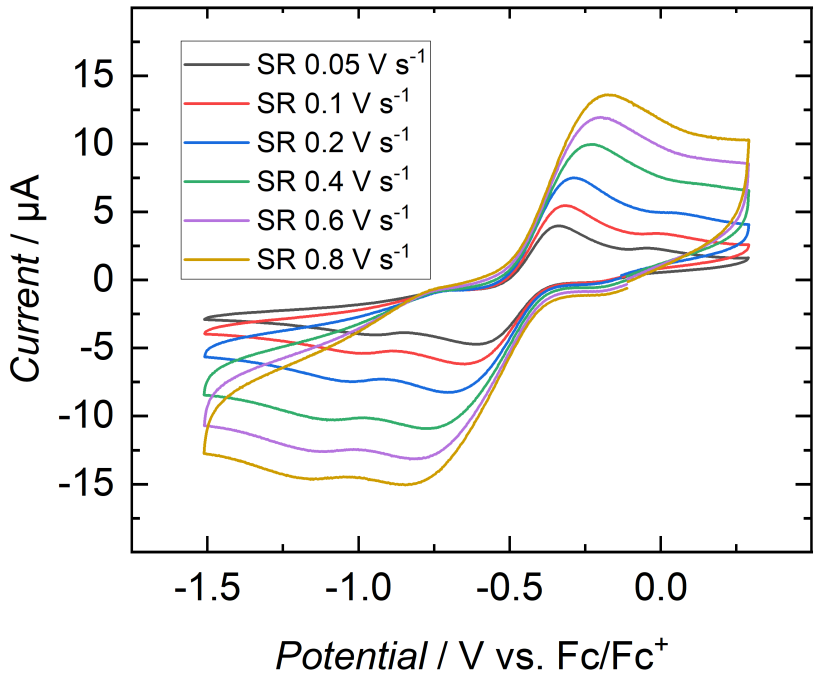

Figure S109: Cyclic voltammogram of the redox event at $E_{1/2}$ = –0.47 V *vs* Fc/Fc^+ of **8** in 1 mM THF solution with $TBAPF_6$ (1 mM) as supporting electrolyte at various scan rates (SR).

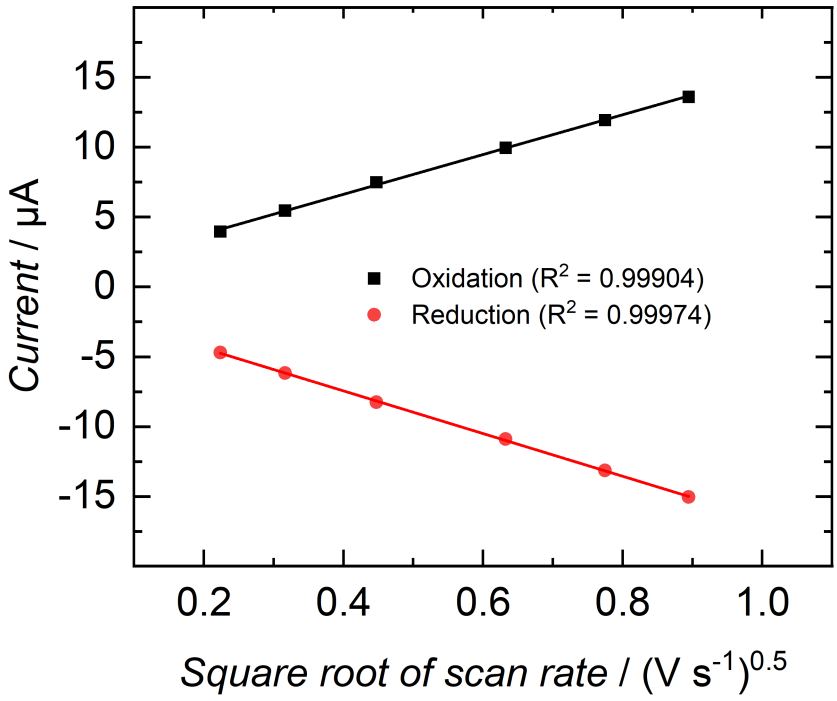

Figure S110: Randles-Sevcik-Plot of the positive and negative peak currents of the redox event at $E_{1/2}$ = –0.47 V *vs* Fc/Fc^+ of **8** (Figure S109).

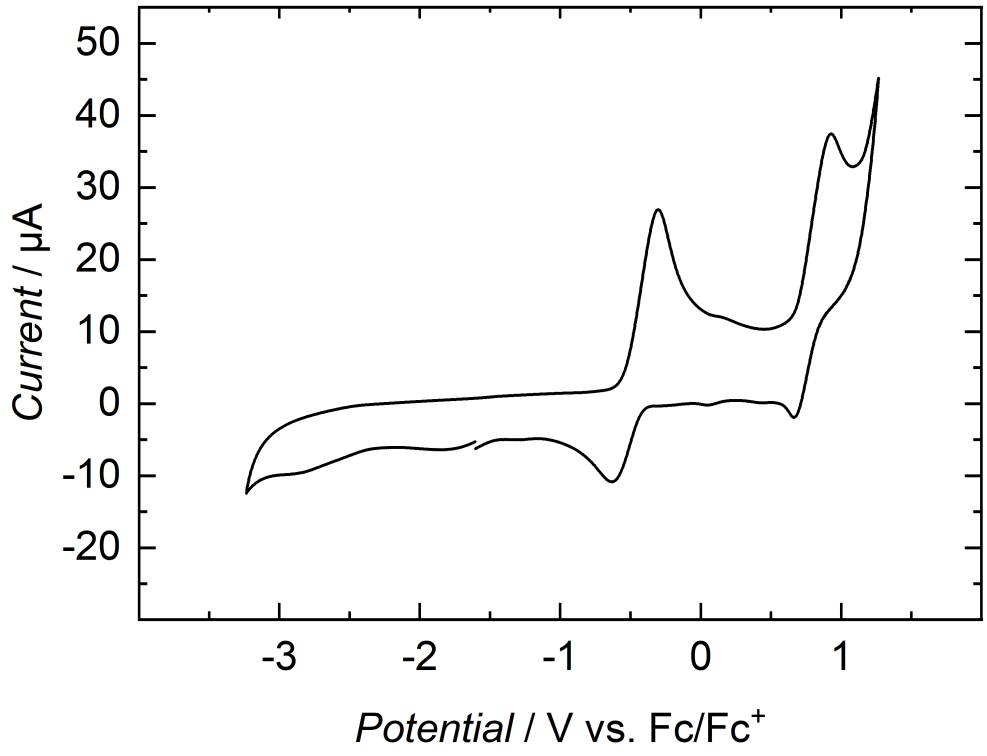

Figure S111: Cyclic voltammogram of **9** in 1 mM THF solution with $TBAPF_6$ (1 mM) as supporting electrolyte at 0.2 V s^{-1}.

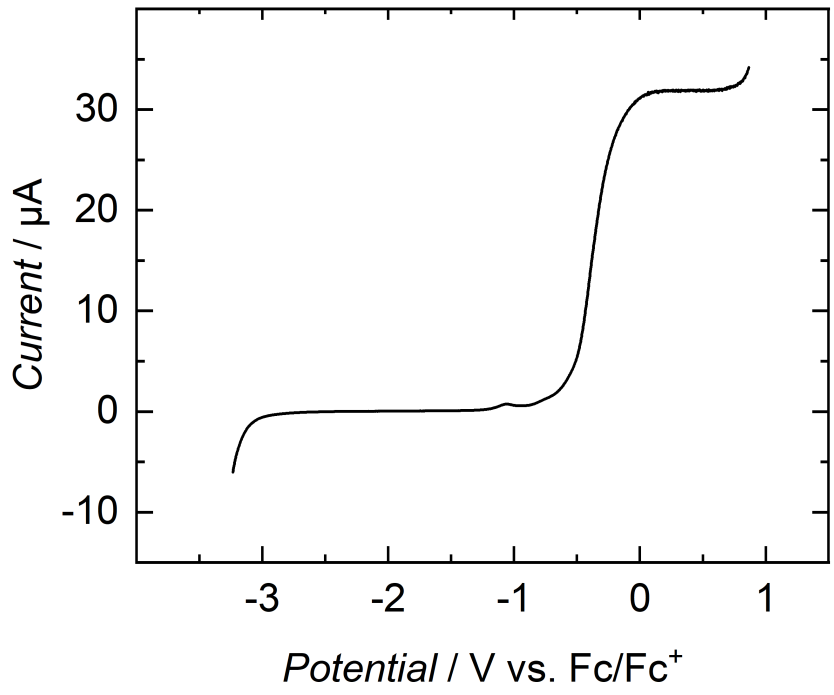

Figure S112: Linear sweep measurement of **9** in 1 mM THF solution with $TBAPF_6$ (1 mM) as supporting electrolyte at 50 mV s^{-1} and 2000 rpm.

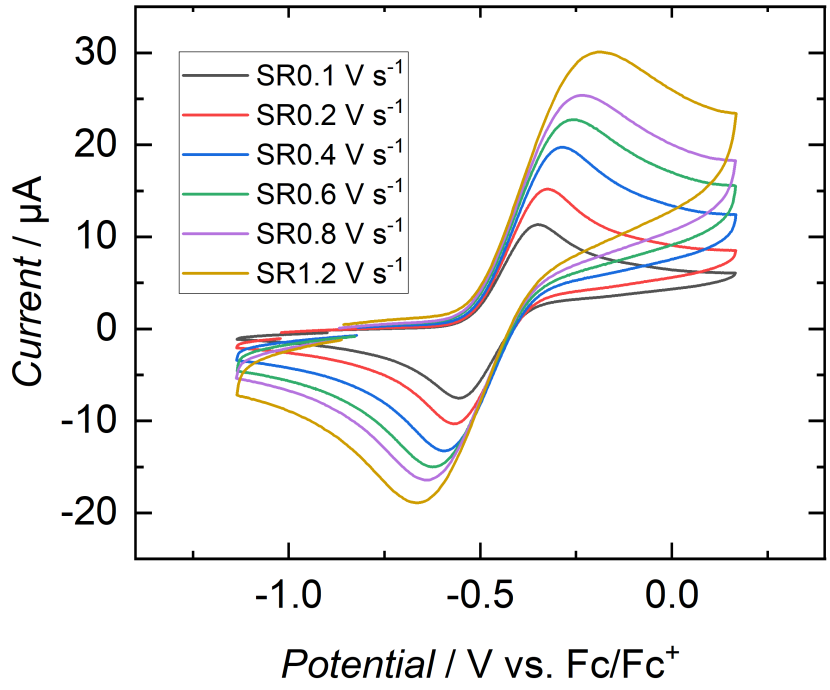

Figure S113: Cyclic voltammogram of the redox event at $E_{1/2}$ = –0.45 V *vs* Fc/Fc^+ of **9** in 1 mM THF solution with $TBAPF_6$ (1 mM) as supporting electrolyte at various scan rates (SR).

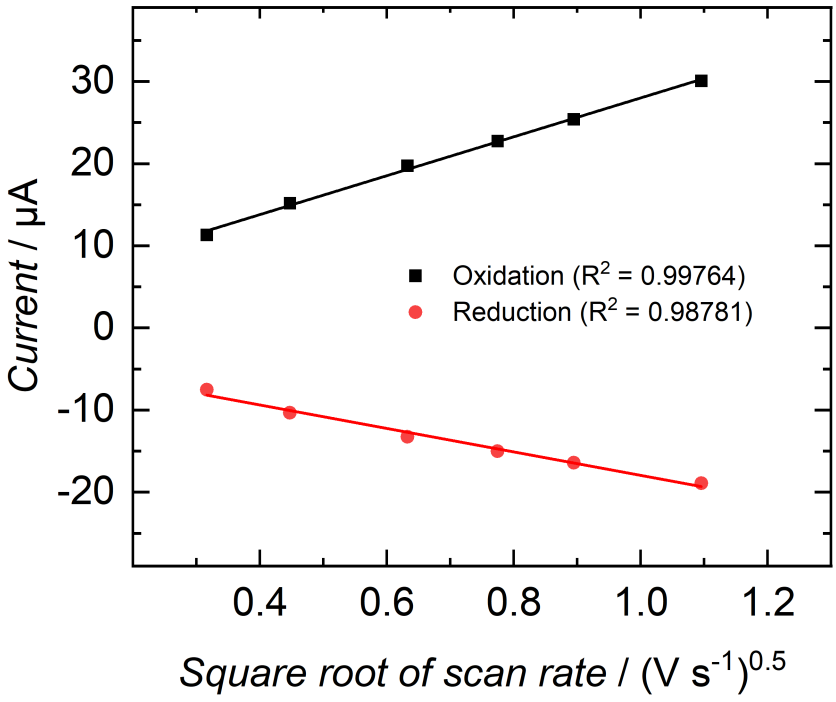

Figure S114: Randles-Sevcik-Plot of the positive and negative peak currents of the redox event at $E_{1/2}$ = –0.45 V *vs* Fc/Fc^+ of **9** (Figure S113).

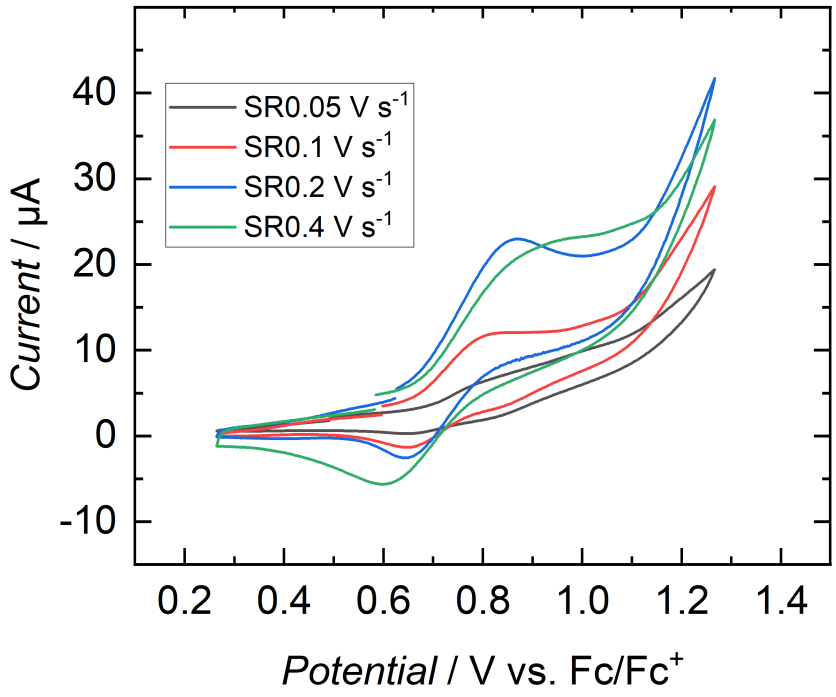

Figure S115: Cyclic voltammogram of the redox event at $E_{1/2}$ = 0.75 V *vs* Fc/Fc^+ of **9** in 1 mM THF solution with $TBAPF_6$ (1 mM) as supporting electrolyte at various scan rates (SR).

Single Crystal X-Ray Structure Determinations

CCDC-2080557 (for **2** • 2 THF), **CCDC-2150855** (for **3** • 2 Et_2O), **CCDC-2150856** (for **4** • 2 THF), **CCDC-2150857** (for **5** • 2 Et_2O), **CCDC-2150858** (for **6** • 1.5 THF), **CCDC-2150859** (for **7** • 3.5 C_6H_6) and **CCDC-2150860** (for **8** • 3.5 C_6H_6) contain the supplementary crystallographic data for this paper. This data can be obtained free of charge via http://www.ccdc.cam.ac.uk/products/csd/request/ (or from Cambridge Crystallographic Data Centre, 12 Union Road, Cambridge, CB2 1EZ, UK (fax: ++44-1223-336-033; e-mail: deposit@ccdc.cam.ac.uk).

Crystallographic Details

Suitable single crystal of the investigated compounds were embedded in protective perfluoropolyalkyether oil and transferred to the cold nitrogen gas stream of the diffractometer. Intensity data were collected using MoK_α radiation (λ = 0.71073 Å) on a Bruker Kappa *IμS* Duo diffractometer equipped with QUAZAR focussing Montel optics and either an APEX 2 CCD detector (for **2**) or a PHOTON 2 CPAD detector (for **3**, **5**, **6**, **7**, and **8**). For **4**, intensity data were collected on a Bruker Smart APEX 2 diffractometer using MoK_α radiation (λ = 0.71073 Å, Triumph curved graphite monochromator). Data were corrected for Lorentz and polarization effects, semi-empirical absorption corrections were performed on the basis of multiple scans using *SADABS*.[6,7] The structures were solved by direct methods (*SHELX XT* 2014/5)[8] and refined by full-matrix least-squares procedures on F^2 using *SHELXL* 2018/3.[9] Material for publication has been prepared using *OLEX2*.[10] All non-hydrogen atoms were refined with anisotropic displacement parameters.

For **2** • 2 THF, five low-angle reflections, obviously affected by the beam stop, were excluded from the refinement. Two significant residual electron density maxima were found in close vicinity to the uranium atom (< 1.08 Å away). These maxima were attributed to truncation effects and do not have chemical significance. The compound crystallized with two molecules of THF per formula unit, one of which was disordered. Two alternative orientations were refined and resulted in site occupancy factors of 67(2) and 33(2) % for the atoms O100 – C104 and O110 – C114, respectively. Similarity restraints were applied to the anisotropic displacement parameters of the disordered atoms.

Compound **3** • 2 Et_2O crystallized with a total of 2 molecules of diethyl ether per formula unit. One of the *t*Bu groups of the ligand (at C20) was disordered. Two alternative orientations were refined and resulted in site occupancies of 60.6(4) and 39.4(4) % for the atoms C21 – C23 and C21A – C23A, respectively. Also, one of the diethyl ether solvent molecules was disordered. Two alternative orientations were refined and resulted in site occupancies of 59.6(7) and 40.4(7) % for the atoms C201 – C205 and C211 – C215, respectively. Similarity restraints were applied to the anisotropic displacement parameters of the disordered atoms of the solvent molecules.

Compound **4** • 2 THF crystallized with two molecules of THF per formula unit. Beyond that, the structure contained solvent accessible voids that were treated with the SQUEEZE procedure. According to the SQUEEZE[11] results two significant solvent accessible voids were found (calculated for space group no. 1, *P*1) with a volume of 378 $Å^3$ and a content of 84 electrons each. This is consistent with *e.g.* two molecules of tetrahydrofuran per void (electron count per tetrahydrofuran = 40, and a volume of 189 $Å^3$ per tetrahydrofuran; typical small solvent molecule volumes are found in between 100 and 200 $Å^3$). One of the *t*Bu groups was disordered. Two alternative orientations were refined and resulted in site occupancies of 56.4(6) and 43.6(6) % for the atoms C21 – C23 and C21A – C23A, respectively. One of the THF solvent molecules was also disordered. Two alternative orientations were refined and resulted in site occupancies of 38.7(8) and 61.3(8) % for the atoms O100 – C104 and O110 – C114, respectively. Similarity restraints were applied in the refinement of the anisotropic displacement parameters of the disordered atoms and the atoms of both THF solvent molecules. The position of the O4 bound hydrogen atom H4 (hydroxy group at U1) was unequivocally located in a difference Fourier synthesis and subsequently allowed to ride on its carrier atom. This O-H group is involved in hydrogen bonding to one of the located solvent tetrahydrofuran molecules (O4 – H4 ⋯ O100: O4 – H4 0.87 Å, H4 ⋯ O100, 2.06 Å, O4 ⋯ O100 2.928(16) Å, O4 – H4 ⋯ O100 176.0°; for the alternative location of the THF molecule: O4 – H4 ⋯ O110: O4 – H4 0.87 Å, H4 ⋯ O110, 2.16 Å, O4 ⋯ O110 3.017(19) Å, O4 – H4 ⋯ O110 170.2°).

The crystals of **5** • 2 Et_2O turned out to be mixed crystals consisting of the di-fluorido and the mono-fluorido species, in the present case in a ratio of 79.7(6):20.3(6) %. The compound crystallized with two molecules of diethyl ether in its asymmetric unit. For one of these solvent molecules (C101 – C105) similarity restraints were applied to the anisotropic displacement parameters of the atoms.

Compound **6** • 1.5 THF crystallized with 1.5 molecules of THF per formula unit, both of which were disordered. For one THF two alternative orientations were refined and resulted in site occupancies of 55(1) and 45(1) % for the atoms O100 – C104 and O110 – C114, respectively. The second THF (O200 – C204) was situated on a twofold crystallographic axis and was therefore given at site occupancy factor of 0.5. Similarity and pseudo-isotropic restraints were applied to the anisotropic displacement parameters of the disordered atoms.

In the crystal structure of **7** • 3.5 C_6H_6 one of the *t*Bu groups of the ligand was disordered. Two alternative orientations were refined and resulted in site occupancies of 60.4(7) and 39.6(7) % for the atoms C51 – C53 and C51A – C53A, respectively. The compound crystallized with a total of 3.5 molecules of benzene per formula unit with half a molecule of benzene being situated on a crystallographic twofold rotation axis (Wyckoff position 2*e*). Similarity restraints were applied to the anisotropic displacement parameters of the disordered atoms and of the atoms of the solvent molecule C301 – C306. Further pseudo-isotropic restraints were applied to the anisotropic displacement parameters of the atoms of the disordered *t*Bu group (C51 – C53A). The position of the O4 bound hydrogen atom H4 could not be unequivocally derived from a difference Fourier synthesis, although two residual electron density maxima were found in approximate positions at O4. We have decided to use the O4 bound hydrogen atom in a calculated position and subsequently allowed it to ride on its carrier oxygen atom. Further evidence for the presence of the hydroxyl group comes from the fact that the unit cell volume of **7** • 3.5 C_6H_6 is by 24.5 $Å^3$ significantly larger than that of the oxo analogue **8** • 3.5 C_6H_6 which crystallizes isostructurally to the hydroxo compound **7**. In a study on unitary crystal volumes from an increment system (A. Immirzi, B. Perini, *Acta Cryst.* 1977, **A33**, 216 – 218) a mean hydrogen atom volume of 6.9 $Å^3$ has been determined for organic compounds. This is consistent with the increase of the volume by four additional hydrogen atoms in **7** • 3.5 C_6H_6 in comparison to **8** • 3.5 C_6H_6. Similarly, the U – O4 (hydroxo) bond distance in **7** • 3.5 C_6H_6 of 2.052(2) Å is significantly longer than the U – O4 (oxo) bond distance in **8** • 3.5 C_6H_6 of 1.949(3) Å. There are no indications of a disorder of the hydroxo with an oxo group in **7** • 3.5 C_6H_6 (*e.g.* by a conspicuous deformation of the anisotropic displacement parameters of O4).In the crystal structure of **8** • 3.5 C6H6 one of the *t*Bu groups of the ligand was disordered. Two alternative orientations were refined and resulted in site occupancies of 68.3(9) and 31.7(9) % for the atoms C50 – C53 and C50A – C53A, respectively. The compound crystallized with a total of 3.5 molecules of benzene per formula unit with half a molecule of benzene being situated on a crystallographic twofold rotation axis (Wyckoff position 2*e*). Similarity restraints

were applied to the anisotropic displacement parameters of the disordered atoms and of the atoms of the solvent molecule C301 – C306.

With the exception of the OH hydrogen atom in **4** • 2 THF, in all presented crystal structure determinations the hydrogen atoms were placed in positions of optimized geometry. The isotropic displacement parameters of all H atoms were tied to those of the corresponding carrier atoms by a factor of 1.2 or 1.5.

Crystallographic data, data collection, and structure refinement details are given in Table S1 – S3. Molecular structures of the complexes (solvent molecules are depicted) in Figures S104 – S110.

Table S1: Crystallographic data, data collection and refinement details for **2**, **3** and **4**

	2 • 2 THF	**3** • 2 Et_2O	**4** • 2 THF
Empirical Formula	$C_{62}H_{101}ClN_4O_5U$	$C_{62}H_{105}FN_4O_5U$	$C_{62}H_{102}N_4O_6U$
Mol. weight [g/mol]	1255.94	1243.52	1237.50
Crystal size [mm^3]	0.21×0.08×0.03	0.26×0.22×0.07	0.29×0.16×0.05
Temperature [K]	100	100	100
Crystal system	orthorhombic	monoclinic	monoclinic
Space group	$P2_12_12_1$	$P2_1/c$	$P2_1/n$
a [Å]	15.083(3)	17.1229(7)	10.7445(6)
b [Å]	17.018(3)	13.5864(5)	16.3263(9)
c [Å]	24.513(5)	27.4309(11)	37.618(2)
α [°]	90	90	90
β [°]	90	100.063(1)	90.093(3)
γ [°]	90	90	90
V [A^3]	6292(2)	6283.3(4)	6598.9(6)
Z	4	4	4
ρ_{calc} [g/cm^3]	1.326	1.315	1.246
μ [mm^{-1}]	2.670	2.634	2.506
F(000)	2600	2584	2568
T_{min}; T_{max}	0.567; 0.746	0.630; 0.746	0.635; 0.746
2Θ interval [°]	2.8 ≤ 2 Θ ≤ 54.9	5.3 ≤ 2 Θ ≤ 59.2	2.1 ≤ 2 Θ ≤ 57.5
Coll. Refl.	179377	143114	165247
Indep. Refl.; R_{int}	14173, 0.110	17649, 0.028	17052, 0.054
Obs. refl. $I_o \geq 2\sigma(I)$	12099	15982	14244
No. ref. param.	723	760	732
wR_2 (all data)	0.1308	0.0451	0.0780
R_1 ($I_o > 2\sigma(I)$)	0.0493	0.0188	0.0357
GooF on F^2	1.109	1.047	1.125
$\Delta\rho_{max/min}$ [e $Å^{-3}$]	6.097; –1.126	1.104; –0.551	1.610; –2.972
Absolute structure Parameter[12]	0.007(3)	-	-

Table S2: Crystallographic data, data collection and refinement details for **5**, **6** and **7**

	5 • 2 Et_2O	**6** • 1.5 THF	**7** • 3.5 C_6H_6
Empirical Formula	$C_{62}H_{105}F_{1.8}N_4O_5U$	$C_{60}H_{97}N_4O_{5.5}U$	$C_{75}H_{107}F_6N_4O_4SbU$
Mol. weight [g/mol]	1258.63	1200.44	1602.42
Crystal size [mm^3]	0.21×0.19×0.14	0.19×0.09×0.04	0.19×0.07×0.05
Temperature [K]	100	100	100
Crystal system	monoclinic	monoclinic	monoclinic
Space group	$P2_1/n$	$C2/c$	$P2/c$
a [Å]	13.5741(5)	30.404(6)	23.6848(8)
b [Å]	15.3727(6)	10.566(2)	12.0981(5)
c [Å]	30.4035(12)	37.842(8)	27.9247(11)
α [°]	90	90	90
β [°]	102.168(1)	106.97(3)	113.046(1)
γ [°]	90	90	90
V [A^3]	6201.8(4)	11627(4)	7363.0(5)
Z	4	8	4
ρ_{calc} [g/cm^3]	1.348	1.372	1.446
μ [mm^{-1}]	2.671	2.842	2.628
F(000)	2613	4968	3256
T_{min}; T_{max}	0.578; 0.746	0.649; 0.746	0.636; 0.746
2Θ interval [°]	3.6 ≤ 2 Θ ≤ 59.2	4.0 ≤ 2 Θ ≤ 55.8	3.6 ≤ 2 Θ ≤ 59.2
Coll. Refl.	118302	211780	128434
Indep. Refl.; R_{int}	17438, 0.047	13853, 0.064	20670, 0.081
Obs. refl. $F_0 \geq 4\sigma(F)$	15223	11084	17059
No. ref. param.	700	837	858
wR_2 (all data)	0.0758	0.0952	0.0717
R_1 (I > 2σ(I))	0.0348	0.0482	0.0351
GooF on F^2	1.129	1.135	1.089
$\Delta\rho_{max/min}$ [e $Å^{-3}$]	1.362; –2.120	1.481; –2.379	1.242; –0.969
Absolute structure Parameter[12]	-	-	-

Table S3: Crystallographic data, data collection and refinement details for **8**

	8 • 3.5 C_6H_6
Empirical Formula	$C_{75}H_{106}F_6N_4O_4SbU$
Mol. weight [g/mol]	1601.41
Crystal size [mm^3]	0.12×0.06×0.04
Temperature [K]	100
Crystal system	monoclinic
Space group	*P*2/*c*
a [Å]	23.6833(13)
b [Å]	12.0691(6)
c [Å]	27.9262(13)
α [°]	90
β [°]	113.169(2)
γ [°]	90
V [A^3]	7338.5(6)
Z	4
ρ_{calc} [g/cm^3]	1.449
μ [mm^{-1}]	2.636
F(000)	3252
T_{min}; T_{max}	0.676; 0.746
2*Θ* interval [°]	4.2 ≤ 2 Θ ≤ 57.4
Coll. Refl.	280430
Indep. Refl.; R_{int}	18961, 0.081
Obs. refl. $F_0 \geq 4\sigma(F)$	16039
No. ref. param.	857
wR_2 (all data)	0.0802
R_1 (I > 2σ(I))	0.0390
GooF on F^2	1.103
$\Delta\rho_{max/min}$ [e $Å^3$]	1.876; –1.570
Absolute structure Parameter[12]	-

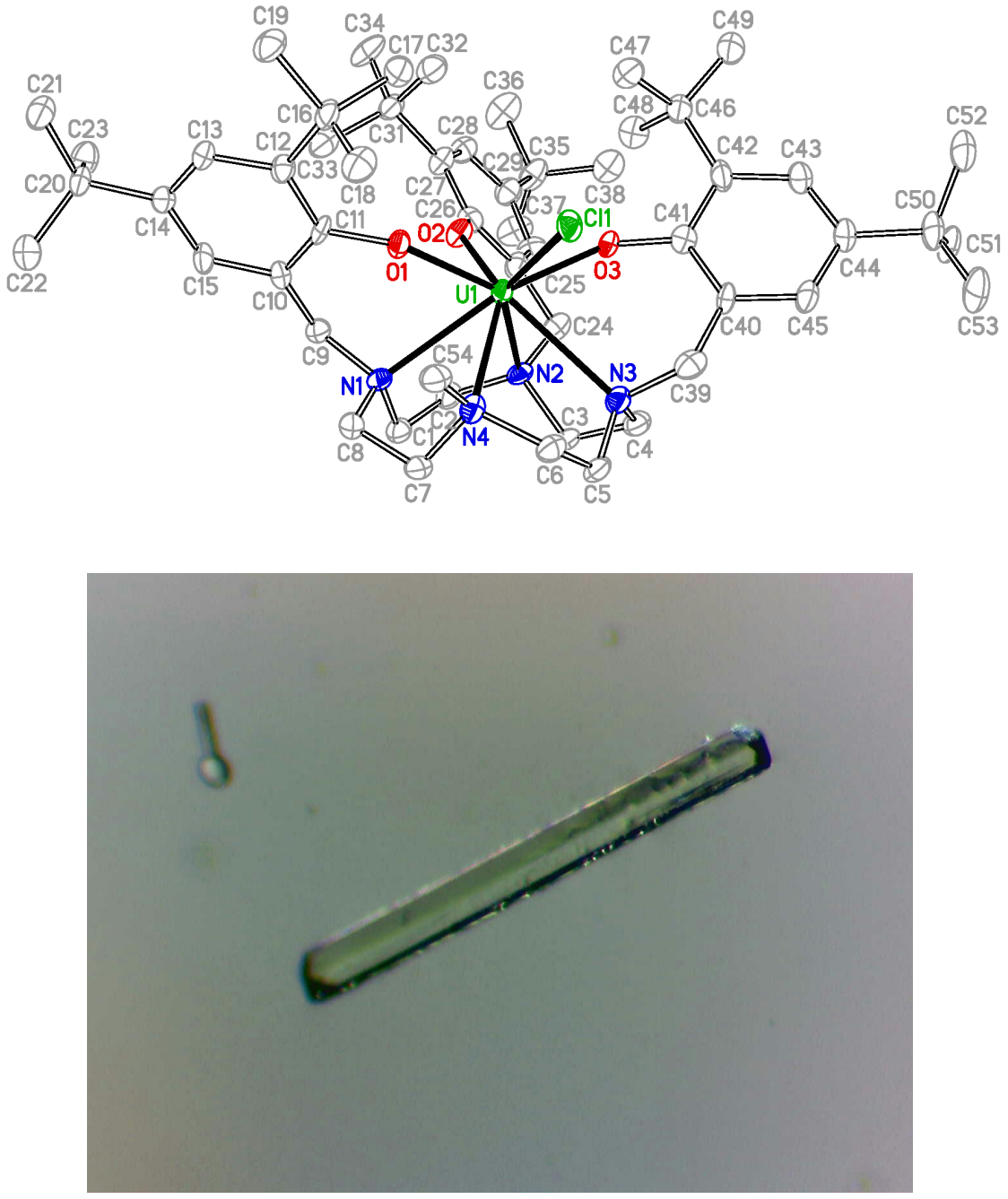

Figure S116: Top: Solid-state molecular structure with the applied numbering scheme of **2** in crystals of [((*t*-Bu,*t*-BuArO)$_3$(Me)cyclen)U^{IV}(Cl)] • 2 THF (thermal ellipsoids are at the 50% probability level, hydrogen atoms and co-crystallized solvent molecules are omitted for clarity). Bottom: A single crystal of **2** obtained from a concentrated THF solution.

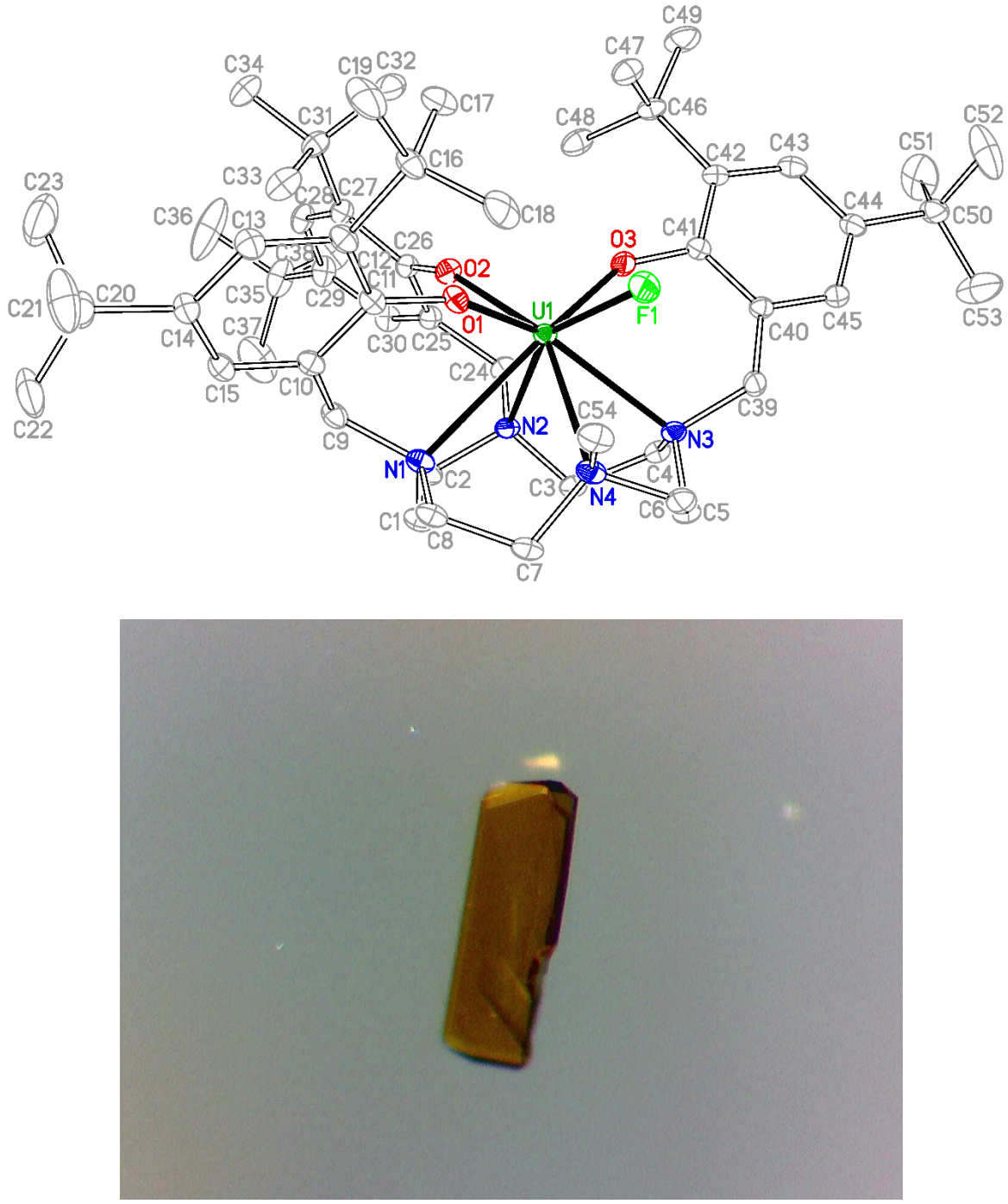

Figure S117: Top: Solid-state molecular structure with the applied numbering scheme of **3** in crystals of [((*t*-Bu,*t*-Bu$ArO)_3$(Me)cyclen)U^{IV}(F)] • 2 Et_2O (thermal ellipsoids are at the 50% probability level, hydrogen atoms and co-crystallized solvent molecules are omitted for clarity). Bottom: A single crystal of **3** obtained by diffusion of *n*-pentane into a concentrated Et_2O solution.

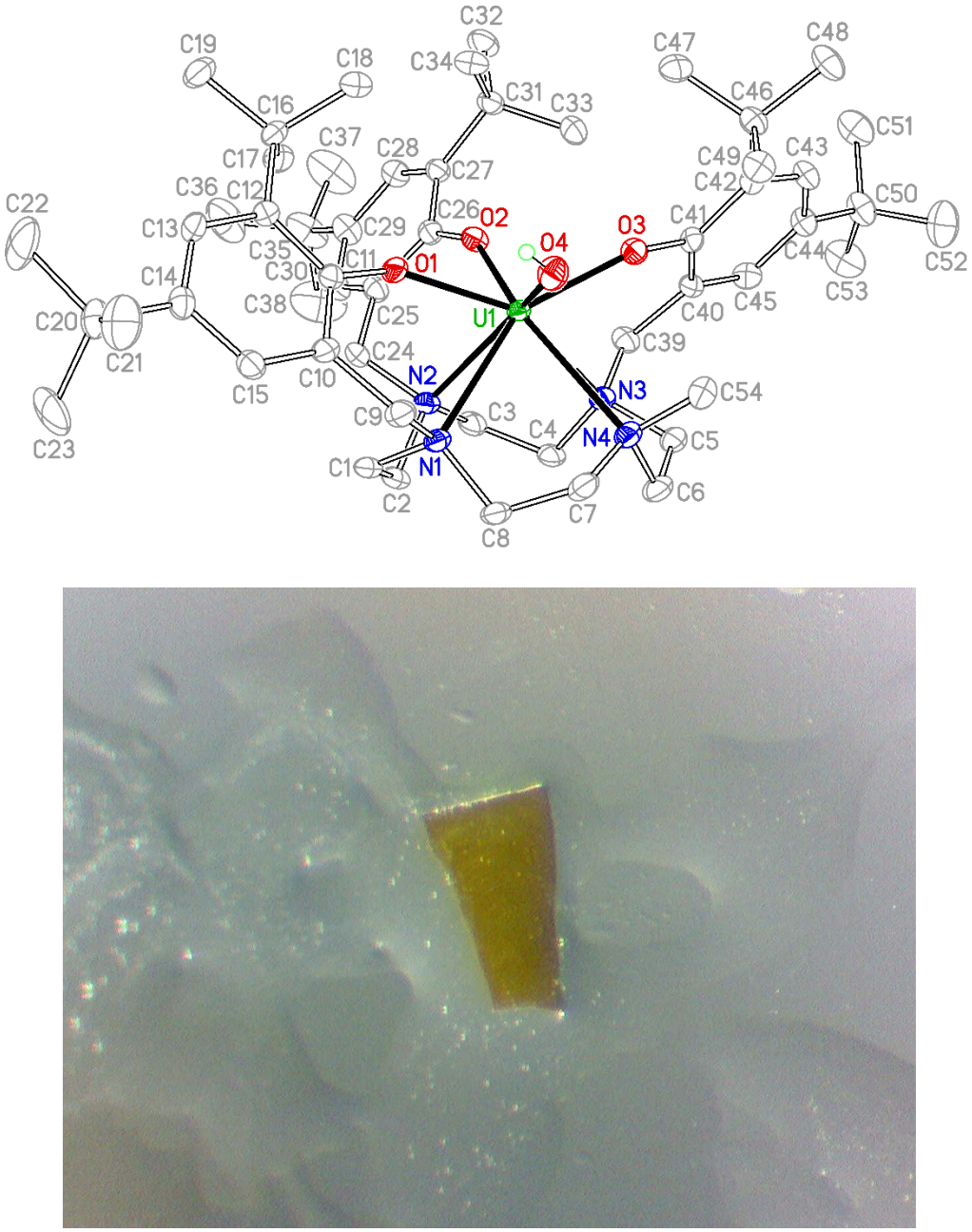

Figure S118: Top: Solid-state molecular structure with the applied numbering scheme of **4** in crystals of [(($^{t\text{-Bu},t\text{-Bu}}$ArO)$_3$(Me)cyclen)U^{IV}(OH)] • 2 THF (thermal ellipsoids are at the 50% probability level, hydrogen atoms except for the O*H* atom and co-crystallized solvent molecules are omitted for clarity). Bottom: A single crystal of **4** obtained by diffusion of a concentrated THF solution into *n*-hexane.

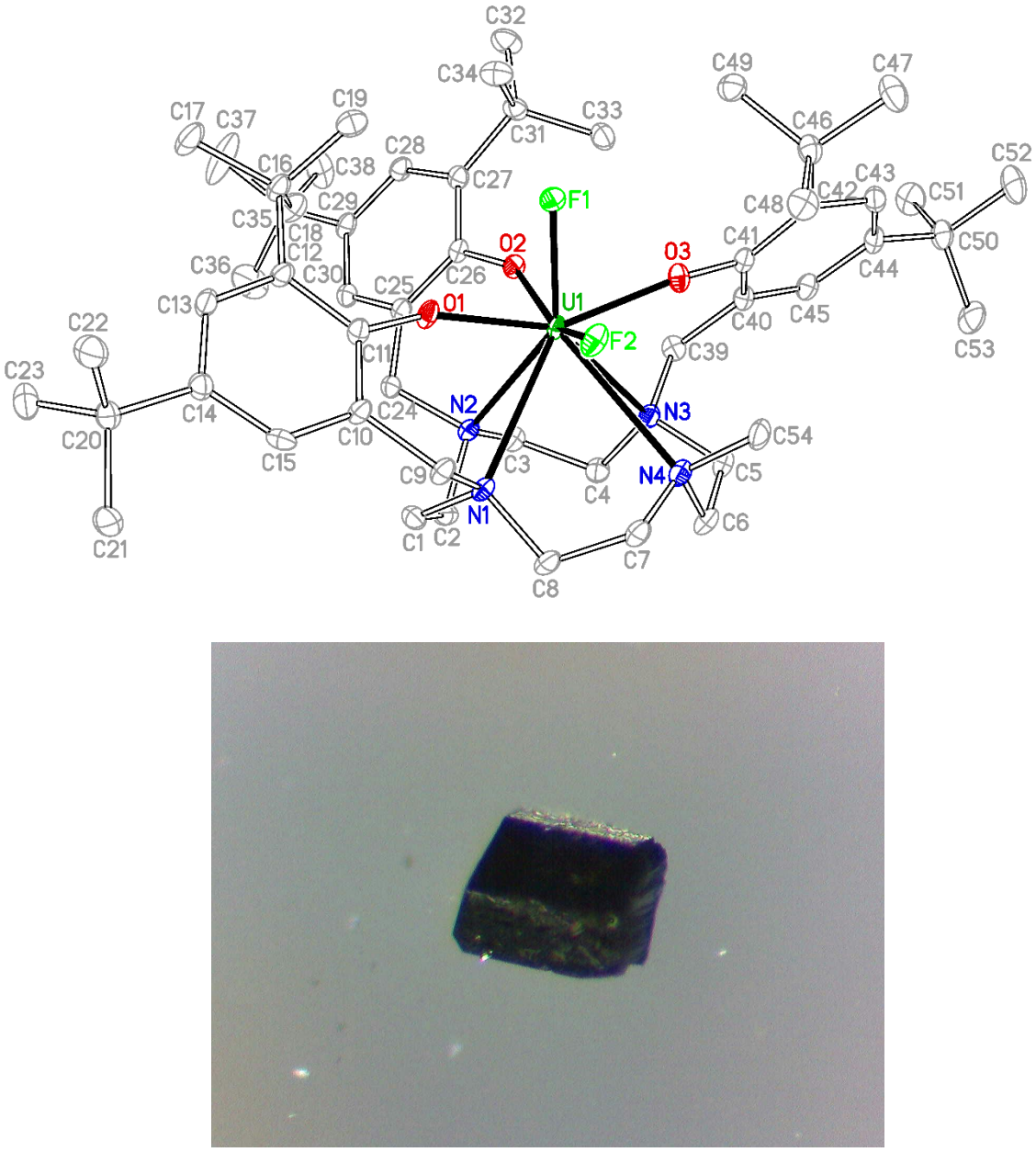

Figure S119: Top: Solid-state molecular structure with the applied numbering scheme of **5** in crystals of [((*t*-Bu,*t*-BuArO)$_3$(Me)cyclen)U^V(F)$_2$] • 2 Et$_2$O (thermal ellipsoids are at the 50% probability level, hydrogen atoms and co-crystallized solvent molecules are omitted for clarity). Bottom: A single crystal of **5** obtained by diffusion of *n*-pentane into a concentrated Et$_2$O solution.

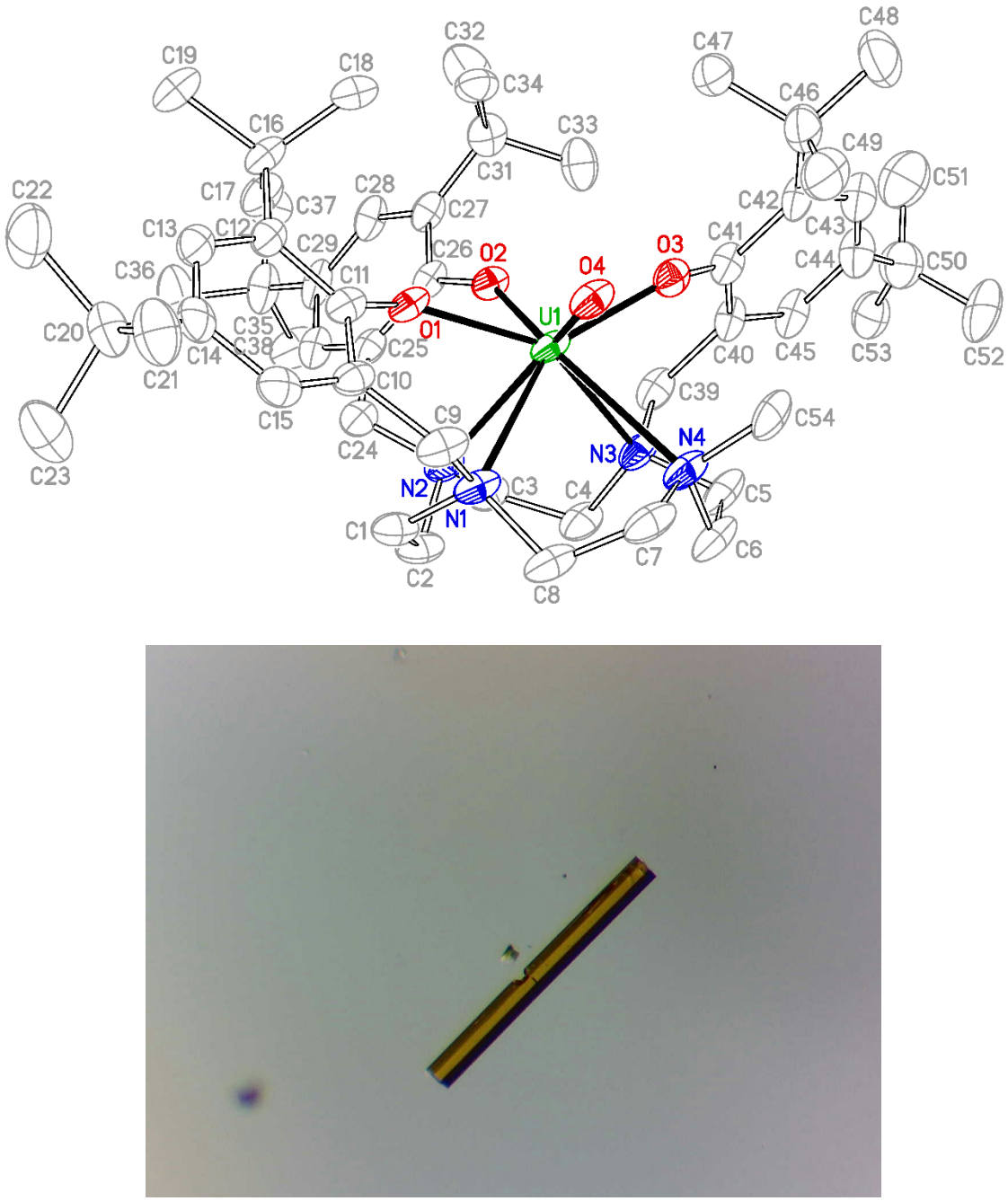

Figure S120: Top: Solid-state molecular structure with the applied numbering scheme of **6** in crystals of [((*t*-Bu,*t*-Bu$ArO)_3$(Me)cyclen)U^V(O)] • 1.5 THF (thermal ellipsoids are at the 50% probability level, hydrogen atoms and co-crystallized solvent molecules are omitted for clarity). Bottom: A single crystal of **6** obtained by diffusion of a concentrated THF solution into *n*-hexane.

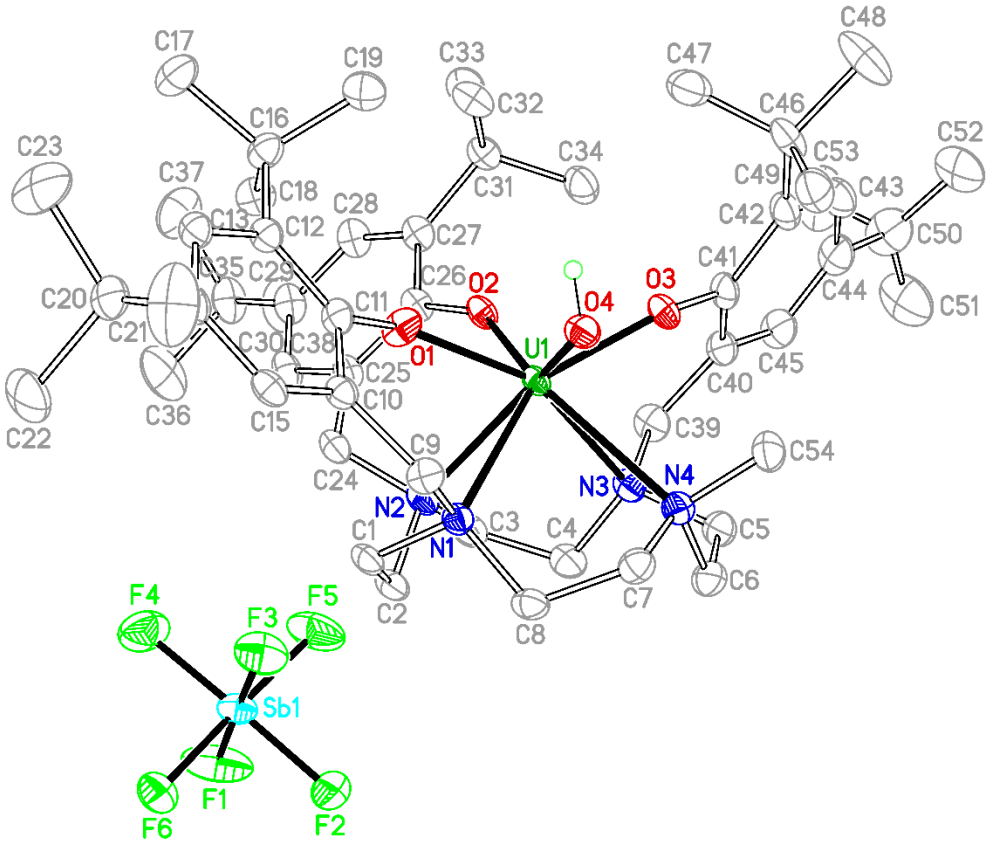

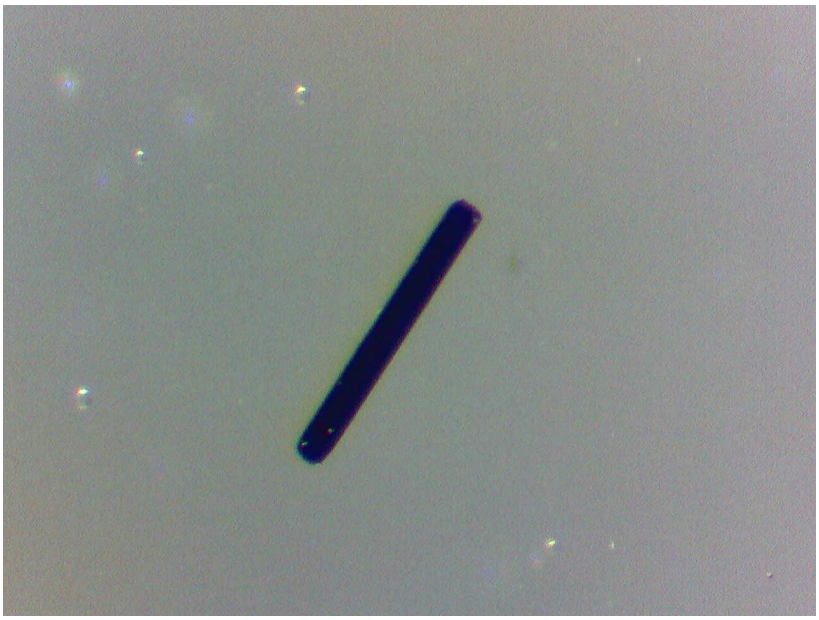

Figure S121: Top: Solid-state molecular structure with the applied numbering scheme of **7** in crystals of [((*t*-Bu,*t*-Bu ArO)$_3$(Me)cyclen)U^V(OH)][SbF$_6$] • 3.5 C$_6$H$_6$ (thermal ellipsoids are at the 50% probability level, hydrogen atoms except for the O*H* atom and co-crystallized solvent molecules are omitted for clarity). Bottom: A single crystal of **7** obtained from a concentrated benzene solution.

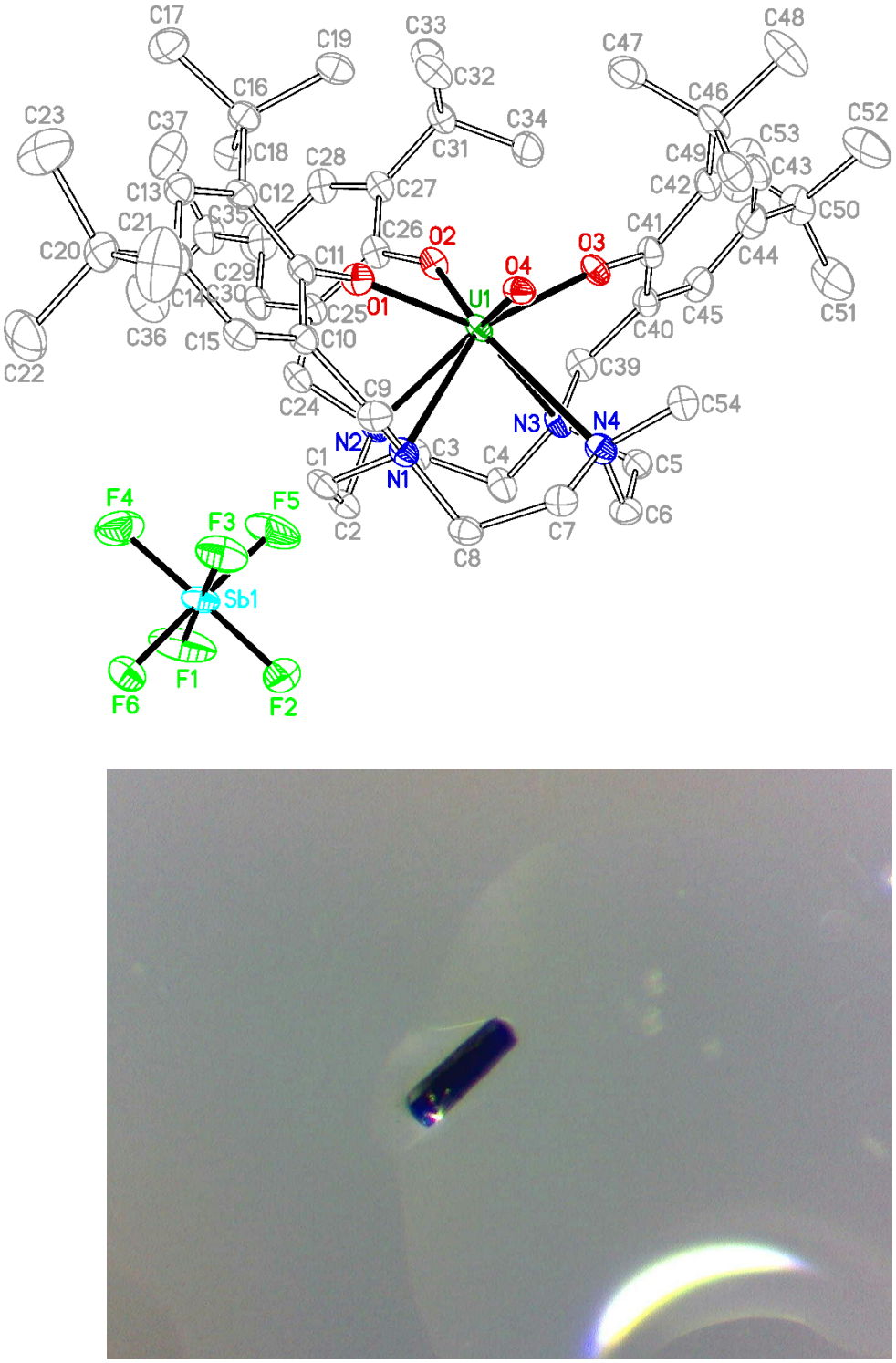

Figure S122: Top: Solid-state molecular structure with the applied numbering scheme of **8** in crystals of [((*t*-Bu,*t*-Bu ArO)$_3$(Me)cyclen)U^{VI}(O)][SbF$_6$] • 3.5 C$_6$H$_6$ (thermal ellipsoids are at the 50% probability level, hydrogen atoms and co-crystallized solvent molecules are omitted for clarity). Bottom: A single crystal of **8** obtained from a concentrated benzene solution.

References

(1) Monreal, M. J.; Thomson, R. K.; Cantat, T.; Travia, Nicholas E.; Scott, Brian L.; Kiplinger, Jaqueline L. *Organometallics* **2011**, *30*, 2031–2038.

(2) Rodríguez-Rodríguez, A.; Regueiro-Figueroa, M.; Esteban-Gómez, D.; Rodríguez-Blas, Teresa; Patinec, Véronique; Tripier, Raphaël; Tircsó, Gyula; Carniato, Fabio; Botta, Mauro; Platas-Iglesias, Carlos. *Chem. Eur. J.* **2017**, *23*, 1110–1117.

(3) Fulmer, G. R.; Miller, A. J. M.; Sherden, N. H.; Gottlieb, Hugo E.; Nudelman, Abraham; Stoltz, Brian M.; Bercaw, John E.; Goldberg, Karen I. *Organometallics* **2010**, *29*, 2176–2179.

(4) Bain, G. A.; Berry, J. F. *J. Chem. Educ.* **2008**, *85*, 532.

(5) Bill, E. *SQUID Program JulX2*, 2019.

(6) Sheldrick, G. M. *SADABS 2014/4*; Bruker AXS Inc.: Madison, Wisconsin, USA, 2014.

(7) Sheldrick, G. M. *SADABS 2016/2*; Bruker AXS Inc.: Madison, Wisconsin, USA, 2016.

(8) Sheldrick, G. M. *Acta crystallographica. Section A, Foundations and advances* **2015**, *71*, 3–8.

(9) Sheldrick, G. M. *Acta crystallographica. Section A, Foundations of crystallography* **2008**, *64*, 112–122.

(10) Dolomanov, O. V.; Bourhis, L. J.; Gildea, R. J.; Howard, Judith A. K.; Puschmann, Horst. *J Appl Crystallogr* **2009**, *42*, 339–341.

(11) Parsons, S.; Flack, H. D.; Wagner, T. *Acta crystallographica Section B, Structural science, crystal engineering and materials* **2013**, *69*, 249–259.